$Cu_2ZnSn(S,Se)_4$ SOLAR CELLS PREPARED FROM Cu_2ZnSnS_4 NANOPARTICLE INKS

YONGTAO QU

PhD

2015

$Cu_2ZnSn(S,Se)_4$ Solar Cells Prepared From Cu_2ZnSnS_4 Nanoparticle Inks

Yongtao Qu

A thesis submitted in partial fulfilment
of the requirements of the
University of Northumbria at Newcastle
for the degree of
Doctor of Philosophy

Research undertaken in the
Faculty of Engineering and Environment

November 2015

Abstract

The selenisation of Cu_2ZnSnS_4 (CZTS) nanoparticle inks offers a potential low-cost route to the creation of Earth-abundant photovoltaic $Cu_2ZnSn(S,Se)_4$ (CZTSSe) thin film absorber layers. This work focuses on the properties of CZTS nanoparticles fabricated under different synthesis conditions, the selenisation kinetics and the performance of CZTSSe solar cell devices made using CZTS nanoparticle inks.

Initially, CZTS nanoparticles were chemically synthesised *via* injection of sulphur into hot metallic precursors. Their composition, structural and optical properties were found to be sensitive to the reaction temperature, cooling rate and reaction time. For a reaction at 225 ℃ for 30 minutes followed by relatively slow cooling (~ 5 ℃/min), it was possible to fabricate kesterite CZTS nanoparticles with an energy bandgap of 1.5 eV.

CZTS nanoparticle inks have a strong effect on the performance of CZTSSe thin film solar cells. Specifically, longer reaction time of 60 minutes increased the device efficiency by increasing the concentration of acceptor levels to 5.3×10^{17} cm^{-3} in kesterite CZTSSe. Quenching the reaction rapidly (~ 20 ℃/min) introduced wurtzite crystal structure and degraded the device efficiency from 5.4 % to 2.3 %. Increasing the reaction temperature to 255 ℃ resulted in the highest cell efficiency of 6.3 % despite the presence of secondary phase Cu_2SnS_3.

In creating CZTSSe photovoltaic thin film absorber layers, high temperature selenisation of the CZTS nanoparticles plays a critical role in the formation of large grains. The results of a series of experiments indicate that the selenisation reaction is controlled by metal cation re-ordering and grain boundary migration (Avrami's model), with a migration energy of 85.38 kJ/mol. Using a high selenium vapour pressure of 226 mbar during the selenisation process it was possible to achieve a device short circuit current density of 37.9 mA/cm^2 resulting from increased carrier generation towards long wavelengths.

Contents

Acknowledgements

I would like to express my sincere gratitude to the following people and institutes who have helped me during my PhD study. Special thanks go to my supervisors Dr. Neil S. Beattie and Dr. Guillaume Zoppi for providing me with continuous support, guidance and encouragement both in my research and life in Newcastle. I would like to thank them for giving me the opportunity to undertake the research under their supervision. Without their constructive advice and encouraging supervisions, it would have been impossible to finish this project on time.

I would like to extend my gratitude to Northumbria University for providing me the scholarship and facilities to carry out my research. This work was also partly funded by the Royal Society. I also would like to thank the financial support from Northumbria Graduate School and Institute of Physics for allowing me to attend conferences. I also acknowledge Dr. Wenyue Li from City University of Hong Kong and NEXUS at Newcastle University for performing the TEM and XPS measurements.

I also thank members of the research group who provided a good research atmosphere and made my time really enjoyable.

Finally, I would like to thank my family and especially my wife for their love and supports.

Declaration

I declare that the work contained in this thesis has not been submitted for any other degree and all the work presented in this thesis was carried out by the candidate except those procedures listed below.

The TEM measurements were performed at City University of Hong Kong. The XPS measurements were taken at National EPSRC XPS User's Service (NEXUS) at Newcastle University. SIMS measurements included were performed by Dr. Guillaume Zoppi, Northumbria University.

Any ethical clearance for the research presented in this thesis has been approved. Approval has been sought and granted by the University Ethics Committee on 25th of March, 2013.

I declare that the word count of this thesis is 35,202 words.

Name:

_____

Date: 19/04/2016

_____

Chapter 1

Introduction

1.1 Research motivations

Sources of renewable energy are becoming increasingly important as a result of increasing green-house gas levels in the atmosphere, the rising cost of energy and the need to ensure security of energy supply. Of these sources, solar energy is appealing because it is the most abundant source of energy on the planet. Solar radiation incident on the Earth in one hour is roughly equivalent to current annual consumption [1]. Photovoltaic (PV) conversion is the direct conversion of solar energy into electrical power and is attracting global continuous research interest stemming from advances in material science and reduced cost. Among the light absorbing materials used in thin-film PV cells, cadmium telluride (CdTe) and copper indium gallium selenide (CIGS) have been used to produce solar cells with efficiencies greater than 20 % [2]. However, as shown in Figure 1.1, the relatively scarce and expensive constituent elements indium, gallium and tellurium may limit their potential application on the terawatt level [3]. The abundance of indium in the upper continental crust is estimated to be 0.16 ppm while tellurium is even lower to 0.001 ppm. In contrast, the quaternary compound copper zinc tin sulphide (CZTS) is composed of naturally abundant (crust abundance of 68, 79 and 2.2 ppm for copper,

zinc and tin respectively) and relatively cheap elements, making it an attractive alternative PV material. More importantly, the CZTS technology is expected to benefit from the rich research experience of CIGS because of the material similarities. CZTS has a near optimum direct energy band gap of ~1.5 eV and a large absorption coefficient of ~10^4 cm^{-1} (in the photon energy range greater than 1.2 eV) [4, 5], minimising the thickness of material needed to absorb the incident light and hence reducing material costs. In recent years, CZTS has experienced rapid development as the device efficiency has increased from 6.8 % to 12.6 % [6-16].

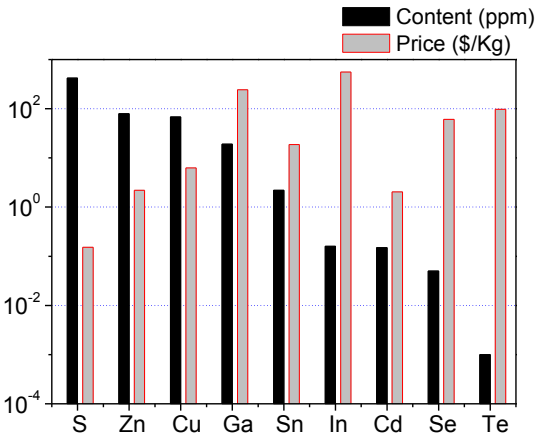

Figure 1.1 Natural abundance and the world trading price of the elements used in CdTe, CIGS and CZTS thin film solar cells. Abundance of metals is downloaded from www.webelements.com. Average prices are taken from www.metalprices.com (April 2014 to May 2015).

Among the variety of techniques employed for preparation of PV absorber films, the deposition of CZTS nanoparticle inks and subsequent selenisation offers a low cost route to fabricate high quality absorber layers that can yield $Cu_2ZnSn(S,Se)_4$

(CZTSSe) thin film solar cells with efficiency as high as 9.0 % [16]. However, considering the detailed balance limit for CZTS, there is still a large difference between the theoretical and experimental power conversion efficiencies [17]. To become a reliable technology for the production of CZTSSe thin film solar cells, several challenges exist for the nanoparticle ink-based technique. In particular, controllable fabrication of CZTS nanoparticles is necessary and the link between device performance and nanoparticle ink properties is not well understood. In addition, despite its importance in the production of high quality CZTSSe absorber layers from nanoparticle inks, the selenisation process also lacks in-depth investigation. Consequently, further work is required to improve device performance of CZTSSe solar cells fabricated from nanoparticle inks.

1.2 Organisation of the thesis

This thesis is divided into eight chapters. Following the introduction, the semiconductors physics and fundamental theory of solar cell devices is presented in Chapter 2. Chapter 3 focuses on the thin film solar cell made from CZTS by reviewing the material properties and technologies to produce CZTSSe devices. In particular, nanoparticle ink-based deposition techniques, which could provide low-cost scalable routes to produce CZTSSe devices are described in detail. The characterisation techniques used in this work are described in Chapter 4. The experimental results are discussed and analysed in the following three chapters. In Chapter 5, the structure, composition, and optical properties of CZTS nanoparticles

are systematically investigated in order to assess the influence of reaction temperature and time. In Chapter 6, the processing and characterisation of solar cells made from CZTS nanoparticle inks are described. The link between the properties of the nanoparticle inks and the completed solar cell performance are emphasised in this chapter. In Chapter 7, the kinetics of the selenisation reaction and in particular, recrystallization and grain growth are studied by controlling the selenisation conditions. The performance of solar cells made from the absorbers selenised for different times, temperatures and selenium vapour pressures, are also presented in this chapter. Chapter 8 describes the conclusions from the work and suggestions for further work.

1.3 List of publications and conference presentations

The research has led to a number of publications as outlined below:

1) Y. Qu, G. Zoppi and N. S. Beattie, The role of nanoparticle inks in determining the performance of $Cu_2ZnSn(S,Se)_4$ thin film solar cells, *Progress in Photovoltaics: Research and Application*s, 2016, DOI: 10.1002/pip.2756.

2) Y. Qu, G. Zoppi and N. S. Beattie, Selenisation kinetics in $Cu_2ZnSn(S,Se)_4$ solar cells prepared from nanoparticle inks, *Solar Energy Materials and Solar Cells*, 2015, http://dx.doi.org/10.1016/j.solmat.2015.12.016.

3) Y. Qu, G. Zoppi, R. W. Miles and N. S. Beattie, Influence of reaction conditions on the properties of solution-processed Cu_2ZnSnS_4 nanocrystals. *Materials*

Research Express **2014**, 1: 045040.

4) Y. Qu, G. Zoppi and N. S. Beattie, Effect of reaction temperature on the properties of Cu_2ZnSnS_4 nanocrystals prepared using a hot injection method. Proceedings of the 10th Photovoltaic Science, Applications, and Technology Conference, Lougborough, UK, April 23, 2014, 89-92.

5) Y. Qu, G. Zoppi and N. S. Beattie, $Cu_2ZnSn(S,Se)_4$ solar cells prepared from nanoparticle inks: strategies to increase long wavelength photons conversion, 6th European Kesterite Workshop 2015, Northumbria University at Newcastle, UK, November 19, 2015. (Oral presentation)

6) Y. Qu, G. Zoppi and N. S. Beattie, Photocurrent enhancement in $Cu_2ZnSn(S,Se)_4$ solar cells prepared from nanoparticle inks. Nanotechnology for next generation high efficiency photovoltaics spring international school & workshop. Mao, Menorca, Balearic Islands, Spain, April 20, 2015. (Oral presentation)

7) Y. Qu, G. Zoppi and N. S. Beattie, Thin film solar cells made from Cu_2ZnSnS_4 nanoparticle inks. Northumbria research conference 2015, Northumbria University, UK, May 20, 2015. (Poster presentation)

Chapter 2

Semiconductor physics and theory of solar cells

Solar cells are semiconductor devices that convert sunlight directly into electrical energy using the photovoltaic process. To understand the working principle of solar cells, the essential definitions and theoretical basis of the semiconductor, the formation of *p*-*n* junctions, and characteristics and working parameters of solar cells are presented in this chapter.

2.1 Semiconductor fundamentals

2.1.1 Energy band formation

Quantum physics indicates that the electrons of isolated atoms are dispersed on discrete energy levels. Taking silicon for example, 10 of its 14 electrons occupy the inner energy levels which are tightly bounded to the nucleus. It is the four remaining valence electrons that determine the electronic properties of the material. As shown in Figure 2.1, the 3*s* orbital (principal quantum number n=3, azimuthal quantum number l=0, magnetic quantum number m=2l+1=1) contains two valence electrons and the three 3*p* orbitals (n=3, l=1, m=2l+1=3) contains the other two valence electrons. The 3*s* orbital and three 3*p* orbitals mix and form four degenerate sp^3 hybrid orbitals with equal energy levels and bond angles of 109.5 °. These sp^3 hybrid orbitals facilitate the formation of the tetrahedral bonds, which determines the crystal

structure [18].

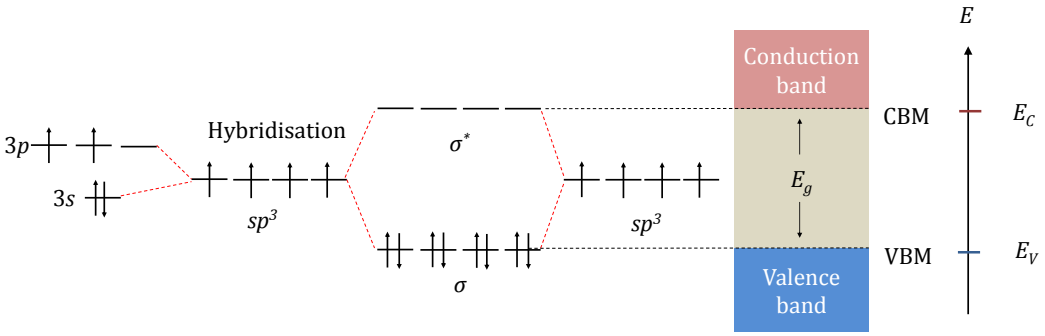

Figure 2.1 Energy band formation of silicon.

When two Si atoms are brought together, the degenerated hybrid orbitals split into two levels: bonding levels with energy lower than the original energy levels and antibonding levels with energy higher than the original energy levels. As shown in Figure 2.1, the electrons fully occupy the bonding energy levels and form four σ bonds with equal length and strength while all states in upper antibonding levels are empty. More generally, when large numbers of Si atoms are bonded to form bulk crystals, two continuous energy bands (the lower energy valence band and higher energy conduction band) are formed. The top of the valence band is called valence band maximum (VBM) with energy of E_V. The bottom of the conduction band is called conduction band minimum (CBM) with energy of E_C. The energy bandgap E_g between E_V and E_C is the width of the forbidden energy gap, which is not accessible for free electrons. Semiconductors have moderate energy bandgaps between conductors and insulators. For example, Si has an energy bandgap on the order of ~1 eV. At room temperature, a considerable numbers of electrons can be thermally

excited from the valence band to the conduction band and the material acquires a moderate conductivity.

If we plot energy E versus momentum p, a more complex energy-momentum relationship is shown in Figure 2.2. The E-p curves near the CBM or the VBM are essentially parabolic, and the energy bandgap E_g therefore is the energy space between the two parabola peaks of conduction band and valence band as shown in Figure 2.2.

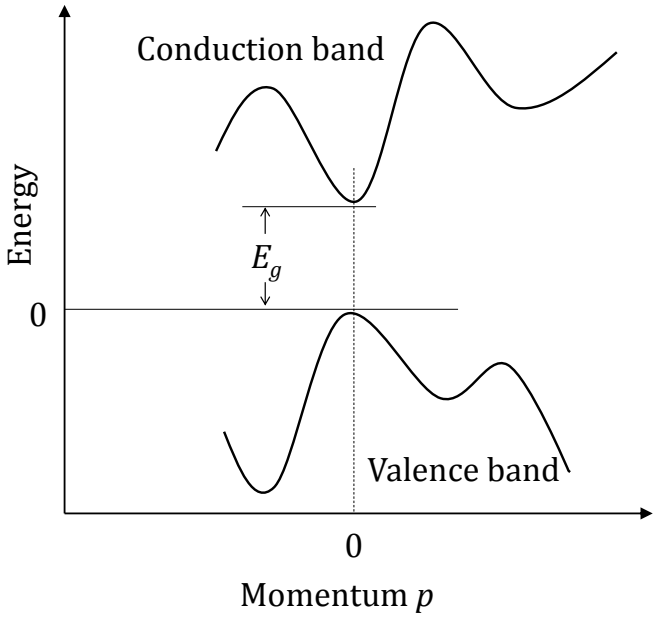

Figure 2.2 A schematic energy-momentum diagram for a direct semiconductor.

Depending on the relative position of the CBM and VBM, the semiconductors can be divided into two groups: direct or indirect bandgap materials. In direct bandgap materials as gallium arsenide (GaAs) and CZTS, the VBM and CBM have the same momentum position as shown in Figure 2.2, and photons with energy exceeding the energy bandgap can excite an electron across the bandgap. As a result, much higher

absorption coefficients ($> 10^4$ cm^{-1}) are observed and much thinner layers (~ 1 micron) are sufficient to absorb the incident light [19, 20]. For indirect bandgap materials however, a momentum difference is observed between the VBM and CBM. Thus both an energy change and a momentum change are required and result in limited absorption processes as only suitable photons contribute to the electron excitation from valence band to conduction band. Consequently, relatively weak light absorption is observed and the material typically has an absorption coefficient less than ~ 10^2 cm^{-1}. Si is an example of this type of semiconductor and hence thick absorber layers (hundreds of microns) are required for solar cells [21].

2.1.2 Carriers under thermal equilibrium conditions

Free electrons are obtained when electrons in the valence band are excited to the conduction band. Correspondingly, an equal number of positively charged holes are observed in the valence band. The probability of an electron occupying an electronic state of energy E can be described by the Fermi distribution function $F(E)$ [22]:

$$F(E) = \frac{1}{1+exp[(E-E_F)/kT]} \qquad (2\text{-}1)$$

where k is the Boltzmann constant, T is the absolute temperature, E_F is the Fermi energy defined as the energy at which the probability of occupation by an electron is 50 %.

In an intrinsic semiconductor, the electron density, n in the conduction band and the hole density, p in the valence band are given by Equation 2-2 and 2-3 respectively:

$$n = N_C \times F(E_C) = N_C exp[-(E_C - E_i)/kT] = n_i \quad \text{for } (E_C - E_i) > 3kT \qquad (2\text{-}2)$$

$$p = N_V \times [1 - F(E_V)] = N_V exp[-(E_i - E_V)/kT] = n_i \text{ for } (E_i - E_V) > 3kT \qquad (2\text{-}3)$$

where N_C and N_V are constant called effective densities of states in the conduction band and valence band respectively, E_i is Fermi level for the intrinsic semiconductor, n_i is the intrinsic carrier density. In an intrinsic semiconductor, n=p=n_i, and E_i can be obtained by equating Equations 2-2 and 2-3:

$$E_i = (E_C + E_V)/2 + (kT/2)\ln(N_V/N_C) \qquad (2\text{-}4)$$

As the second term in Equation 2-4 is much smaller compared with the energy bandgap at room temperature, E_i hence generally lies in the middle of the bandgap.

In addition, the intrinsic carrier density n_i can be written in terms of the energy bandgap E_g of the material by multiplying Equations (2-2) and (2-3):

$$n_i{}^2 = np = N_C N_V exp\left(-E_g/kT\right) \qquad (2\text{-}5)$$

When electrons in the conduction band and holes in the valence band are introduced artificially by donors and acceptors, the semiconductor becomes an extrinsic semiconductor. Correspondingly, the semiconductor is called *n*-type or *p*-type as electrons and holes respectively become the majority carriers in the material. Intrinsic semiconductors, such as pure Si, can be *n*-type or *p*-type doped with impurities to increase their conductivity by replacing Si (a group IV) atoms with group V atoms or group III atoms. Compound semiconductors like CIGS and CZTS

are intrinsically doped by defects such as vacancies, antisites and interstitials which act as donors or acceptors. This is discussed further in section 3.1.3.

Based on Equation 2-2 and 2-3, the Fermi level position for *n*-type and *p*-type semiconductors can be described in Equation 2-6 and 2-7, respectively:

$$E_C - E_F = kT \ln(N_C/N_D) \qquad (2\text{-}6)$$

$$E_F - E_V = kT \ln(N_V/N_A) \qquad (2\text{-}7)$$

It is clear that higher donor concentration N_D and acceptor concentration N_A will push the Fermi level closer to the bottom of the conduction band and top of the valence band, respectively. Figure 2.3 illustrates the different energy levels in a semiconductor. The excess donors create an isolated energy level called donor level E_D just below the CBM. Similarly, acceptors create an acceptor level E_A just above the VBM as shown in Figure 2.3. In a heavily doped *n*-type semiconductor, E_F actually moves above E_C such that electrons can only be excited into conduction band levels above the Fermi level. This is observed as an apparent widening of the semiconductor bandgap, known as Burstein-Moss effect [23].

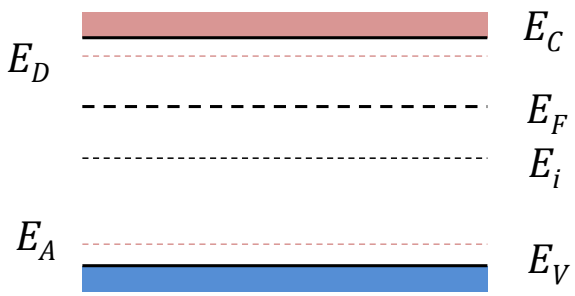

Figure 2.3 Band diagram showing energy levels in a semiconductor.

Under complete ionisation conditions, the free electron density n in an n-type semiconductor *is* equal to the donor concentration N_D, and can be described by combining Equation 2-6 and 2-2:

$$n = N_D = N_C exp[-(E_C - E_F)/kT] = N_C exp[-(E_C - E_i)/kT] exp[(E_F - E_i)/kT]$$

$$= n_i exp[(E_F - E_i)/kT] \qquad (2\text{-}8)$$

Similarly, the free hole density p in p-type semiconductor can be described as:

$$p = n_i exp[(E_i - E_F)/kT] \qquad (2\text{-}9)$$

Although the majority carriers electrons or holes dominate in n- or p-type semiconductors, the product of Equation 2-8 and 2-9 remains constant at n_i^2 at a given temperature. The relationship $np=n_i^2$ is known as the law of mass action and is valid for both intrinsic and extrinsic semiconductors under thermal equilibrium conditions.

2.1.3 Carrier generation and direct recombination under optical excitation

Most semiconductor devices operate under nonequilibrium conditions in which excess carriers are introduced into the semiconductor. In solar cell operation, these excess carriers are generated optically as shown in Figure 2.4.

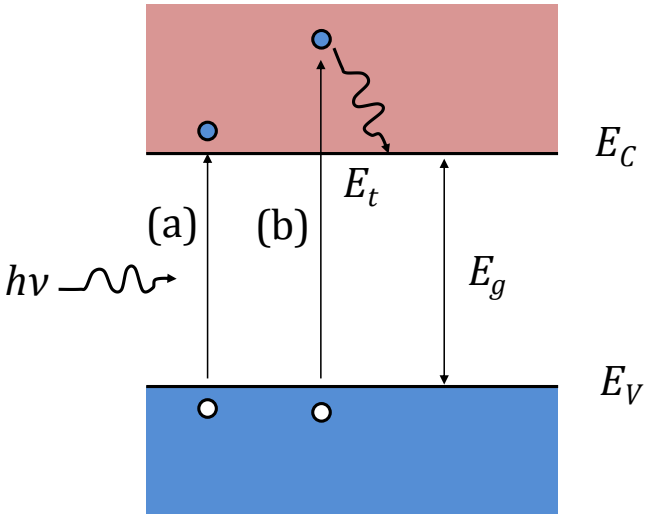

Figure 2.4 Electron excitation for (a) photon energy $h\nu = E_g$, and (b) $h\nu > E_g$.

Incident photons with energy $h\nu$ equal to the energy bandgap of the semiconductor can excite electrons from the top of valence band to the bottom of conduction band. This generates electron-hole pairs as shown in process (a) in Figure 2.4. If $h\nu$ is greater than the energy bandgap (process b), electron-hole pairs can also be generated and the excess energy ($h\nu$ - E_g) is dissipated as heat to the lattice of the semiconductor. Processes (a) and (b) are called intrinsic transitions and no electron-hole pairs are generated when $h\nu$ is smaller than E_g.

When excess carriers are introduced into the semiconductors and the thermal-equilibrium condition is disturbed, recombination process exists to restore the system to equilibrium. Recombination process can be classified as direct and indirect processes. Direct recombination dominates in direct bandgap semiconductors as illustrated in Figure 2.5.

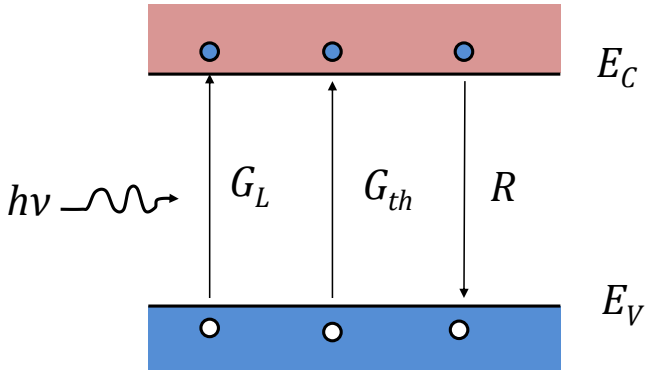

Figure 2.5 Carrier generation and direct recombination process under illumination.

Considering a semiconductor under thermal equilibrium electron-hole pairs are continuously generated and annihilated at a generation rate G_{th} and a recombination rate R_{th}, respectively. G_{th} must be balanced by R_{th} to satisfy the mass action law. Therefore, for a *p*-type semiconductor for example, it should satisfy:

$$G_{th} = R_{th} = \beta n_{po} p_{po} \qquad (2\text{-}10)$$

where β is a recombination proportionality constant and n_{po} and p_{po} represent the electron and holes densities in a *p*-type semiconductor at thermal equilibrium.

If the semiconductor is illuminated by light of energy $E = h\nu \geq E_g$, excess carriers are generated at a rate of G_L as shown in Figure 2.5. The generation and recombination rates then modified to:

$$G = G_L + G_{th} \qquad (2\text{-}11)$$

$$R = \beta n_p p_p = \beta(n_{po} + \Delta n)(p_{po} + \Delta p) \qquad (2\text{-}12)$$

where Δn and Δp are excess carrier concentrations and should be equal to each other to keep charge neutrality. The net rate of change in electron concentration is

then given by:

$$\frac{dn_p}{dt} = G - R = G_L + G_{th} - R \qquad (2\text{-}13)$$

Under steady state, $dn_p/dt = 0$ and G_L is given by:

$$G_L = R - G_{th} = U = \beta(n_{po} + p_{po} + \Delta n)\Delta n \qquad (2\text{-}14)$$

where U is defined as the net recombination rate. For a p-type semiconductor, Δn and $n_{po} \ll p_{po}$ allow Equation 2-14 to be simplified into:

$$U = \beta p_{po}\Delta n = \frac{n_p - n_{po}}{\frac{1}{\beta p_{po}}} = \frac{n_p - n_{po}}{\tau_n} \qquad (2\text{-}15)$$

Therefore, the net recombination rate U is proportional to the excess minority carrier concentration. The proportionality constant $1/\beta p_{po}$ is defined as the excess minority carrier lifetime τ_n.

To understand the physical meaning of τ_n, the minority carrier density variation can be studied after the light is suddenly turned off at t=0 where G_L= 0. Equation 2-13 can then be rewritten as:

$$\frac{dn_p}{dt} = G_{th} - R = -U = -\frac{n_p - n_{po}}{\tau_n} \qquad (2\text{-}16)$$

Given the boundary condition that $n_p(t = 0) = n_{po} + \tau_n G_L$, Equation 2-16 can be converted into:

$$n_p(t) = n_{po} + \tau_n G_L exp(-t/\tau_n) \qquad (2\text{-}17)$$

Using Equation 2-17, τ_n can then be determined by extrapolating the minority

carrier decay curve. As shown in Figure 2.6, the excess minority carriers will decay back to the equilibrium carrier concentration because of recombinations. The minority lifetime thus can be understood as the average time that a carrier can spend in an excited state before recombining.

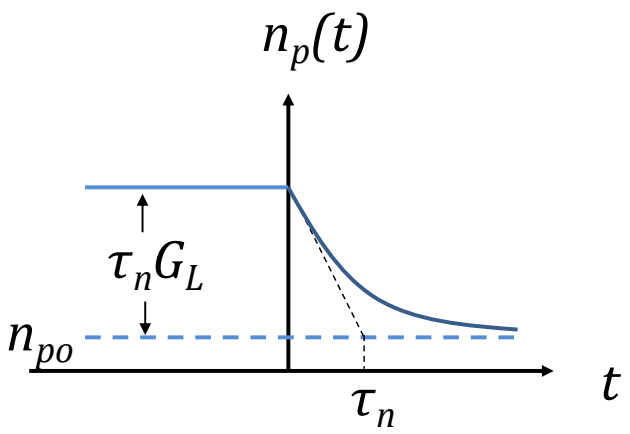

Figure 2.6 Decay of minority carriers (electrons) in a *p*-type semiconductor with time.

2.2 Theory of the *p-n* junction

Optically excited minority carriers normally recombine with the majority carriers and thus do not contribute to a photocurrent. A built-in electric field is therefore required to separate and collect the generated carriers before recombination. In a solar cell, such a field is achieved by a *p-n* junction when a *p*-type and an *n*-type semiconductor are brought into contact.

2.2.1 Formation of a *p-n* junction

As shown in Figure 2.7 (a), a *p-n* junction is formed by joining *p*-type and *n*-type

semiconductor materials.

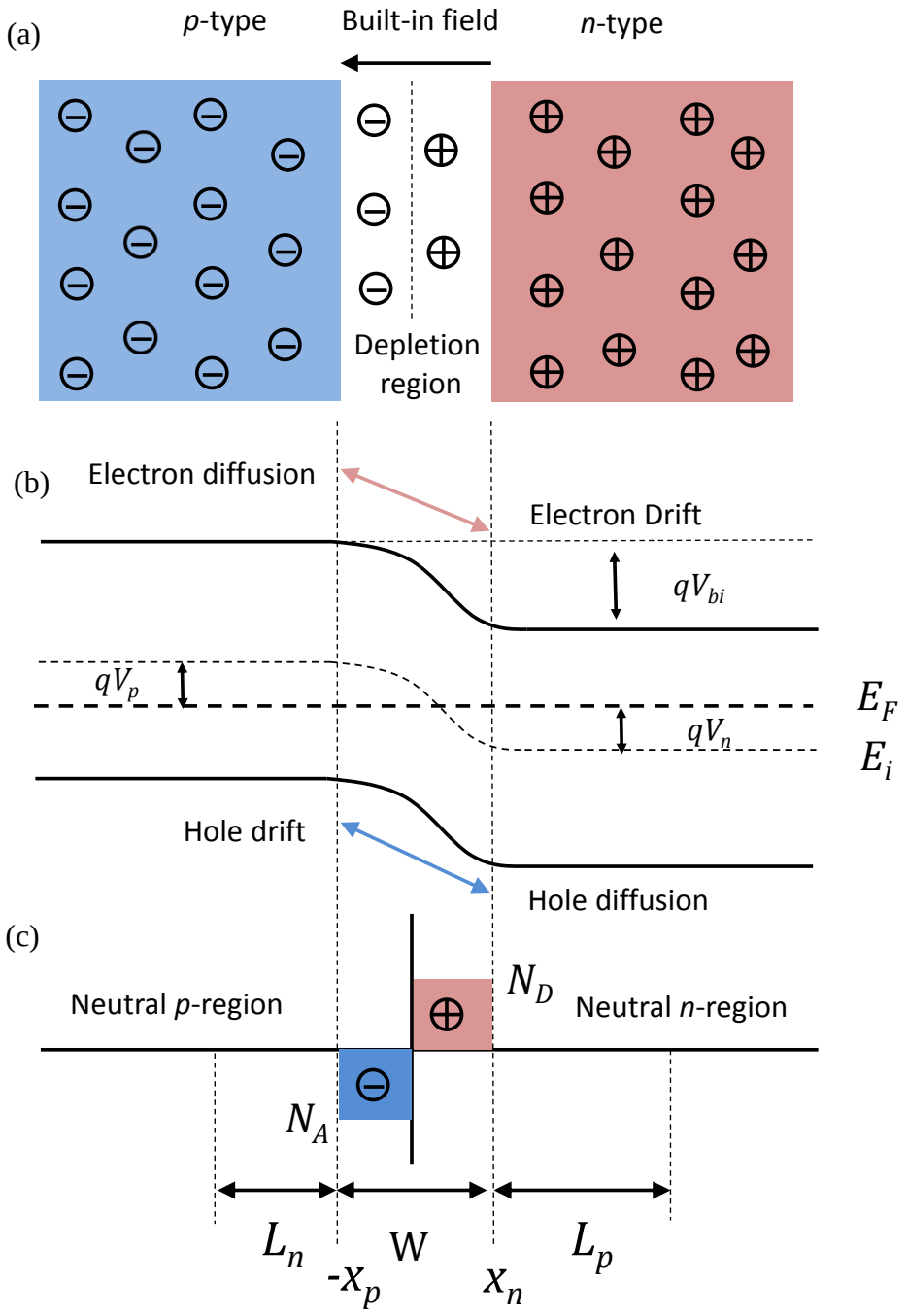

Figure 2.7 (a) Schematic of a *p*-*n* junction at equilibrium, (b) energy band diagram of a *p*-*n* junction and (c) space charge distribution of a *p*-*n* junction under thermal equilibrium.

The *p*-type semiconductor contains a large number of free holes as the majority

carriers, and the *n*-type semiconductor is rich in free electrons. When the *p*-type and *n*-type materials are joined together, excess holes in *p*-side and excess electrons in *n*-side diffuse to the opposite side. At the same time, the negatively charged fixed acceptor ions in *p*-side and positively charged fixed donor ions in *n*-side near the junction are left in the semiconductor lattice, resulting in an electron field at the junction. This field removes excess carriers close to the junction and this creates a depletion region as shown in Figure 2.7 (a). In this region, the direction of the electric field is from the *n*-side to the *p*-side and opposes the majority carrier diffusion process. At the same time, the minority carriers that reach the junction can drift across the depletion region and become majority carries in the other side. When the diffusion current equals the drift current, equilibrium is reached and the net current across the junction is zero.

As shown in Figure 2.7 (b), the energy difference between E_F and E_i away from the junction on the *p*-side is given as:

$$qV_p = E_i - E_F \qquad (2\text{-}18)$$

Putting Equation 2-9 into Equation 2-18 and assuming complete ionisation ($p = N_A$) gives:

$$qV_p = kT \ln\left(\frac{N_A}{n_i}\right) \qquad (2\text{-}19)$$

Similarly, the energy difference between E_F and E_i on the *n*-side is given in Equation 2-20:

$$qV_n = kT \ln\left(\frac{N_D}{n_i}\right) \quad (2\text{-}20)$$

The total energy different between the *p*-side and *n*-side is obtained by adding Equations 2-19 and 2-20:

$$qV_{bi} = kT \ln\left(\frac{N_A N_D}{{n_i}^2}\right) \quad (2\text{-}21)$$

Here, V_{bi} is known as the built-in potential. Figure 2.7 (b) illustrate that the total electrostatic potential across the junction is V_{bi}.

To maintain the overall space charge neutrality of the semiconductor, the total negative charge per unit area on the *p*-side junction must be equal to the total positive charge per unit area on the *n*-side junction:

$$N_A x_p = N_D x_n \quad (2\text{-}22)$$

where x_p is extent of the depletion region penetrating into the *p*-type semiconductor and x_n is extent of the depletion region penetrating into the *n*-type semiconductor as shown in Figure 2.7 (c). The total depletion region width W is given by:

$$W = x_p + x_n = \sqrt{\frac{2\varepsilon_s}{q}\left(\frac{N_A + N_D}{N_A N_D}\right)V_{bi}} \quad (2\text{-}23)$$

where ε_s is semiconductor permittivity. Equation 2-23 reveals that W depends strongly on the doping concentrations in the *p*- and *n*-side, respectively. When one side of the junction is more highly doped, the width of the depletion region varies inversely with doping concentration and penetrates into the side with the lower doping. For example, when the *n*-side of the junction is more heavily doped than the

p-side ($N_D \gg N_A$) Equation 2-23 can be simplified and indicates that the depletion region penetrates into the *p*-side:

$$W = x_p = \sqrt{\frac{2\varepsilon_s V_{bi}}{qN_A}} \qquad (2\text{-}24)$$

Furthermore, if a positive bias (also known as forward bias) V_F is applied to the *p*-side of the junction with respect to the *n*-side, the total electrostatic potential cross the junction is reduced to V_{bi}-V_F. In contrast, if a negative bias, which is known as reverse bias V_R is applied to the *p*-side of the junction, the total electrostatic potential cross the junction is increased to V_{bi}+V_R. For a one-sided heavily doped junction, the depletion region width is then revised into Equation 2-25:

$$\mathrm{W} = \sqrt{\frac{2\varepsilon_s (V_{bi} - V)}{qN_B}} \qquad (2\text{-}25)$$

where N_B is the doping concentration of the lightly doped material, V is positive for forward bias and negative for reverse bias. It is clear that forward bias reduces the depletion region width while reverse bias increases the depletion region width.

In addition to the depletion region width, L_n is the electron (minority carriers) diffusion length in the *p*-region and L_p is the diffusion length of holes in the *n*-region as shown in Figure 2.7 (c). The minority carrier diffusion length is defined as the average distance a minority carrier can move from the point of generation to the depletion region before it recombines with a majority carrier.

2.2.2 Heterojunction

In contrast to the homojunction that is formed between two materials with same energy bandgap and opposite doping, such as the case demonstrated in the previous section, a heterojunction is formed by two dissimilar semiconductors with different energy bandgaps, different work function φ and different electron affinities χ. The work function is defined as the energy required to remove an electron from Fermi level to a position just outside the material (the vacuum level as shown in Figure 2.8). The work function of a semiconductor is not a constant as the Fermi Level of the semiconductor is influenced by the doping density. The electron affinity however is a constant for a given semiconductor. It defines as the energy required to remove an electron from the bottom of the conduction band to the vacuum level. In Figure 2.8 (a), the conduction band energy difference is represented as ΔE_C and valence band energy difference is represented as ΔE_V.

To form ideal heterojunctions, the materials should have similar lattice constants as lattice mismatch results in a high density of defects at the interface which act as recombination centres. When two semiconductors with different energy bandgaps and electron affinities are brought into contact, charge is transferred until the Fermi levels are equalised across the two sides. The energy band profile of an ideal heterojunction at equilibrium is shown in Figure 2.8 (b). The discontinuities act as barriers to the flow of electron and limit the device performance.

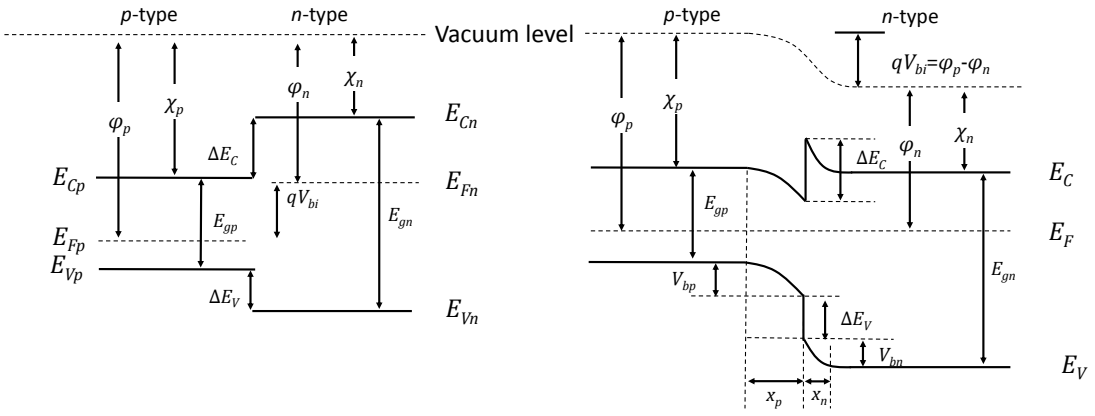

(a) (b)

Figure 2.8 (a) Electron energy band diagram of two isolated semiconductors, (b) Energy band diagram of an ideal *p-n* heterojunction at thermal equilibrium.

As shown in Figure 2.8, the total built-in potential V_{bi} of the heterojunction is the sum of the electrostatic potentials of the two sides at equilibrium:

$$V_{bi} = V_{bn} + V_{bp} \qquad (2\text{-}26)$$

When a bias is applied to the heterojunction, the total depletion width is equal to:

$$W = x_p + x_n = \sqrt{\frac{2\varepsilon_n\varepsilon_p(N_A+N_D)^2(V_{bi}-V)}{qN_AN_D(\varepsilon_nN_D+\varepsilon_pN_A)}} \qquad (2\text{-}27)$$

For the case when the *n*-side is more heavily doped relative to the *p*-side, i.e. $N_D \gg N_A$, Equation 2-27 can be simplified into:

$$W = x_p = \sqrt{\frac{2\varepsilon_p(V_{bi}-V)}{qN_A}} \qquad (2\text{-}28)$$

2.2.3 Schottky junction

In addition to the *p-n* junction formed between semiconductors, metal contacts are needed to collect photo-generated carriers at the front and rear surfaces of a solar cell.

For example, when a metal and an *n*-type semiconductor are come into contact, a Schottky junction is formed as shown in Figure 2.9.

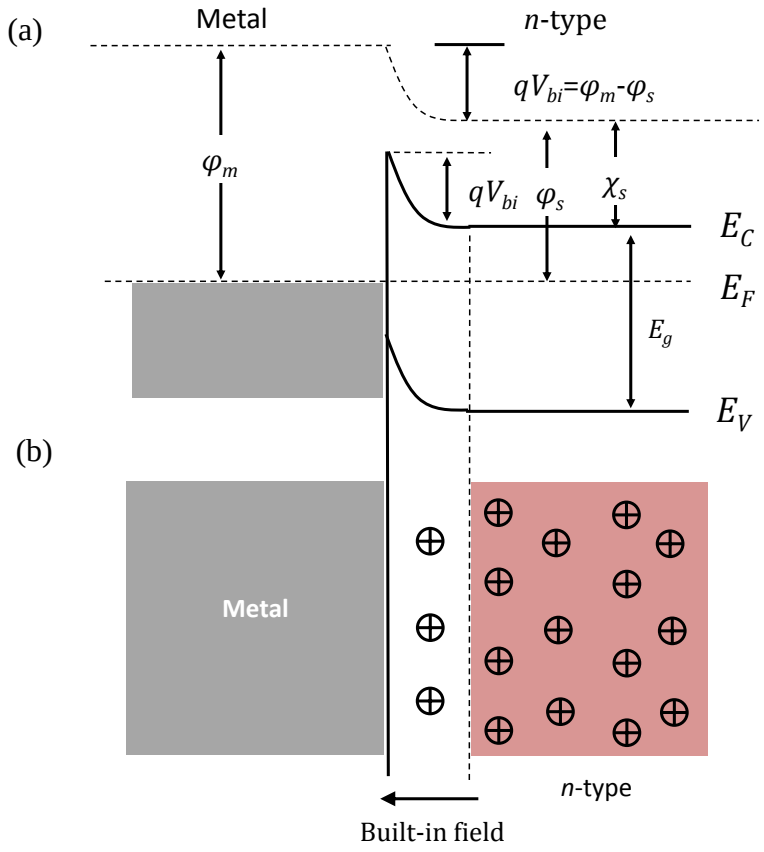

Figure 2.9 (a) Energy band diagram of a Schottky junction at thermal equilibrium with $\varphi_m > \varphi_s$. (b) Schematic of a Schottky junction formed between a metal and an *n*-type semiconductor.

In the condition that the work function of metal (φ_m) is larger than that of the semiconductor (φ_s), the Femi level of the semiconductor has higher energy than that of the metal. Electrons from the conduction band of the semiconductor flow into the metal until the Fermi levels of the semiconductor and metal are coincident with each other. As the electrons move out of the semiconductor into the metal, the free electron concentration in the semiconductor region near the junction decreases.

According to Equation 2-6, the separation between the CBM and the Fermi level of the semiconductor increases with decreasing electron concentration. The conduction band edge thus bends up as shown in Figure 2.9 (a) and the amount of band bending is equal to the work function difference of the metal and semiconductor, i.e. $qV_{bi} = \varphi_m - \varphi_s$. V_{bi} is the potential barrier of an electron has to surmount when moving from the semiconductor into the metal. An electric field is established from the semiconductor to the metal as shown in Figure 2.9 (b). Since the electrons move out of the semiconductor into the metal and leave positive charged donors back, a depletion region is created near the surface between the metal and semiconductor. Unlike the *p*-*n* junction however, the depletion region is only formed in the semiconductor side because the large number of carriers available in the metal side and immediately compensate the loss of carriers diffused to the semiconductor side [24].

2.3 Solar cell theory

2.3.1 Ideal diode equation

Due to the depletion region and built-in voltage, a *p*-*n* junction only allows current to flow in one direction when a bias is applied. In the dark, a solar cell has the same current-voltage characteristic as a diode. The ideal current-voltage characteristics of diodes are derived by assuming that the doped regions are uniformly doped and have abrupt boundaries, and low-injection that the injected minority carrier concentration

is small compared with the majority carrier concentration.

In the following analysis, p_{po} represents the density of holes in a *p*-type semiconductor and n_{no} represents the density of electrons in a *n*-type semiconductor at equilibrium. For complete ionisation, the majority carrier density p_{po} and n_{no} equals the doping density N_A and N_D. Equation 2-21 thus can be rewritten into:

$$qV_{bi} = kT \ln\left(\frac{p_{po}n_{no}}{{n_i}^2}\right) = kT \ln\left(\frac{p_{po}n_{no}}{n_{po}p_{po}}\right) = kT \ln\left(\frac{n_{no}}{n_{po}}\right) \qquad (2\text{-}29)$$

Rearranging Equation 2-29 gives:

$$n_{no} = n_{po}\exp(\frac{qV_{bi}}{kT}) \qquad (2\text{-}30)$$

From Equation 2-30, it can be seen that the electron densities at the two depletion region boundaries are related by V_{bi}. When a bias is applied, Equation 2-30 may be rewritten as:

$$n_n = n_p\exp[\frac{q(V_{bi}-V)}{kT}] \qquad (2\text{-}31)$$

where n_n and n_p are the density of electrons at the boundaries of the depletion region in the *n*- and *p*-side respectively at nonequilibrium. Assuming low-injection, the injected minority carriers have negligible influence on the majority carrier density and therefore $n_n \cong n_{no}$. The electron density at the *p*-side boundary (x=-x_p) of the depletion region can be obtained using this relation and substituting Equation 2-30 into Equation 2-31:

$$n_p(x = -x_p) = n_{po}\exp(\frac{qV}{kT}) \qquad (2\text{-}32)$$

Similarly, the hole density at the *n*-side boundary ($x=x_n$) of the depletion region can be described as:

$$p_n(x = x_n) = p_{no}\exp(\frac{qV}{kT}) \qquad (2\text{-}33)$$

In the neutral *n*-region, the steady-state continuity equation is given in Equation 2-34:

$$\frac{d^2p_n}{dx^2} - \frac{p_n - p_{no}}{D_p\tau_p} = 0 \qquad (2\text{-}34)$$

where D_p and τ_p is the diffusion coefficient and lifetime of holes, respectively. The hole diffusion length L_p is related to the lifetime τ_p through the diffusion coefficient D_p according to the following formula:

$$L_p = \sqrt{D_p\tau_p} \qquad (2\text{-}35)$$

The general solution of Equation 2-34 is given as:

$$p_n(x) - p_{no} = \mathrm{A}\exp\left(-\frac{x}{L_p}\right) + \mathrm{B}\exp(\frac{x}{L_p}) \qquad (2\text{-}36)$$

Using the boundary conditions of Equation 2-33 and $p_n(x = \infty) = p_{no}$, constant A and B are calculated to:

$$\mathrm{A} = p_{no}\left[\exp\left(\frac{qV}{kT}\right) - 1\right]\exp\left(\frac{x_n}{L_p}\right), \qquad B = 0 \qquad (2\text{-}37)$$

Applying Equation 2-37 into Equation 2-36 yields:

$$p_n(x) - p_{no} = p_{no}[\exp(\frac{qV}{kT}) - 1]\exp(-\frac{x - x_n}{L_p}) \qquad (2\text{-}38)$$

The hole diffusion current density J_p on the *n*-side boundary is then:

$$J_p(x = x_n) = -qD_p \frac{dp_n}{dx} = \frac{qD_p p_{no}}{L_p}[\exp(\frac{qV}{kT}) - 1] \quad (2\text{-}39)$$

Similarly, the electron diffusion current density J_n on the the *p*-side boundary is:

$$J_n(x = -x_p) = qD_n \frac{dn_p}{dx} = \frac{qD_n n_{po}}{L_n}[exp(\frac{qV}{kT}) - 1] \quad (2\text{-}40)$$

The total current is constant throughout the diode and equals to the sum of Equation 2-39 and 2-40:

$$J = J_p(x = x_n) + J_n(x = -x_p) = J_o\left[\exp(\frac{qV}{kT}) - 1\right] \quad (2\text{-}41)$$

where $J_o = \frac{qD_p p_{no}}{L_p} + \frac{qD_n n_{po}}{L_n}$.

Equation 2-41 is known as the ideal diode equation or Shockley equation. It is clear that the current density increases exponentially with forward bias applied on the *p*-side, and saturates at J_o in the reverse direction. J_o is therefore called the diode saturation current density and is a measure of the recombination rate in a device. A diode with a larger recombination rate will have a larger J_o.

2.3.2 Current-voltage characteristic and cell parameters

When a solar cell is exposed to light, electron-hole pairs are generated. Within the minority carrier diffusion length from the boundary of the depletion region, the light generated minority carriers can be separated and collected by the depletion region to create a photocurrent as shown in Figure 2.10 (a). The equivalent circuit is shown in Figure 2.10 (b).

In the dark, the diode equation for an ideal *p-n* junction was given in Equation 2-41

(also shown in Figure 2.10 (b)). Under irradiation, the current density-voltage curve of the solar cell is shifted downward as the light generated current opposes the diode dark current and the total current density is

$$J = J_o \left[\exp(\frac{qV}{AkT}) - 1\right] - J_L \qquad (2\text{-}42)$$

where J_L is the light generated current density and A the diode ideality factor. For an ideal junction, the ideality factor equals to 1 and in realistic devices it usually has a value between 1 and 2 [25]. The current density-voltage characteristics for a solar cell operating in the dark and under illumination are shown in Figure 2.11.

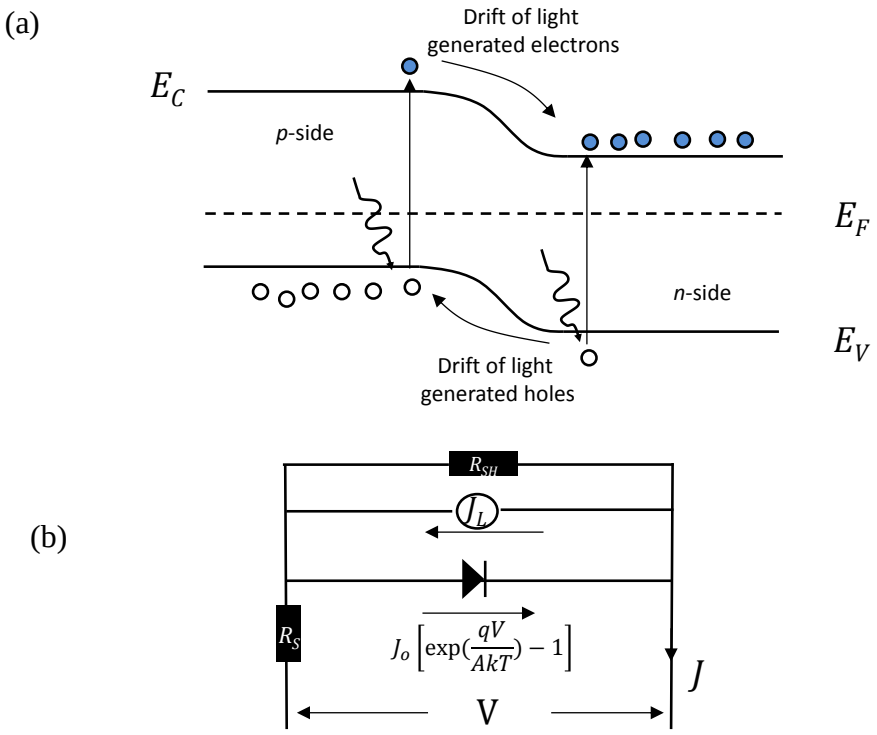

Figure 2.10 (a) Energy band diagram of a solar cell under light irradiation. (b) Equivalent circuit for a real solar cell with inclusion of main parasitic losses represented by series resistance R_S and shunt resistance R_{SH}.

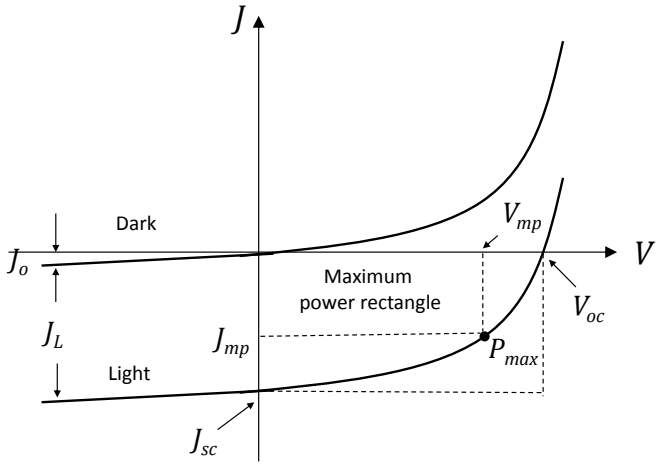

Figure 2.11 Current density-voltage characteristic of a solar cell under irradiation and in the dark.

From Figure 2.11, the primary parameters of the solar cell can be extracted and include short circuit current density J_{sc}, open circuit voltage V_{oc}, fill factor *FF*, and efficiency η.

J_{sc} is the maximum current flowing through a solar cell when no bias is applied. For ideal solar cells, J_{sc} equals the light generated current density J_L, i.e. $J_{sc} = J_L$.

V_{oc} is the applied voltage at which no net current is flowing across the device. From Equation 2-42, V_{oc} can be determined by setting the total current at zero:

$$V_{oc} = \frac{AkT}{q} \ln\left(\frac{J_L}{J_o} + 1\right) \qquad (2\text{-}43)$$

For a given solar irradiation, V_{oc} is found to increase as J_o decreases. As J_o is determined by the rate of minority recombination, V_{oc} is limited by the recombination losses [26].

The *FF* is defined as the ratio of the maximum power P_{max} from the solar cell to the

product of V_{oc} and J_{sc}. From Figure 2.11, *FF* is the ratio of the areas of the two rectangles decided by V_{oc}, J_{sc} and V_{mp}, J_{mp} respectively. This ratio is given in:

$$FF = \frac{V_{mp} \times J_{mp}}{V_{oc} \times J_{sc}} \qquad (2\text{-}44)$$

where V_{mp} and J_{mp} are the voltage and current density yielding the maximum output power P_{max} of the cell. *FF* is therefore a measure of the "squareness" of the *J-V* curve.

The efficiency η is the most commonly used parameter to present the performance of solar cells and is defined as the ratio of the maximum power converted by the solar cell to the incident illumination power P_{in}:

$$\eta = \frac{P_{max}}{P_{in}} = \frac{V_{oc} \times J_{sc} \times FF}{Area\ of\ the\ cell \times incident\ light\ power\ density} \qquad (2\text{-}45)$$

For comparison purposes a simulated air mass (AM) spectrum is usually used to illuminate the cells. The intensity of solar radiation in the free space at the average distance of the earth from the sun is defined by the solar constant, the value of which is 1367 W/m^{-2} [27]. However, the solar radiation is varied in the terrestrial regions due to attenuation effects caused by atmospheric absorption and scattering. The degree of which the atmosphere attenuates the solar radiation reaching the earth's surface is defined as the air mass (AM). The AM0 spectrum is that incident from the sun just outside the Earth's atmosphere. The AM1.5 spectrum is the global average incident at the surface of the Earth. Both AM0 and AM1.5 global spectra are shown in Figure 2.12. The definition of AM1.5 is that the direct optical path length of the

incident light is 1.5 times thickness of the Earth's atmosphere. AM1.5 at a temperature of 25 ℃ is accepted as the standard test condition for all terrestrial photovoltaic applications.

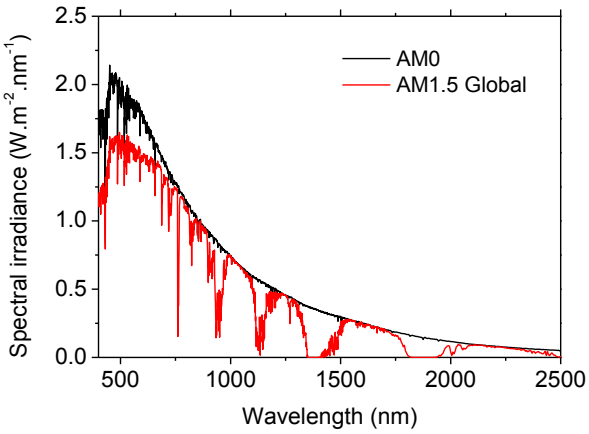

Figure 2.12 AM0 (black line) and AM1.5 Global (red line) spectra (reproduced from ASTM G173-03 Reference Spectra).

2.3.3 Losses in solar cell

2.3.3.1 Parasitic losses

In contrast to the ideal solar cells discussed above, parasitic resistances are always present in real devices (as shown in Figure 2.10 (b)) and cannot be ignored. The major impact of parasitic resistance is to reduce the *FF*. Two resistances, series resistance R_S and shunt resistance R_{SH} are introduced. Considering the resistance losses, Equation 2-42 can be modified to more accurately describe real devices:

$$J = J_o\left[\exp\frac{q(V-JR_S)}{AkT} - 1\right] + \left(\frac{V-JR_S}{R_{SH}}\right) - J_L \qquad (2\text{-}46)$$

Series resistance mainly arises from the resistance of current movement through the

bulk semiconductor and the contact resistance between the semiconductor and metal contact required to complete the circuit. Increasing series resistance clearly has a negative influence on the *FF* of the solar cells. In addition, shunt resistance typically arises from the manufacturing defects that provide the shunting or leakage paths for the light generated current. Low shunt resistance results in a decrease in V_{oc}. The overall impact of parasitic resistance on the device is a reduced the fill factor. The series resistance R_S and shunt resistance R_{SH} experimental determination from the *J-V* curve is explained in Chapter 4.

2.3.3.2 Optical losses

The external quantum efficiency (EQE) is used to determine the number of electrons collected by the solar cell compared to the number of incident photons for a given photon energy incident on the solar cell. Under ideal conditions, every incident photon of energy larger than the energy bandgap generates one electron flowing in the external circuit. However, the real external quantum efficiency is reduced and the measured J_{sc} is smaller than the maximum achievable J_{sc} due to optical losses. EQE is commonly used to describe the different types of losses responsible for a reduction in the measured J_{sc}. Referring to the numbers in Figure 2.13, EQE losses can be divided into the following groups [26, 28]:

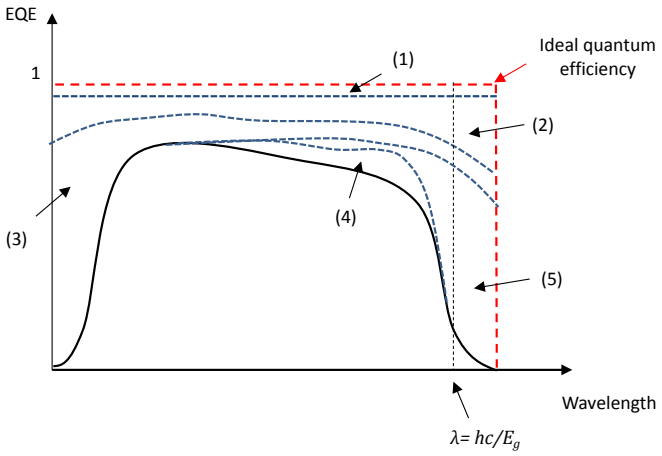

Figure 2.13 External quantum efficiency of a solar cell as function of light wavelength [26].

(1) Shading from the collection grid. Generally, about 10 % of the cell is covered by the front grid and is the only wavelength-independent optical loss.

(2) Reflections from the front contact and interfaces between different constituent layers.

(3) Absorption losses in the front contact layer and window layer. Typically, about 5-10 % of the incident light is lost in these layers [29].

(4) Incomplete collection of photo-generated carriers. The carriers generated in or close to the depletion region can be quickly collected and swept apart by the electric field. If the carriers are generated more than a diffusion length away from the depletion region, they are more likely to recombine and do not contribute photocurrent. Application of a reverse bias increases the depletion width and improves the collection efficiency of photo-generated carriers.

(5) Incomplete absorption in the absorber layer near the absorber bandgap. Since

long wavelength photons penetrate more deeply into the device, some of the long wavelength light will pass through before being absorbed. If the absorber is thinner than $1/\alpha_g$, where α_g is the absorption coefficient just above the bandgap, this loss becomes significant. In addition, high energy photons are prone to be absorbed towards the surface, thus the front surface recombination may take account for a reduction in quantum efficiency in the short wavelength region.

2.4 Summary

The energy band formations and various energy levels in a semiconductor were described at the beginning of this chapter. Photovoltaic devices operate under nonequilibrium conditions with excess carriers generated by incident photons that have energy larger than the energy bandgap of the semiconductor. The mechanism that restores equilibrium is the recombination of the excess minority carriers with the majority carriers.

A *p*-*n* junction is then formed when a *p*-type and an *n*-type semiconductor are brought into contact and act as the basic building block for the photovoltaic device. An electric field from n-side to p-side is formed at the junction. This built-in field, in turn creates a depletion region of mobile carriers. In addition to the homojunction, the formations of heterojunctions and Schottky junctions were also discussed.

A solar cell in dark is similar to a diode and has the same operational principle. Under irradiation, the current-voltage curve of the solar cell is shifted downwards as

current is generated. The losses for real solar cells, including parasitic losses and optical losses were finally described.

Chapter 3

Cu_2ZnSnS_4 material properties and solar cells

In this chapter, the crystal structure, electronic band structure, phase control and intrinsic defects of CZTS are firstly summarised in section 3.1. In section 3.2, the device configuration of a CZTS thin film solar cell and various absorber deposition techniques including vacuum-based and solution-based are reviewed. Section 3.3 details the nanoparticle ink-based deposition techniques, which are used in this work.

3.1 Properties of CZTS absorber material

CZTS is not a new material as its synthesis can be traced back to 1967 [30]. However, it has attracted extensive research focus in recent years ranging from crystal and electronic properties to phase control and intrinsic defects.

3.1.1 Crystal structure

Derived from Cu based chalcogenides such as $CuInSe_2$ (CIS) where half of the indium is replaced by zinc and the other half by tin, CZTS crystallises in a tetrahedrally coordinated structure as shown in Figure 3.1 (a). Each sulphur anion is bonded to four cations and each cation is bonded to four sulphur anions. The periodic packing of atoms in crystals results in various degrees of symmetry, which lead to the definition of space groups. Space groups in three dimensions are made

from combinations of the translational symmetry of a unit cell (including lattice centering), the point group symmetry operations (*i.e.* reflection, rotation, improper rotation), and screw axis and glide plane symmetry operations. The combination of all these symmetry operations results in a total of 230 different space groups describing all possible crystal symmetries [31].

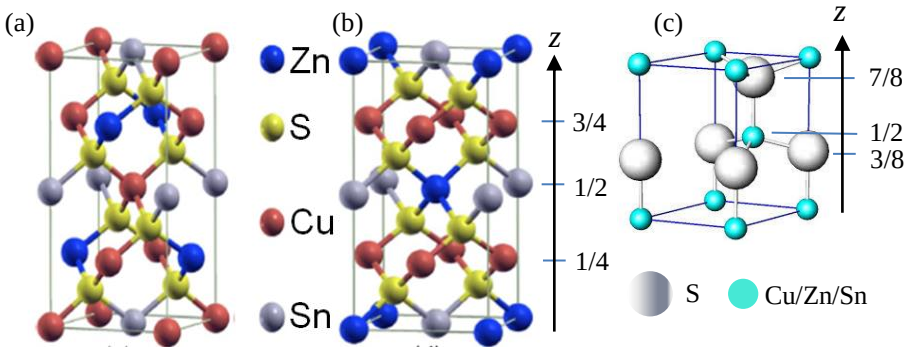

Figure 3.1 Crystal structure of CZTS unit cell (a) kesterite, (b) stannite [32] and (c) wurtzite structure [33].

As shown in Figure 3.1 (a), there are at least two variations for the ordering of the cations: kesterite structure and stannite structure. The kesterite CZTS has a tetragonal crystal structure with space group $I\bar{4}$ where the cation layers alternate as CuSn/CuZn/CuSn/CuZn at z = 0, 1/4, 1/2 and 3/4 respectively (where z is the fractional coordinate along the long c-axis of the structure). In this representation I represents the body centred Bravais lattice and $\bar{4}$ is a rotation-inversion axis that has a rotation angle of 360°/4. Figure 3.1 (b) shows however that for the stannite CZTS structure ZnSn layers alternate with CuCu layers with space group $I\bar{4}2m$. Here, 2 represents the rotation axis with a rotation angle of 360°/2 and m is a mirror symmetry plane that is parallel to the rotation axis 2 [31]. The stannite crystal

structure therefore has a more complicated symmetry than the kesterite structure and is calculated to have a higher energy. Kesterite CZTS thus should be more stable than the stannite structure [34, 35]. Despite this energy difference, kesterite and stannite structure cannot be unambiguously distinguished by X-ray diffraction due to isoelectronic of Cu^{+} and Zn^{2+} [36]. On the other hand, neutrons can distinguish between Cu and Zn atoms by interaction with the nuclei rather than the electron shell. A comprehensive neutron diffraction study showed CZTS to crystalise in a disordered kesterite structure [37]. This disorder mainly arises from the mix occupation of Cu and Zn atom [34, 38]. Thus, stannite structures reported in the literature [39] are most likely a partially disordered kesterite structure rather than an independent and stable crystal structure. In this work, all CZTS in a tetragonal structure is thus defined as kesterite. The lattice data of kesterite CZTS is shown in Table 3.1 and three main characteristic peaks are located at around 28 °, 47 ° and 56 °, respectively.

Table 3.1 Lattice data of single crystal kesterite CZTS (PDF 026-0575).

D(Å)	2θ(degree)	(*hkl*)	I/I_0(%)
5.421	16.34	002	1
4.869	18.21	101	6
3.847	23.10	110	2
3.126	28.53	112	100
3.008	29.68	103	2
2.713	32.99	200	9
2.426	37.03	202	1
2.368	37.97	211	3
2.212	40.76	114	1
2.013	45.00	105	2
1.919	47.33	220	90
1.636	56.18	312	25
1.618	56.86	303	3
1.565	58.97	224	10
1.45	64.18	314	1
1.356	69.23	008	2
1.245	76.44	332	10

Notes: PDF refers to the powder diffraction file, *D is* the distance between two neighbouring parallel planes, 2θ is twice of the Bragg diffraction angle, (*hkl*) are the Miller indices and I/I_0 is the relative peak intensity.

In addition to the kesterite structure, wurtzite CZTS is calculated to have a high energy and as a result, unstable crystal structure [40, 41]. Considering kesterite CZTS unit cell derived from two vertically stacked zinc-blende ZnS unit cells along the c-axis, wurtzite CZTS could be considered as the derivative of wurtzite ZnS. As

shown in Figure 3.1 (c), the position previously occupied by a Zn cation in wurtzite ZnS is replaced by Cu, Zn and Sn cations in CZTS. Metal cations distribute randomly in the sulphur anions hexagonal framework and occupy half of the interstices of the sulphur anions. The lattice data of wurtzite CZTS is shown in Table 3.2. Compared with the kesterite diffraction pattern, three additional peak appear around 26 °, 30 °, and 51 °, which correspond to the (100), (101) and (103) plane of wurtzite CZTS can be used to distinguish between the two atomic arrangements.

Table 3.2 Lattice data of the wurtzite CZTS single crystal [33].

D(Å)	2θ(degree)	(*hkl*)	I/I_0(%)
3.324	26.70	100	100
3.169	28.10	002	84
2.944	30.26	101	87
2.294	39.19	102	28
1.919	47.32	110	81
1.783	51.23	103	54
1.642	56.00	112	47

3.1.2 Electronic properties

Based on CIS, the valence band maximum VBM of CZTS is formed by hybridising S 3*p* and Cu 3*d* states, while the conduction band minimum CBM is derived from antibonding state of S 3*p* and Sn *5s* orbitals [32, 34, 35, 42].

According to the fundamental Shockley-Queisser limit, a single-junction solar cell has a theoretical peak performance of about 33 % under AM 1.5 spectral conditions

[17]. This limit is obtained by balancing the photocurrent produced when an incident photon has sufficient energy to excite an electron across the energy bandgap with the loss mechanisms. In addition to blackbody radiation and radiative recombination, the most significant of these are spectrum losses. Photons with energy less than the energy bandgap pass though the absorber and do not contribute to the photocurrent. Additionally, photons with energy in excess of the energy bandgap create highly energetic electrons which are subject to thermalisation losses as they relax to the band edge. It is thus crucial to choose photovoltaic absorber materials with appropriate energy bandgaps. For single junction solar cells, absorber materials with an energy bandgap between 1 and 2 eV can yield solar energy conversion efficiency in excess of 20 % as shown in Figure 3.2 [17]. CZTS has a near optimum direct energy bandgap of 1.5 eV with maximum conversion efficiency of greater than 30 %.

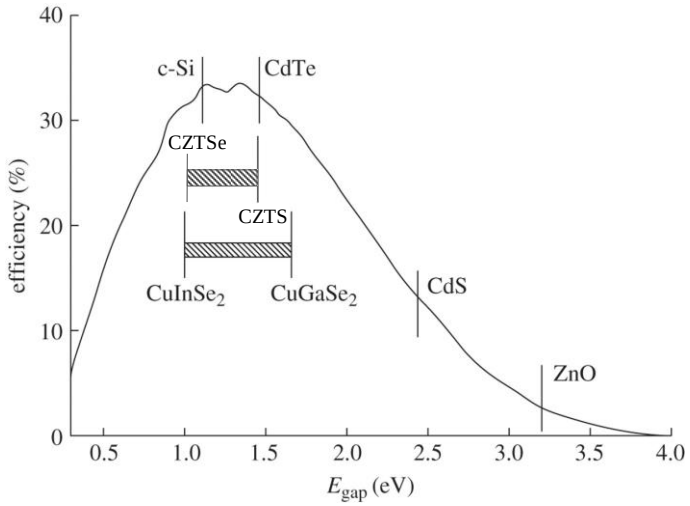

Figure 3.2 Theoretical efficiency limits for single junction solar cells under AM1.5 illumination[17]. Different materials of CZTS, CIGS, CdTe, c-Si, CdS and ZnO with reported energy bandgaps are shown for comparison. Note that the bandgap of the CIGS and CZTS system can be tuned by controlling the In/Ga and Se/S ratio, respectively, and this is shown by the marked areas.

The ideal energy bandgap also provides CZTS a high optical absorption coefficient of more than 10^4 cm^{-1} in the photon energy range greater than the energy bandgap [4, 43, 44]. Such a direct bandgap and high absorption coefficient reduces the thickness of absorber material needed to absorb the incident light hence reducing material costs and panel weight.

3.1.3 Intrinsic defects in CZTS

As a quaternary compound, CZTS is reported to be heavily doped with the presence of a large concentration of intrinsic defects [45, 46]. Only point defects such as vacancies, antisites and interstitials are discussed here. Vacancy defects are lattice sites which would be occupied by A atoms, but are vacant, i.e. V_A. Antisite defects occur in an ordered alloy when A atoms occupies the position which would be

occupied by B atoms, i.e. A_B. Interstitial defect is A atom that occupy a site in the crystal structure at which there is usually not an atom, i.e. A_i. To further explain the compositional dependence of the solar cell efficiency, it is necessary to study defect properties in CZTS. Although very little experimental work is available, theoretical studies on the defects in CZTS are obtained from density functional theory [47-50].

All possible intrinsic defects in CZTS can be divided into two groups: (1) negatively charged defects such as Cu_{Zn}^{-}, Cu_{Sn}^{-}, Zn_{Sn}^{-}, V_{Cu}^{-}, V_{Sn}^{-} and V_{Zn}^{-},which act as acceptors and (2) positively charged defects such as Zn_{Cu}^{+}, Sn_{Cu}^{+}, Sn_{Zn}^{+},V_S^{+}, Cu_i^{+}, Zn_i^{+}, and Sn_i^{+} which act as donors. The calculated formation energies of all defects in CZTS are summarised in Figure 3.3 (a), which shows that all acceptor defects have lower formation energy than that of donor defects. This supports experimental observations that CZTS is an intrinsic *p*-type semiconductor. Furthermore, Cu_{Zn} has the lowest energy arising from the small chemical difference between Cu and Zn atoms. Thus Cu_{Zn} is the dominant defect in stoichiometric CZTS with an acceptor level 0.12 eV above the VBM as shown in Figure 3.3 (b). However, the deep level of Cu_{Zn} may decrease the open-circuit voltage thereby degrading photovoltaic performance. Therefore, Cu-poor and Zn-rich growth conditions should be applied to enhance the formation of V_{Cu}, which has a shallow acceptor level 0.02 eV above VBM. This explains why a Cu-poor and Zn-rich composition, which is not a favour region for single CZTS growth, is widely reported for best solar cells.

Despite the large concentration of intrinsic defects, 98% charge compensation is

observed in CZTS thin films where the negatively charged acceptors are compensated by positively charged donors [46]. In the Cu-poor and Zn-rich growth condition, [V_{Cu}^{-}+Zn_{Cu}^{+}] suppresses [Cu_{Zn}^{-}+Zn_{Cu}^{+}] becoming the dominant complexes [48]. These complexes passivate the Zn_{Cu}^{+} deep donor level (0.15 eV below the CBM), which may act as traps of free carriers or recombination centres and reduce device efficiencies [38, 49].

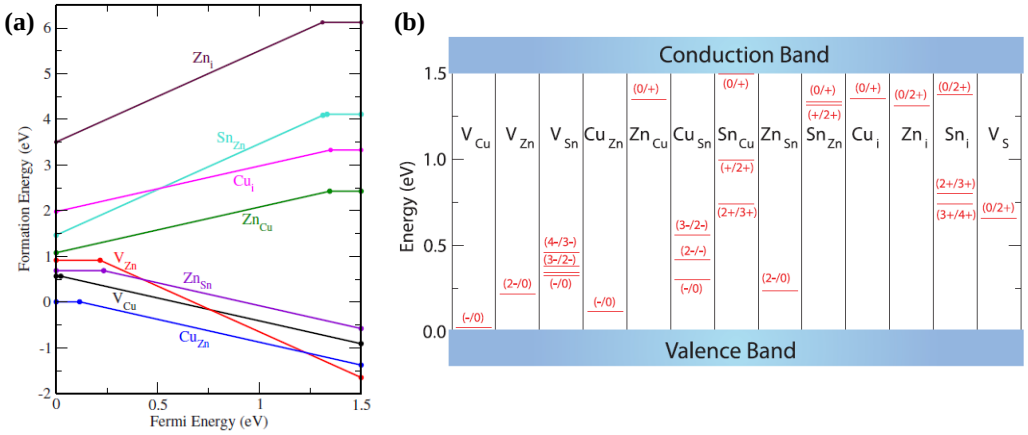

Figure 3.3 (a) Formation energy of intrinsic defects in CZTS as a function of the Fermi energy [48], (b) The ionization levels of intrinsic defects in the bandgap of CZTS [51].

3.1.4 Bandgap engineering of $Cu_2ZnSn(S,Se)_4$

As shown in Figure 3.2, bandgap tuning has been widely and successfully employed in the fabrication of CIGS thin film solar cells by substitution of In by Ga [52-57]. Similarly, various methods have been employed to tune the energy bandgap of CZTS. Firstly, the energy bandgap of CZTS nanocrystal has been controlled by incorporating Ga into the CZTS lattice [58]. In addition, the bandgap of CZTS shows a shift to higher energy due to the quantum confinement when the nanoparticle

diameter is less than the Bohr exciton radius of CZTS (~ 3 nm) [59, 60]. Furthermore, by incorporating Se into CZTS lattice, the energy bandgap of the sulphur-selenium alloy CZTSSe can be tuned from 1.5 to 1.0 eV [61-66]. The fully selenised material is known as $Cu_2ZnSnSe_4$ (CZTSe) when 100 % of the sulphur replacement is completed and the bandgap narrows to 1.0 eV [34, 67].

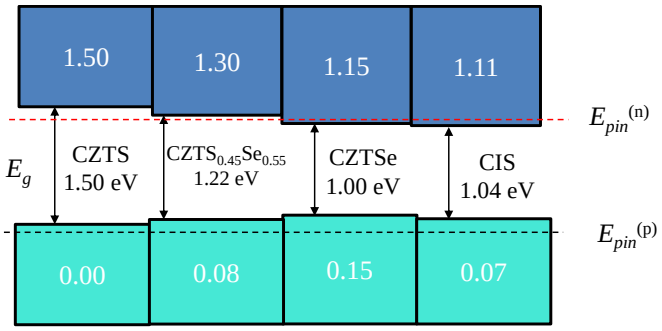

Figure 3.4 Band alignments of CZTS, $CZTS_{0.45}Se_{0.55}$, CZTSe and CIS. The numbers in the boxes are the energy in eV relative to the reference energy level of 0 eV. The dashed line near CBM shows the pinning energy of the Fermi level for *n*-type doping ($E_{pin}^{(n)}$) while the dashed line below VBM is the pinning energy of the Fermi level for *p*-type doping ($E_{pin}^{(p)}$). It is difficult to make a semiconductor *n*-type doped if $E_{pin}^{(n)}$ is located below the CBM and similarly it is difficult to make it *p*-type doped if the $E_{pin}^{(n)}$ is above CBM.

Figure 3.4 is provided to understand the bandgap tunability from CZTS to CZTSe. The band alignment between CZTS and CZTSe is type I, in which the VBM is higher and the CBM is lower for the selenide compared to that of the sulphide. As shown in Figure 3.4, a CBM offset (0.35 eV) and a smaller VBM offset (0.15 eV) is observed in CZTSe compared with CZTS. As the VBM of Cu based chalcogenides is formed by hybridising the S/Se *p* orbitals and Cu *d* orbitals, the lower level of S *p* obital than that of Se *p* obital results in the VBM of the sulphide being lower than

that of the selenide. On the other hand, the CBM of CZTS and CZTSe is the formed by antibonding state of the S/Se *p* and Sn *s* states. The small atom radius of S results in a shorter bond length of Sn-S compared with Sn-Se, which makes the hybridised *s-p* state higher energy in sulphide and moves its CBM up relative to the selenide. The CBM downshift combined with the VBM upshift results in a reduced bandgap as the Se content increases in the $CZTS_xSe_{1-x}$ alloy. Furthermore, the relationship between the bandgap shift and the S composition x is expected to be approximately linear [64]. Depending on the energy bandgap values of CZTS and CZTSSe given in Figure 3.4, the energy bandgap of $CZTS_{0.45}Se_{0.55}$ is estimated to be 1.22 eV, which agrees well with the literature value of 1.18 eV [61].

Although the bandgap narrows from the optimal bandgap of ~ 1.5 eV, the incorporation of Se into CZTS lattice has be found to improve the device performance from 8.4 % [8] of pure CZTS absorber to 12.6 % using CZTSSe as the absorber layer [15]. Chen *et al.* proposed two possible explanations for this conversion efficiency enhancement [49, 64]. Previous calculations have shown that the Fermi-level pinning energy $E_{pin}^{(n)}$ for *n*-type doping in chalcopyrites is located above the CBM of CIS as shown in Figure 3.4 [68]. Since kesterite CZTS and CZTSe have similar electronic structures to the CIS, it is assumed that the $E_{pin}^{(n)}$ lines up for CIS and kesterite compounds. CZTSSe thus could possibly be *n*-type doped due to the selenium incorporation. As shown in Figure 3.4, CZTSe has a CBM below $E_{pin}^{(n)}$ and thus it could exist in *n*-type form like CIS. If this prediction is

correct, type-inversion to *n*-type conduction should be possible at the surface of the *p*-type CZTSSe absorber layer which would facilitate electron-hole separation of photo-generated carriers in CZTSSe thin film solar cells. Additionally, the dominant antisite defect of Cu_{Zn} in stoichiometric CZTSSe has a relatively shallow acceptor level than CZTS due to relatively higher VBM of CZTSSe and weaker *p-d* hybridisation between Se and Cu. Both the facile electron-hole separation and shallow acceptor level are positive for solar cell performance and offer possible reasons for the observed high efficiency of CZTSSe based solar cells.

3.1.5 Phase control

Investigation of the phase diagram of the Cu_2S-ZnS-SnS_2 system shown in Figure 3.5 indicates that single-phase CZTS can only grow in a very narrow region [69].

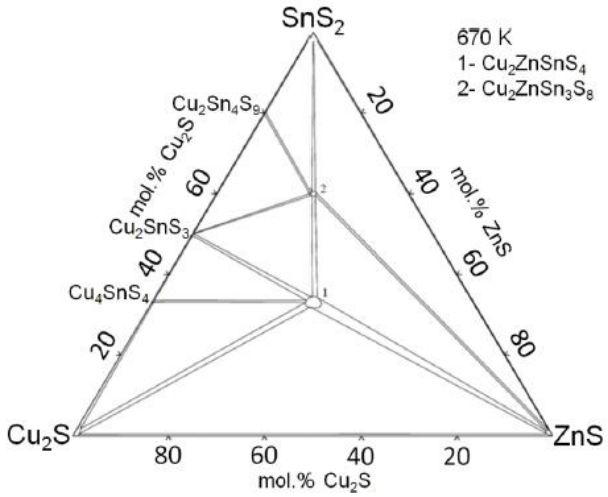

Figure 3.5 Phase diagram of Cu_2S-ZnS-SnS_2 system [69].

Consequently, it is a challenge to synthesis high quality single phase CZTS without

secondary binary and ternary phases such as ZnS, SnS_2 and Cu_2Sn_S [70-72]. Inhomogeneity due to the presence of these secondary phases is assumed to contribute to the relatively low efficiency currently observed in CZTS solar cells [73]. As a result, accurate proper phase control will offer a route to improve the efficiency of CZTS thin film solar cells. However, a further complication is that identifying secondary phases such as cubic Cu_2SnS_3 and zincblende ZnS is difficult as they share diffraction peaks with kesterite CZTS [74]. Therefore, Raman spectroscopy is commonly used to characterise the CZTS phase in combination with XRD diffraction [75-78].

In addition to the experimental phase diagram, the stable atomic chemical potential region of CZTS has been theoretically calculated [47-51]. To maintain stoichiometric CZTS, the following equation must be satisfied:

$$2\mu_{Cu} + \mu_{Zn} + \mu_{Sn} + 4\mu_S = \Delta H_f(\text{CZTS}) = -4.21\text{eV} \qquad (3\text{-}1)$$

where μ_i is the chemical potential of Cu, Zn, Sn, and S referenced to the most stable phases. μ_i equals to 0 when the element is so rich that the pure solid phase can be formed. ΔH_f(CZTS) represents the formation enthalpy of CZTS crystals.

Furthermore, to avoid the formation of competitive secondary phases such as CuS, ZnS, SnS and Cu_2SnS_3, the following relations must be satisfied:

$$\mu_{Cu} + \mu_S < \Delta H_f(\text{CuS}) = -0.49\ \text{eV} \qquad (3\text{-}2)$$

$$\mu_{Zn} + \mu_S < \Delta H_f(\text{ZnS}) = -1.75\text{eV} \qquad (3\text{-}3)$$

$$\mu_{Sn} + \mu_S < \Delta H_f(SnS) = -1.01eV \qquad (3\text{-}4)$$

$$2\mu_{Cu} + \mu_{Sn} + 3\mu_S < \Delta H_f(Cu_2SnS_3) = -2.36eV \qquad (3\text{-}5)$$

Considering all these constraints, the formation of CZTS is restricted in a narrow region as shown by the area ABCD in Figure 3.6.

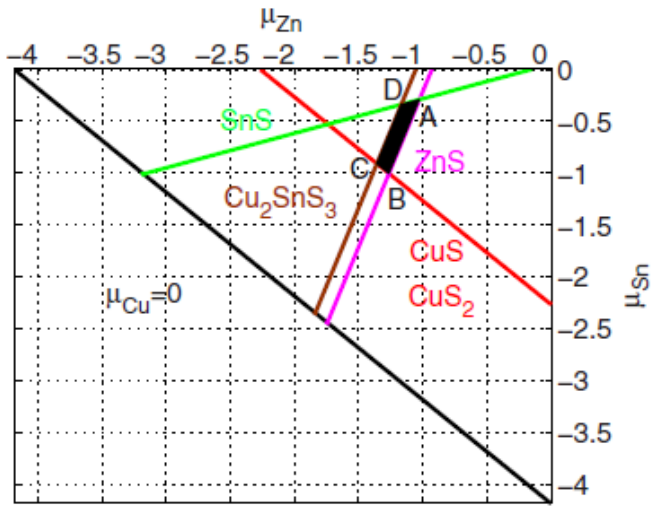

Figure 3.6 The stable chemical potential region of CZTS in a two dimensional Cu-rich plane i.e. μ_{Cu}= 0 [49]. The unit of chemical potential is eV.

The black region in Figure 3.6 is the chemical potential stable region for CZTS, which is small and surrounded by the formation of secondary phases such as CuS, ZnS, SnS and Cu_2SnS_3. In addition, as the stable region along the μ_{Zn} axis for CZTS crystal growth is very narrow (~ 0.3 eV) compared with that of Sn, it is crucial to control Zn composition during the fabrication process. Zn-rich leads to ZnS formation, while Zn-poor leads the formation of Cu_2SnS_3. The narrow thermodynamic window again demonstrates that it is challenging but important to carefully control the growth composition to synthesis high quality single CZTS.

However, contrary to the prediction in Figure 3.6 that Cu-rich and Zn-poor is required to maintain stable CZTS single phase, the highest performance solar cells have been prepared with a Cu-poor and Zn-rich composition region: Cu/(Zn+Sn) = 0.75-0.85 and Zn/Sn = 1.05-1.25 as indicated by the dark hexagon in the Figure 3.7. In this case, ZnS(e) should be the main competing phase and experimentally found in the thin films [79]. As it has wide bandgap, ZnS(e) is not detrimental to the open circuit voltage of the solar cells. However, it may play a role in the high series resistance observed in CZTSSe solar cells [5].

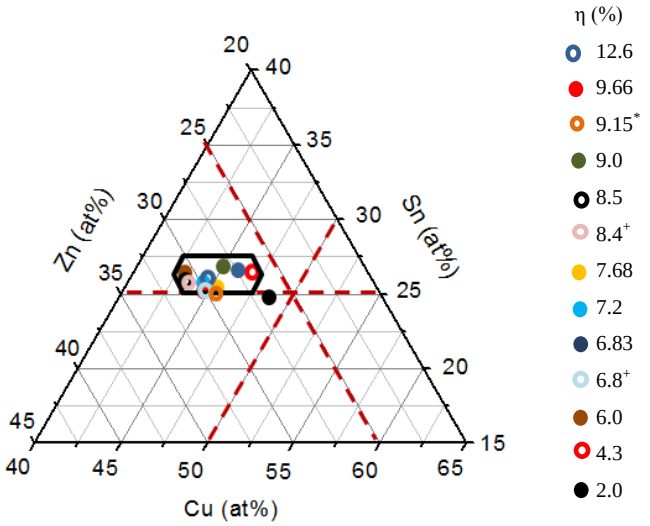

Figure 3.7 Efficiency map of CZTSSe thin film devices on the ternary phase diagram based on the atomic percentage of Cu, Sn, and Zn in the samples [45]. The most common compositional ranges suitable for high efficiency photovoltaic devices are indicated by the dark hexagon. The absorber of the devices indexed with * and $^{+}$ are pure CZTSe and CZTS, respectively. References and process details are given in Table 3.3.

Table 3.3 Comparison of CZTSSe thin film solar cells.

Group	η (%)	Cu/(Zn+Sn)	Zn/Sn	Absorber	Film formation
Wang [15]	12.6	0.8	1.1	CZTSSe	Annealed precursor films
Todorov [13]	9.66	0.8	1.22	CZTSSe	Annealed precursor films
Repins [9]	9.15	0.86	1.15	CZTSe	Thermal evaporation
Miskin [16]	9.0	0.82	1.05	CZTSSe	Selenised nanocrystal films
Cao [11]	8.5	0.77	1.2	CZTSSe	Selenised nanocrystal films
Shin [8]	8.4	0.77	1.2	CZTS	Thermal evaporation
Embden [80]	7.68	0.85	1.12	CZTSSe	Selenised nanocrystal films
Guo [10]	7.2	0.79	1.11	CZTSSe	Selenised nanocrystal films
Tian [81]	6.83	0.87	1.03	CZTSSe	Selenised nanocrystal films
Wang [6]	6.8	0.82	1.2	CZTS	Thermal evaporation
Cao [11]	6.0	0.76	1.17	CZTSSe	Selenised nanocrystal films
Yang [82]	4.3	0.89	1.02	CZTSSe	Selenised nanocrystal films
Cao [11]	2.0	0.94	1.08	CZTSSe	Selenised nanocrystal films

3.2 CZTS solar cells

3.2.1 Device configuration

A schematic structure of a typical thin film CZTS solar cell in substrate configuration is shown in Figure 3.8. At the bottom of the device, a Mo layer with thickness of ~ 1 μm is usually sputtered on a soda lime glass (SLG) substrate to provide a electrical back contact. Mo is chosen because of its high conductivity and stability in harsh conditions up to 900 ℃. However, Mo is not entirely inert during the high temperature selenisation process and a thin $Mo(S,Se)_2$ interfacial layer is widely found between the Mo and CZTSSe absorber layer [11, 14-16]. This thin layer is thought to provide a lower resistance contact for holes than bare Mo and establish a back surface field to reduce the recombination of electrons at the back contact [83]. However, too thick a $Mo(S,Se)_2$ layer will limit the device performance due to its high resistivity and weak adhesion [84, 85]. Above the Mo substrate, the absorber layer is a *p*-type thin film made from CZTS, CZTSe or CZTSSe, which are here all defined as kesterite. Typically, the absorber thin film ranges from 1 μm to 2 μm in thickness. To form the *p*-*n* junction, an *n*-type cadmium sulphide (CdS) layer is deposited on top of the *p*-type absorber layer usually by chemical bath deposition. The surface of CZTS thin film is too rough to be fully covered by CdS thin film, leading to shorting between the front contact and back contact. To mitigate this, an intrinsic ZnO (i-ZnO) layer with thickness around 50 nm is usually sputter-coated on the CdS followed by a TCO (transparent conducting oxide) layer of Indium Tin

Oxide (ITO) or Al-doped ZnO (AZO). The TCO layer allows electrons to flow in the horizontal plane towards the front contact. A highly conductive Al/Ni bilayer front contact is finally deposited to minimise series resistance and increase the current collection. In high performance solar cells, an anti-reflection coating of MgF_2 layer may also be applied to reduce optical losses [15].

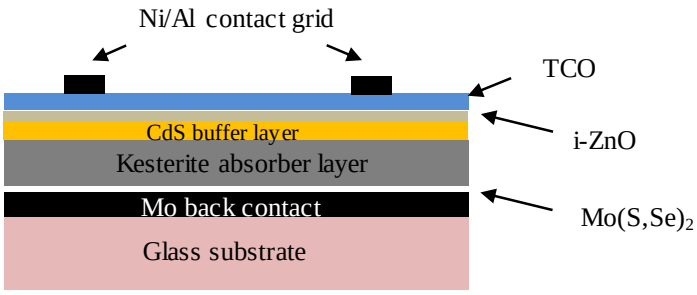

Figure 3.8 Schematic structure of a typical CZTS solar cell.

3.2.2 Absorber deposition techniques

Despite the relatively small region of stability in the phase diagram, numerous techniques have been attempted to deposit the kesterite absorber thin films for solar cells. The reasonably successful film deposition methods can be roughly divided into two categories: vacuum-based and solution-based deposition approaches.

3.2.2.1 Vacuum-based techniques

Vacuum-based techniques have been widely applied for the deposition of kesterite thin films [43, 86]. Furthermore, the progress and experience achieved for CIGS solar cells manufactured using vacuum-based methods can be readily transferred.

Vacuum-based fabrication techniques normally involve deposition of the constituent atoms on a substrate at certain pressure and temperature. Various high vacuum techniques have been developed to deposit the kesterite thin films that are suitable for photovoltaic applications such as sputtering [4, 43, 67, 87-89], thermal evaporation [6, 9, 79, 90, 91], electron beam evaporation [92] and pulsed laser deposition [93].

Vacuum techniques have the advantage of easily controlling the chemical composition in the thin films and normally have good reproducibility. However, high vacuum techniques require a large capital investment and considerable energy to deposit thin film from the target sources.

3.2.2.2 Solution-based techniques

Compared with vacuum-based methods, solution-based deposition and processing provides an appealing alternative with relatively high throughput, low energy consumption and cost. These methods include electrodeposition [94-97], spray pyrolysis [98, 99], sol-gel [100-102], spin-coating of precursor solutions [13-15, 81, 103-105], and nanoparticle inks [40, 106-110]. A summary of these techniques and associated device efficiencies are listed in Table 3.4. Compared with vacuum-based, solution-based techniques operate at lower temperature and have the potential to suppress the volatilisation of the constituents.

Table 3.4 Highest efficiencies achieved for CZTS solar cells prepared by different methods.

Methods	η (%)	Absorber	Year
Sputtering [89]	6.77	CZTS	2008
Evaporation [9]	9.15	CZTSe	2012
Pulsed laser deposition [93]	3.14	CZTS	2011
Electrodeposition [96]	7.3	CZTS	2012
Sol-gel [102]	2.23	CZTS	2012
Hydrazine [15]	12.6	CZTSSe	2013
Precursor deposition [105]	11.2	CZTSSe	2015
Nanoparticle based [16]	9.0	CZTSSe	2014

Extra material such as SnS is not needed in solution-based methods to prevent the decomposition of CZTS at high temperature in vacuum [79]. As shown in Table 3.4, solution-based techniques demonstrate high performance that is comparable to or even better than those produced by vacuum-based methods. Among the variety of solution-based techniques, the best results are observed for hydrazine-based method with efficiency up to 12.6 % [15]. An obvious drawback of this technique however is that hydrazine is an explosive and toxic solvent. Compared with this method, CZTS nanoparticle inks offer an attractive non-toxic route to fabricating the absorber layer. The highest reported efficiency for CZTS nanoparticle inks currently stands at 9.0 %.

The parameters of these two devices are compared in Table 3.5.

Table 3.5 Device characteristics of the current world record CZTSSe solar cells (a) hydrazine-based method, (b) nanoparticle ink-based method.

Cell	η (%)	V_{oc} (mV)	J_{sc} (mA/cm^2)	FF (%)	R_S (Ω.cm^2)	A	E_g (eV)	E_g-qV_{oc} (eV)
a	12.6	449	35.2	69.8	0.72	1.24	1.13	0.617
b	9.0	404	35.1	63.7	-	1.54	1.10	0.696

More importantly, among all the solution-based techniques, nanoparticle inks currently provide the only approach that enables the phase formation to occur prior to the film deposition. In carefully controlled reaction conditions, kesterite nanoparticles are firstly fabricated in a liquid environment, which means the constituent elements have high diffusivity and can achieve a thermodynamically stable phase. In other solution-based methods, it is molecular or molecular/particle slurries deposited on the substrate and to complete the phase formation requires one or more reactions taking placing in the solid films. Compared with nanoparticle inks, there is a higher reaction barrier and lower diffusivity making it more challenging to obtain a stable CZTS single phase thin film. The post synthesis washing treatment in the nanoparticle based method can remove most of the precursor chemicals before thin film deposition. However, it may be difficult to remove residual chemicals in thin films deposited from molecular solutions found in other solution-based techniques. The nanoparticle ink based technique therefore provides a feasible and

reliable route to achieve high quality photovoltaic materials and ultimately competitive photovoltaic devices.

3.3 Kesterite absorber layer from nanoparticle inks

The nanoparticle ink-based process starts with the controlled synthesis of nanoparticles and finishes with the post treatment of the thin films deposited from the nanoparticle inks [10, 16]. As the nanoparticle inks can be sprayed [110, 111], dip-coated [112], doctor bladed [10, 113] or spin coated [11] into thin films under ambient laboratory conditions, it is potentially compatible with high volume manufacturing for the production of kesterite thin film solar cells.

3.3.1 CZTS nanoparticle synthesis

The CZTS nanoparticle synthesis can be generally divided into two major approaches: synthesis of hydrophilic CZTS nanoparticles based on solvothermal methods [107, 114, 115] and formation of hydrophobic colloidal nanoparticles based on a thermolysis technique [74, 109, 111]. In the hydrophilic case, glycol and polyvinylpyrrolidone (PVP) is widely used as a solvent and ligand system providing nanoparticle good dispersibility in polar solvents. Specially, an in-situ self-stabilisation method using $Sn_2S_6^{4-}$ and $Sn_2S_7^{6-}$ as the self-component ligands provides aqueous CZTS inks where water is the only solvent [114]. Unfortunately, the hydrophilic nanoparticle inks are reported to yield inferior device performance because of the relatively low quality thin film (agglomerates on film surface or

cracks) formed on deposition [116, 117]. In the hydrophobic system however, it is the inorganic crystalline nanoparticle in the centre coated with an organic ligand layer, such as oleylamine (OLA), that prevent aggregation and provides dispersibility in nonpolar solvents. Using the hydrophobic technique to produce colloidal CZTS nanoparticles has recently resulted in an impressive device efficiency of 9.0 % [16].

Hydrophobic colloidal nanoparticle synthesis is typically performed in a batch reaction in an organic solvent under air-free conditions. This is achieved by using a multi-necked flask with one neck connected to a multi-valve manifold that can be used to either purge the reaction chamber with an inert gas or pull vacuum to evacuate volatiles from the reaction medium (commonly called a Schlenk line). The solvent is de-gassed and heated under inert atmosphere before other precursors are later injected into the hot solvent where they quickly react.

For the metal precursors, metal acetylacetonates $Cu(C_5H_7O_2)_2$, $Zn(C_5H_7O_2)_2$, $Sn(C_5H_7O_2)_2Cl_2$ are widely adopted. The ligand acetylacetonate is normally abbreviated into acac, and the metal complexes have the simplified formulae $Cu(acac)_2$, $Zn(acac)_2$, and $Sn(acac)_2Cl_2$. Typically, both oxygen atoms in the acetylacetone molecule bind to the metal atom to form a six-membered chelate ring as shown in Figure 3.9.

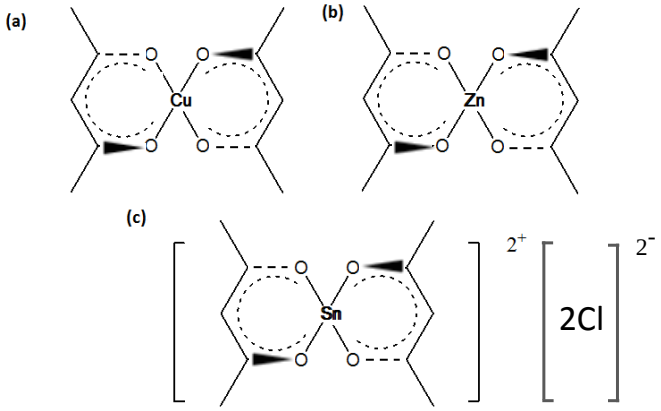

Figure 3.9 Molecular structure of (a) $Cu(acac)_2$, (b) Zn $(acac)_2$, and (c) $Sn(acac)_2Cl_2$.

For the solvents, oleylamine (OLA) acts as a versatile reagent for the synthesis of various colloidal semiconductor nanoparticles [118-120], while trioctylphosphine oxide (TOPO) [74, 112], octadecane (ODE) [78] and octadecylamine (ODA) [75] are also occasionally used. The molecular structure of OLA is depicted in Figure 3.10. The high boiling point of OLA (348-350 ℃) allows the possibility to employ strong heating conditions if necessary.

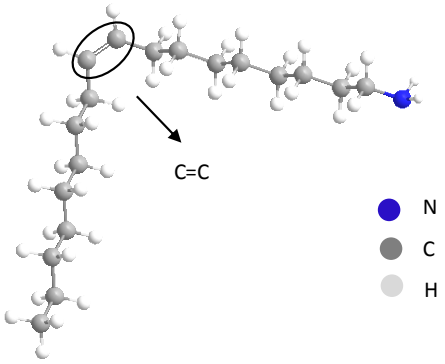

Figure 3.10 Chemical structure of cis-isomer OLA ($CH_3(CH_2)_7CH=CH(CH_2)_8NH_2$).

In the reaction system, OLA acts as not only the solvent for the metal precursors and sulphur, but also as the surfactant and a mild reducing agent. A schematic illustration of the solvent, reductant and surfactant role of OLA in the synthesis is shown in Figure 3.11 (taking Cu^{2+} as the metal cation for example).

(1) Solvent: OLA can form complexes with metal cations at moderate temperature, which can be used as nanoparticle precursors.

(2) Reductant: OLA serves as a reducing agent by transferring one electron of the amine to the metal cation at relatively high temperature.

(3) Surfactant: OLA is a long-chain primary alkenylamine. It can passivate the surface of nanoparticles through the coordination of the lone pair electrons on the N atom of the amine [121].

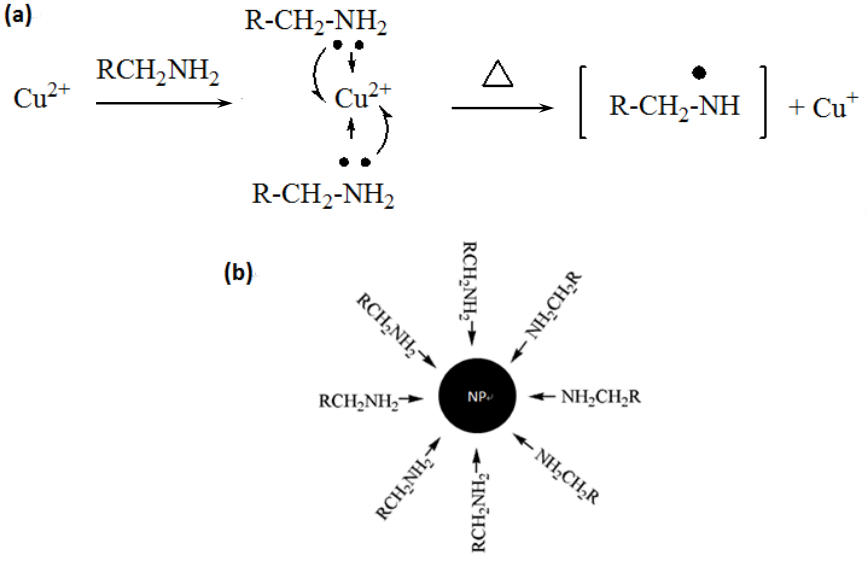

Figure 3.11 Schematic illustration of the role of OLA in the nanoparticle synthesis as: (a) a solvent and reductant, and (b) a surfactant. (R=$C_{17}H_{33}$, Δ= heat).

Incorportation of sulphur into the reaction system can be achieved by simply dissolving elemental sulphur directly into OLA although other sources such as dodecanethiol (DDT) [78, 122], can be used.

3.3.2 Absorber formation

To fabricate the absorber layer, the as-synthesised CZTS nanoparticle inks are first deposited on the substrate to form a dry nanoparticle precursor thin film followed by a high temperature treatment. Various methods have been reported for the nanoparticle deposition stage. Drop-casting is straightforward although difficult to produce uniform and crack free films [109, 123]. Doctor-blading allows rapid production of absorber layers thicker than 1 mm, which is too thick for thin film photovoltaic applications [10, 113, 124]. Spray coating is found to yield precise control over film thickness and can be readily applied to larger substrates that are compatible with high volume manufacturing [111]. Spin-coating can efficiently yield uniform and crack free thin films. In this work, nanoparticle inks are applied onto a substrate by spin-coating followed by a soft-bake to remove the residual solvent [11]. The spin-coating and soft-baking procedures are repeated several times to yield the thin film with desired thickness.

Although the aforementioned soft-baking procedure removes most of the ligand on the nanoparticle surfaces, the as-deposited CZTS nanocrystal thin film has poor optoelectronic properties due to the large number of grain boundaries within the

nanocrystal thin film. Without post heat treatment the best CZTS devices efficiency stands at only 0.23% [111]. The large surface area of the nanoparticles, which serve as recombination centres and scattering sites for carriers, are the reason for such inferior device performance. For photovoltaic applications, it is desirable for the absorber film to have large grains which facilitate the transport of photo-generated carriers while minimising grain boundary recombination. To induce grain growth, the CZTS nanoparticle thin films are therefore subject to thermal annealing in the presence of selenium, which is known as selenisation. The treatment temperature is typically reported around 500 ℃ for a period of about 20 minutes under an inert gas atmosphere [10, 80, 114].

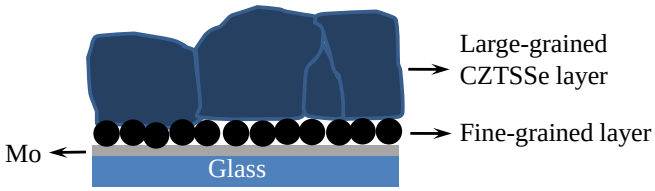

Figure 3.12 Schematic illustration of the nanoparticle precursor thin film on Mo-coated glass after selenisation.

After selenisation, a bilayer structure is generally generated with an upper large-grained layer and a lower fine-grained layer [16, 80] as shown in Figure 3.12. The upper large-grained layer is reported to be composed of a CZTSSe phase. Ideally, the CZTSSe grains are large enough to yield a single monolayer, which can eliminate the boundaries lying across the direction of carrier transport. Furthermore, the upper large-grained layer acts as the optical absorber, which means that it is only this layer

that contributes to the photocurrent [125]. Increasing the thickness of the effective large-grained layer is thought to improve the device performance by enhancing the absorption of the low energy photons. Below the upper micron-scale grains is the fine-grained layer composed of metal-chalcogenide nanocrystals and a carbon rich matrix [11, 126]. The involvement of carbon, via the long chain ligands, is expected to be the main cause of the unique bilayer morphology exhibited by the selenised thin films as no such bottom fine-grained layers are obtained in carbon free techniques [15, 114]. To eliminate the fine-grained layer, which generates no photocurrent but increases the series resistance, further work is required to change the capping ligands either in ink preparation or in the earlier nanoparticle synthesis.

3.4 Summary

Kesterite materials, such as CZTS, CZTSe, and CZTSSe compounds, are experiencing rapid improvement because of the abundant constituent elements and promising optoelectronic properties. Currently, solar cell efficiencies of 12.6 % have been achieved, which is close to the performance metric that is considered interesting for commercialisation. Considerable studies have been conducted both experimentally and theoretically to provide the necessary detailed understanding of these materials. Due to the narrow single phase region and limited knowledge of defects, it is challenging to grow single phase kesterite material with controlled native defects. Finally, various approaches have been attempted to form kesterite thin films from vacuum-based to solution-based techniques. Nanoparticle inks represent a

non-toxic and feasible method to provide high performance devices. By optimising the nanoparticle synthesis and film selenisation treatment, this technique has the potential to enable widespread adoption of CZTS solar cell technology.

Chapter 4

Characterisation techniques

This chapter describes characterisation techniques used throughout this work. The characterisation techniques used in this study can be divided into two groups: material properties and device performance. Material characterisations include morphological study using electron microscopy and atomic force microscopy (AFM); crystal structure using X-ray diffraction (XRD) and Raman spectroscopy; composition using energy dispersive X-ray spectroscopy (EDS), X-ray photoelectron spectroscopy (XPS), and secondary ion mass spectroscopy (SIMS); and optical properties using transmittance-reflectance spectroscopy. Device characterisation includes current-voltage (I-V), capacitance voltage (C-V), and external quantum efficiency (EQE).

4.1 Material characterisation

4.1.1 Electron microscopy

The resolution limit of optical microscopy is determined directly by the incident light wavelength as shown in Equation 4-1 [31]:

$$d = \frac{0.61\lambda}{NA} \qquad (4\text{-}1)$$

where d is the resolvable distance, λ is the wavelength of the light source, NA is

numerical aperture that can be determined by the lens system. The maximum values of *NA* are of the order of 0.95 for lenses operating in air [31]. Limited by the wavelength of visible light (~ 400 nm), optical microscopy has maximum resolution about 0.25 μm, which is unacceptably low for the morphology of nanostructured material. Using accelerated electrons as the source, the electron microscope extends the resolution to a scale of several nanometres or even the lattice planes.

4.1.1.1 Transmittance electron microscopy

Transmittance electron microscopy (TEM) has analogous imaging principles to optical microscopy. However, the electron beam source is at the top of the microscopy vacuum column while the recording system is at the bottom as shown in Figure 4.1.

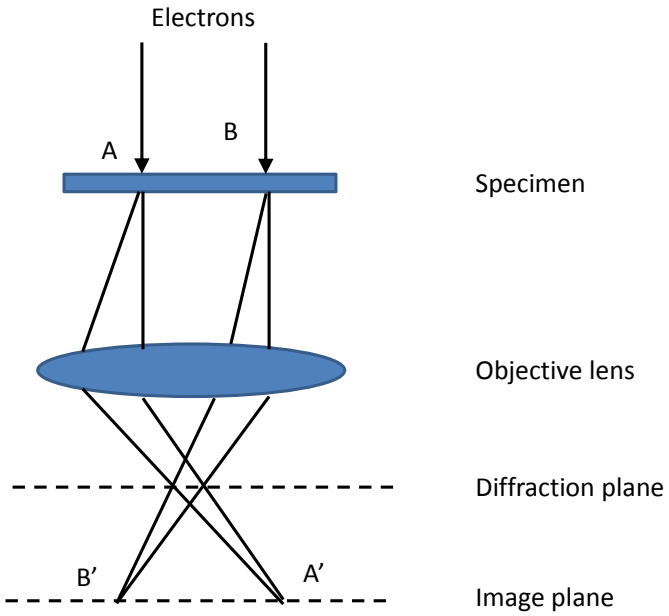

Figure 4.1 Schematic diagram of TEM optics.

All rays scattered from a single point in the sample are brought into focus at a conjugate point in the image plane. Typically, TEM is maintained at a high voltage (100-400 kV), which enables the examination of fine structures. For example, the wavelength of electrons at 100 kV is 0.0037 nm and provides a potential resolution of 0.2 nm. Furthermore, all rays scattered in a given direction from all points in the sample are brought to focus at a single point in the back focal plane of the objective lens, where the selected area electron diffraction (SAED) pattern is obtained. The SAED pattern is useful for examining the crystal properties in material areas as small as a few nanometres. For single crystals, discrete diffraction spots are observed while diffuse rings are obtained for amorphous materials.

In this study, TEM observations were carried out on a JEOL JEM-2100F with an emission voltage of 200 kV. Samples were prepared by dropping a dilute toluene solution of the nanoparticle (~0.05 mg/ml) onto 200 mesh carbon coated Cu grids. The TEM measurements were taken at City University of Hong Kong.

4.1.1.2 Scanning electron microscopy and energy dispersive X-ray spectroscopy

Distinct from TEM in which focused electrons are transmitted through the sample, scanning electron microscopy (SEM) works by scanning the electron beam over the sample surface and collecting the resulting signal. When the electron beam hits the sample surface, electrons interact with the sample within a bulb shaped volume. As shown in Figure 4.2, various types of radiations are generated and among all of these,

the low-energy secondary electrons emitted from the sample surface are the main source used for surface topography imaging. Lowering the accelerating voltage can efficiently detect the fine surface structures as the secondary electrons are generated only from the very surface of the samples.

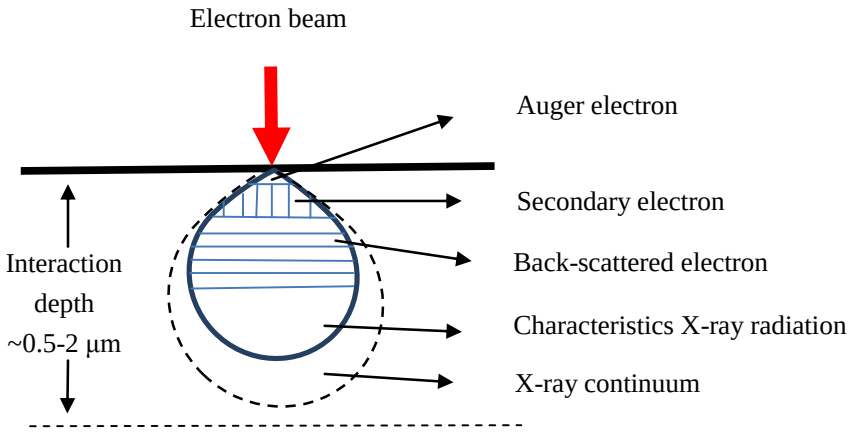

Figure 4.2 Schematic of electron beam interactions with the material surface.

In addition to the secondary electrons, the emitted characteristic X-ray radiation is taken into account for compositional analyses. As shown in Figure 4.3, an incident electron creates a vacancy by ejecting a core level atomic electron. The outer shell electron will fill this vacancy and emit a photon with an energy equivalent to the energy difference between the higher and lower level. Since atomic energy levels are quantised, the atom can be identified by measuring the energy of the X-ray. The emitted X-ray is defined as K_α X-ray since an electron falls from the *L* shell to the *K* shell. Similarly, the X-ray is defined as K_β X-ray when an electron falls from the *M* shell to the *K* shell.

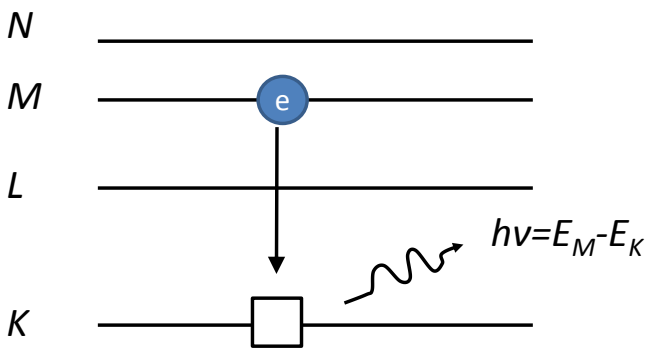

Figure 4.3 Schematic of characteristic X-ray generation from electron bombardment.

In this study, the morphology of thin films was studied using an FEI Quanta 200 scanning electron microscope with operating voltage of 5 kV. Thin film compositions were determined using an attached Oxford Instruments energy dispersive X-ray detector at an incident voltage of 20 kV. K_α X-ray emission lines for Cu, Zn, S and L_α for Sn were used for quantification.

4.1.2 Atomic force microscopy

Atomic force microscopy (AFM) is a type of scanning probe microscopy that uses the physical contact of a solid probe tip to scan the sample surface. In an AFM, a laser is focused onto a highly reflective cantilever and reflected onto the surface of a position-sensitive photodetector as shown in Figure 4.4. In tapping mode, the cantilever is oscillated at its resonant frequency and a prescribed amount of set point amplitude is used to represent sample contact. When the cantilever tip scans over the sample surface, the surface topography changes cause the amplitude of the reflected laser spot on the photodetector to deviate from its original amplitude. The piezoelectric scanner then responds by vertically deflecting the sample such that the

amplitude of the reflected laser spot is maintained at the set amplitude. This vertical deflection of the piezoelectric scanner is associated with a change in voltage. Therefore, the surface topography of the sample can be obtained by mapping out the corresponding deviations in this voltage.

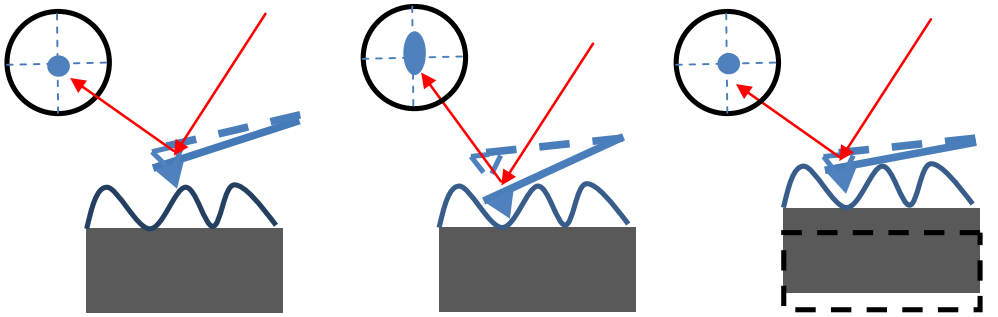

Step A: In contact with the surface, the cantilever oscillates at set point.

Step B: The scanner moves laterally, amplitude of tip changes.

Step C: The piezo moves vertically to maintain amplitude of

Figure 4.4 Schematic of tapping mode AFM working principle.

In this study, AFM images were taken using a Veeco Nanoscope multimode system. Thin films of CZTS nanoparticles were deposited by spin-coating onto the soda-lime glass (SLG) substrate at 4000 rpm for 30 s.

4.1.3 X-ray diffraction

X-rays are electromagnetic radiation with wavelength comparable to the interatomic spacing in a crystal lattice. Thus the diffraction spectrum can be obtained if X-rays are incident on the samples. As illustrated in Figure 4.5, $|AC| = |AB| \times \cos 2\theta = |AB| \times (1 - 2\sin^2 \theta)$ and the inter-planar spacing

$d = |AB| \times \sin\theta$.

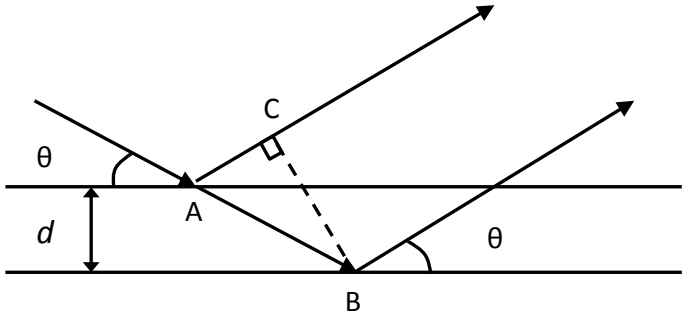

Figure 4.5 X-ray diffraction from atomic planes.

For constructive interference, the path difference between the incident beam and reflected beam should be an integer multiple of the incident X-ray wavelength:

$$|AB| - |AC| = n\lambda = 2d_{hkl}sin\theta \qquad (4\text{-}2)$$

Equation 4-2 is known as Bragg's law, where λ is the wavelength of the incident X-rays, d_{hkl} is the spacing between atomic planes *hkl* in the crystalline lattice, θ is the X-ray incident angle with respect to the diffracted atomic plane, n is the order of diffraction and equals to 1 in an X-ray diffraction (XRD) measurement.

For certain incident X-rays, different atomic planes with different inter-planar spacing fulfill Bragg's law at different diffraction angles. Each crystalline material as a result has a unique diffraction pattern. A crystalline material may then be identified by comparing its diffraction pattern with a standard diffraction database, such as the International Centre for Diffraction Data (ICDD), which maintains a database of PDF, including the *d*-spacing and relative densities of the diffraction peaks.

In addition, important crystal parameters can be also determined using the diffraction pattern. The inter-planar distance d is a function of the Miller indices of the planes and the lattice parameters. For example, CZTS has a tetragonal unit cell with the lengths of the cell edges $a = b \neq c$ and the angles between them $\alpha = \beta = \gamma = 90°$. The inter-planar spacing d_{hkl} between two consecutive (hkl) planes is given as:

$$\frac{1}{d_{hkl}} = \left(\frac{h}{a}\right)^2 + \left(\frac{k}{a}\right)^2 + \left(\frac{l}{c}\right)^2 \qquad (4\text{-}3)$$

Combining Equation 4-7 with Bragg's law, the lattice parameters can be determined from the diffraction pattern. Furthermore, the diffraction peak broadening can be used to estimate the nanocrystal domain size by employing Scherrer's equation:

$$D = \frac{K\lambda}{B\cos\theta} \qquad (4\text{-}4)$$

In Equation 4-4, D is the nanocrystal diameter, K is a constant related to crystal morphology and is typically 0.89 for spherical particles, B is the full width at half-maximum (FWHM) of the diffraction peak, and θ equals to half of the diffraction angle.

In this study, the crystal structure of the thin films was examined using a Siemens D-5000 diffractometer using a Cu K_α radiation source (λ=0.15406 nm) with step size of 0.02 °. During scanning mode, the instrument was operated at 40 kV and 40 mA.

4.1.4 Raman spectroscopy

Since the XRD technique is based on Bragg's law, crystalline materials are

indistinguished if they have similar atomic planar spacing. Raman spectroscopy is thus widely used as a complementary measurement to detect secondary phase in CZTS since it is based on the vibrational modes of a system [16, 77]. The theoretical basis of the Raman effect is given in Figure 4.6.

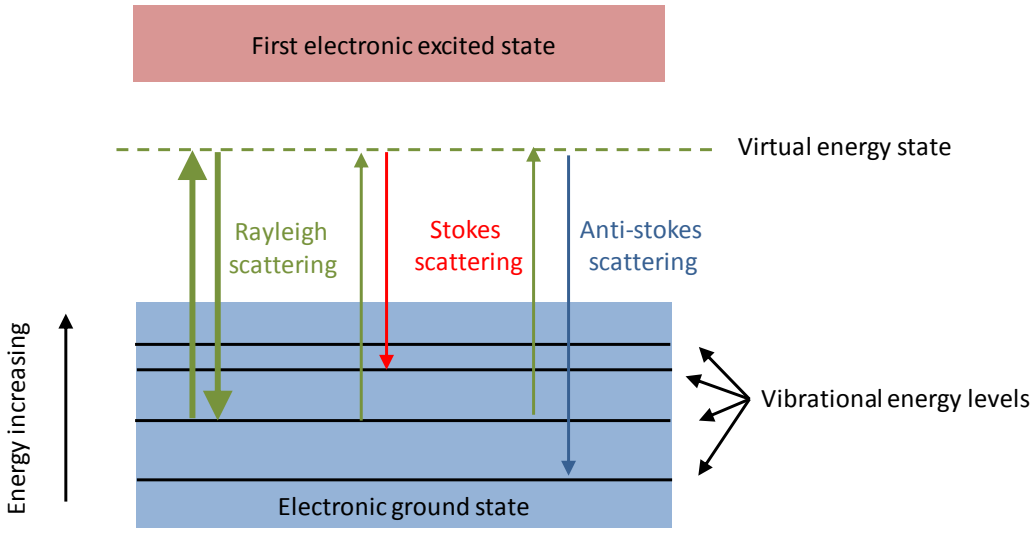

Figure 4.6 Schematic energy-level diagram involved in the Raman effect. The line thickness represents the signal strength from the different transitions.

Due to molecular vibrations, every single electronic state contains many sublevels known as vibrational energy levels as shown in Figure 4.6. Following absorption, the energy of incident photons is shifted due to molecular vibrations. The interactions can be divided into groups: elastic and inelastic. In the elastic one, the final vibrational state of the molecule is same level as the initial state. Thus the energy of the scattered photon is same as the incoming photons, and thus is known as Rayleigh scattering. In the inelastic one however, the final vibrational state is different from the initial one. On the one hand, when the final vibrational state of the molecule has

higher energy than the initial state, the scattered photon will lose energy and shift to longer wavelength. This inelastic scattering is known as Stokes scattering. On the other hand, if the final vibrational state is less energetic than the initial state, the inelastically scattered photon will gain energy and shift to shorter wavelength. Correspondingly, this scattering is designated as anti-Stokes scattering. The Stokes and anti-Stokes scattering are collectively called Raman scattering. To understand the energy shift of the scattered photons easily, a virtual energy level is introduced as shown in Figure 4.6. However, in contrast to the luminescence emitted when an excited electronic state returns to the ground electronic state, no real excitation and emission occurs in Raman scattering.

In Raman spectroscopy, the wavenumber (which is the reciprocal of the wavelength) is used to represent the energies of photons. The wavenumber difference between the incident photons and strokes scattered photons is defined as the Raman shift indicating the energy shift in the Raman scattering. The Raman shift is only related to the characteristic vibrational energy levels of the sample and independent to the incident photons. In this study, Raman measurements were performed with a Renishaw inVia microscopy using a 514 nm argon ion laser emitting at 2.5 mW and 10 % power. The acquisition time was 5 seconds per scan with the final spectrum created from the accumulation of 20 scans.

4.1.5 X-ray photoelectron spectroscopy

In X-ray photoelectron spectroscopy (XPS), an incident characteristic X-ray is absorbed and a secondary photoelectron is emitted with a kinetic energy E_K. The basic mechanism of XPS is illustrated in Figure 4.7.

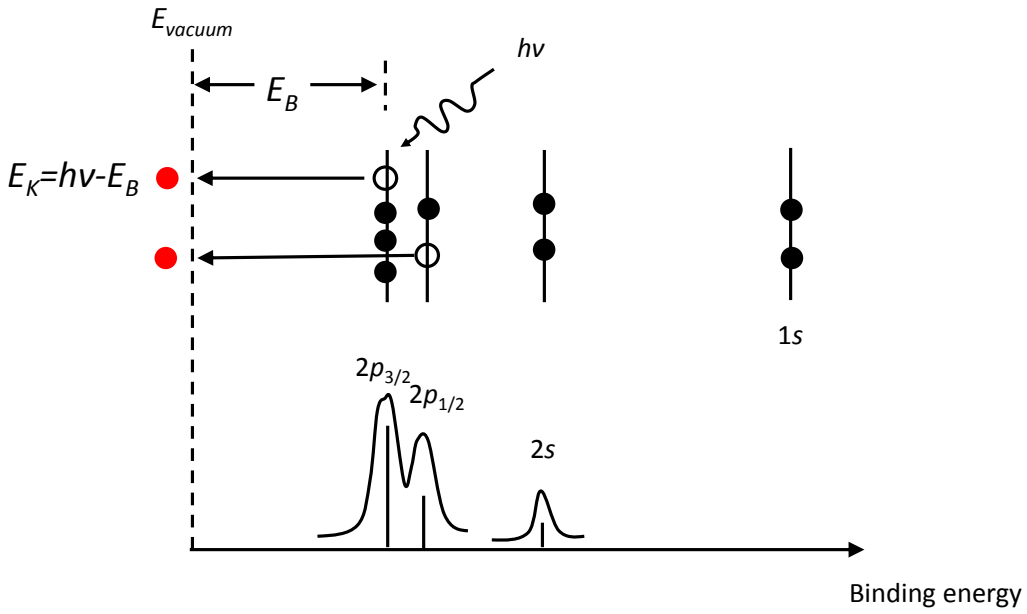

Figure 4.7 2p photoelectrons are emitted due to the absorption of the incident X-rays.

As shown in Figure 4.7, E_K is equal to the energy difference between the incident photon (hv) and the binding energy (E_B) needed to excite the electron from the atomic orbital level to the vacuum level. Since the atomic levels are quantised, the resulting binding energy spectra exhibit peaks that are characteristic of individual atoms. The escape depth of the secondary photoelectrons is limited to the surface region, and thus XPS technique is generally used to study surface chemistry of a sample.

Electrons ejected from atomic orbitals can be divided into two XPS observable states assigned by a quantum number *j*, which is defined by the angular momentum *l* such that $j = l \pm 1/2$. As shown in Figure 4.7, doublet peaks are observed corresponding to the two quantum states and appear with a relative intensity ratio of $2j_1+1:2j_2+1$. Thus for *p* electrons ($l = 1$), the doublet peaks are assigned as $p_{1/2}$ and $p_{3/2}$ with relative intensity 1:2, while for *d* electrons ($l=2$) the doublet peaks have relative intensity of 2:3. However, for the *s*-orbital ($l=0$), only a single peak can be observed. The separation energy between these doublet peaks is a characteristic that depends on an atom number, principal and angular momentum quantum.

The constituent elements of the thin films were confirmed using a Thermo Scientific K-alpha X-ray Photoelectron Spectrometer System with a monochromatic Al K_α X-ray source (1486.6 eV). A short sputter clean was performed before the scanning process to remove any contamination on the top surface. The XPS measurements were taken at National EPSRC XPS User's Service (NEXUS) at Newcastle University.

4.1.6 Secondary ion mass spectroscopy

Secondary ion mass spectroscopy (SIMS) can be used to study the compositional information from the surface to the bulk interior of the sample. Bombarding the sample with a focused primary ion beam causes secondary particles to be ejected from the sample due to atomic collisions as shown in Figure 4.8.

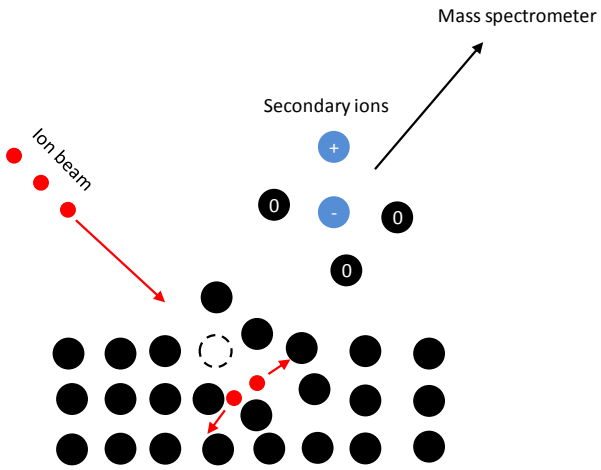

Figure 4.8 Principle of SIMS.

The ejected particles include monoatomic and polyatomic particles of the sample material. Typically, neutral particles are the most abundant of the ejected particles. However, only the positively or negatively charged particles which are defined as secondary ions can be detected by the mass spectrometer. Secondary ions with different mass to charge ratios will be separated and recorded to provide the basis for compositional analysis.

In this work, elemental depth profiles of the thin films were performed by monitoring the secondary ion count rate of selected elements as a function of sputtering time. A primary Ar^+ beam with an impact energy of 4 keV and beam current of 200 nA was used to sputter over a 500 μm × 500 μm rastered area. A gating area of 10 % was used to remove side wall effects.

4.1.7 Optical spectroscopy measurements

The effectiveness of a material at absorbing light is generally represented by the

absorption coefficient (α), which determines how far light of a certain wavelength can penetrate into a material before it is absorbed. For a material with a high absorption coefficient, light is efficiently absorbed and only penetrates a shallow region of the material. The absorption coefficient strongly depends on the material and wavelength of the incident light. For a given material, the absorption coefficient α at a particular wavelength can be determined by transmittance and reflectance measurements at the corresponding wavelength following Equation 4-5:

$$\alpha = \frac{1}{t} ln \left[\frac{(1-R)^2}{T}\right] \qquad (4\text{-}5)$$

where *t* is the thin film thickness, *R* is the reflectance and *T* is the transmittance.

Based on the obtained absorption coefficient, the optical energy bandgap E_g is related to α as:

$$\alpha h\nu = A(h\nu - E_g)^{1/m} \qquad (4\text{-}6)$$

where *A* is a constant, *h* is Planck's constant, $h\nu$ is the incident photon energy, *m* is a constant related to the energy band structure. For a direct bandgap semiconductor, the density of states function is given by:

$$g(\hbar\omega) = 0 \qquad \text{for } \hbar\omega < E_g \quad (4\text{-}7)$$

$$g(\hbar\omega) = \frac{1}{2\pi^2}\left(\frac{2\mu}{\hbar^2}\right)^{3/2}\left(\hbar\omega - E_g\right)^{1/2} \qquad \text{for } \hbar\omega \geq E_g \quad (4\text{-}8)$$

where $\hbar$ is reduced Plank constant and equals to $h/2\pi$, ω is angular frequency and equal to $2\pi\nu$, and μ is the effective electron-hole mass. By using Fermi's

golden rule:

$$\lambda_{if} = \frac{2\pi}{\hbar}\left|M_{if}\right|^2 \mathrm{g}(\hbar\omega) \qquad (4\text{-}9)$$

where λ_{if} is the quantum mechanical transition rate for exciting an electron from an initial to a final quantum state by absorption of a photon of angular frequency ω, and M_{if} is the matrix element for the transition. It is apparent that for photon energies greater than the bandgap the transition rate, and hence the absorption coefficient α will be proportional to $\left(\hbar\omega - E_g\right)^{1/2}$, *i.e.*:

$$\alpha(\hbar\omega) \propto \left(\hbar\omega - E_g\right)^{1/2} \qquad (4\text{-}10)$$

Consequently, m in Equation 4-6 is equal to 2 for a direct semiconductor and Equation 4-6 can be rewritten as:

$$(\alpha h\nu)^2 = A(h\nu - E_g) \qquad (4\text{-}11)$$

Using Equation 4-11, the energy bandgap can be estimated by extrapolating the linear portion of the curve $(\alpha h\nu)^2$ versus photon energy.

For these measurements, the optical properties of CZTS nanoparticles were studied using a Shimadzu SolidSpec 3700 spectrophotometer with scanning range from 360-1400 nm. All nanoparticle solutions were prepared with an absorbance of 0.020 $\pm$0.005 (after background correction) at 1600 nm in toluene.

4.2 Device characterisation

4.2.1 Current density-voltage measurement

Current density-voltage measurements (*J-V*) are necessary to provide the primary photovoltaic parameters such as V_{oc}, J_{sc} and *FF* that determine the device efficiency as described in section 2.3.2. *J-V* measurements were performed in a four-point probe configuration using a Keithley 2400 series sourcemeter. The current was recorded as the voltage was typically swept from -0.2 V to 0.6 V. Samples were illuminated with an Abet Technologies Sun 2000 solar simulator with an AM1.5 spectrum adjusted to 1000 W/m^2 using a pyronometer.

The shunt resistance R_{SH} and series resistance R_S can be also extracted from the *J-V* curves. To calculate the R_{SH}, the R_S of the solar cell is assumed negligible and Equation 2-46 can be simplified to:

$$J = J_o\left[\exp(\frac{qV}{AkT}) - 1\right] - J_{SC} + \frac{V}{R_{SH}} \qquad (4\text{-}12)$$

The derivative of 4-12 is:

$$\frac{dJ}{dV} = \frac{J_o \cdot q}{AkT}\exp\left(\frac{qV}{AkT}\right) + \frac{1}{R_{SH}} \qquad (4\text{-}13)$$

At the $J=J_{sc}$, $V = 0$. In addition, J_o is typically negligible and Equation 4-13 can then be simplified into:

$$\left.\frac{dV}{dJ}\right|_{J\approx J_{sc}} = R_{SH} \qquad (4\text{-}14)$$

Similarly, the series resistance can be found from:

$$\left.\frac{dV}{dJ}\right|_{V\approx V_{oc}} = R_S \qquad (4\text{-}15)$$

Therefore, estimates of R_{SH} and R_S can be extracted from the *J*-*V* curve by taking the inverse of the slope near $J=J_{sc}$ and $V=V_{oc}$, respectively.

4.2.2 Spectral response measurements

The spectral response of a solar cell is studied by quantum efficiency (QE) as a function of wavelength. The as-measured QE is referred to as the external quantum efficiency (EQE) where reflection and transmittance losses are not considered. The definition is given in Equation 4-16.

$$\mathrm{EQE} = \frac{number\ of\ collected\ electrons}{number\ of\ incident\ photons} = \frac{current\ density/charge\ of\ one\ electron}{power\ density\ of\ incident\ photons/energy\ of\ one\ photon} \qquad (4\text{-}16)$$

EQE measurements in this study were performed using a double grating monochromator (Bentham Instruments, M300) with scanning step of 5 nm.

EQE provides important device performance-related information such as optical loss mechanism, the position of maximum carrier collection and the energy bandgap. In addition, the maximum J_{sc} achieved by a solar cell can be also estimated from the EQE spectrum. To obtain this parameter, the AM1.5 spectrum is firstly divided into subgroups following the step size of EQE measurement (5 nm). Then the incident power in each group can be obtained by integrating the solar spectrum in the group wavelength range. The number of incident photons in each group can be calculated as follow:

$$\text{number of photons} = \frac{integrated\ solar\ spectrum(W \cdot m^{-2})}{h\frac{c}{\lambda}(J)} \qquad (4\text{-}17)$$

Substituting Equation 4-17 into Equation 4-16, J_{sc} obtained from each group is given as:

$$J_{subgroup}(A \cdot m^{-2}) = number\ of\ photons(\frac{W \cdot m^{-2}}{J}) \times EQE \times q(C) \qquad (4\text{-}18)$$

The maximum J_{sc} from a solar cell is then found by summing up all the subgroup values, i.e. $J_{sc} = \sum J_{subgroup}$.

4.2.3 Capacitance-voltage measurements

By considering the depletion region boundaries of a *p-n* junction as two plates, the depletion region is analogous to a parallel plate capacitor. The spacing between the two plates is thus equal to the depletion layer width. The capacitance C, is given by:

$$C = \frac{\varepsilon_o K_s A}{W} \qquad (4\text{-}19)$$

where W is the depletion layer width, A is the area of the junction, ε_o is the permittivity of free space and K_s is the semiconductor dielectric constant.

Substituting Equation 2-28 into Equation 4-19 gives:

$$\frac{1}{C^2} = \frac{2}{qN_A K_s \varepsilon_o A^2}(V_{bi} - V) \qquad (4\text{-}20)$$

It is clear from Equation 4-20 that a plot of $1/C^2$ versus voltage yields a straight line and the carrier density N_A, in the lightly doped side can be calculated from the slope while V_{bi} is obtained from the intercept $1/C^2$=0.

In this study, *C-V* measurements of solar cells were performed in the dark using an Agilent E4980A Precision LCR Meter operating at 100 kHz frequency and 100 mV step with reverse bias from 0 to -1 V.

Chapter 5

Fabrication of CZTS nanoparticle inks

CZTS nanoparticles have been fabricated by several research groups using the hot-injection method [74, 109, 111]. However, only the properties of CZTS nanoparticles fabricated at specific temperatures and times have been reported to date. There are few examples of systematic study of the structural and optical properties of the CZTS nanoparticles as a function of the reaction conditions. In this chapter, CZTS nanoparticles are fabricated using a hot-injection method while tuning the reaction temperature, cooling rate and time. The morphology, crystal structure, composition and optical properties of the nanoparticles are then detailed discussed. Based on these aforementioned investigations, a possible growth mechanism for the CZTS nanoparticles is proposed in the end.

5.1 Synthesis of CZTS nanoparticles

5.1.1 Reaction system

CZTS nanoparticles were fabricated using a hot-injection method involving the combination of metal salt precursors and sulphur dissolved in OLA [109]. As discussed in section 3.1.4, CZTS solar cells with the high efficiencies can only exist in a narrow Cu-poor and Zn-rich composition region. In this work, the precursor molar ratios are chosen to be Cu/(Zn + Sn) = 0.79 and Zn/Sn = 1.27, achieved by

using 1.34 mmol of $Cu(acac)_2$, 0.95 mmol of $Zn(acac)_2$, 0.75 mmol of $Sn(acac)_2Cl_2$ as the metal source for the nanoparticle fabrication. As shown in Figure 5.1, a three neck flask was used as the reaction vessel. The three necks were sealed by: (a) attaching a thermometer inlet to monitor the reaction temperature; (b) a septum for sulphur injection, and (c) a condenser attached to a standard Schlenk line. The core of the Schlenk line is the Schlenk manifold shown in Figure 5.2, which has two tubes. One tube is connected at one end to a source of nitrogen. It provides the dynamic inert gas supply to the reaction vessels. The excess gas exits past a check valve to a pressure release bubbler. The other Schlenk tube is connected to a vacuum pump and supplies dynamic vacuum (10^{-1} mbar) to the reaction vessel. By controlling a Teflon valve, vacuum or N_2 can be selected without placing the sample on a separate line.

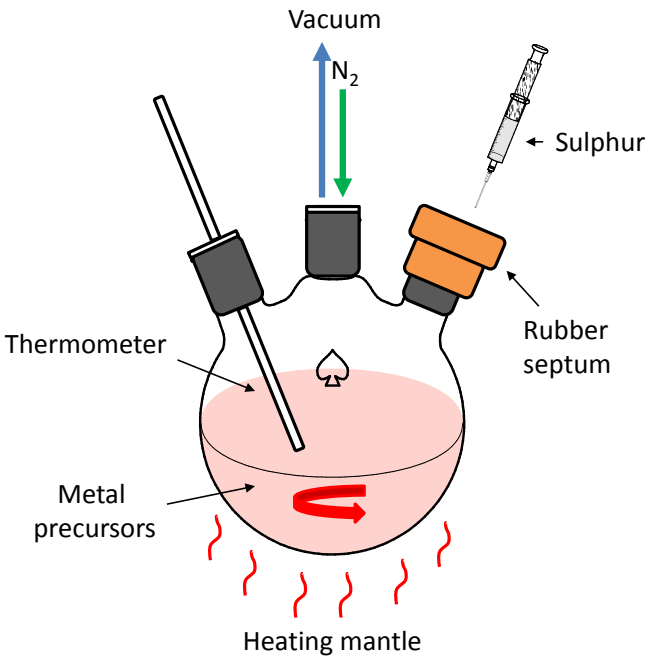

Figure 5.1 Schematic diagram of CZTS nanoparticle synthesis using hot-injection method.

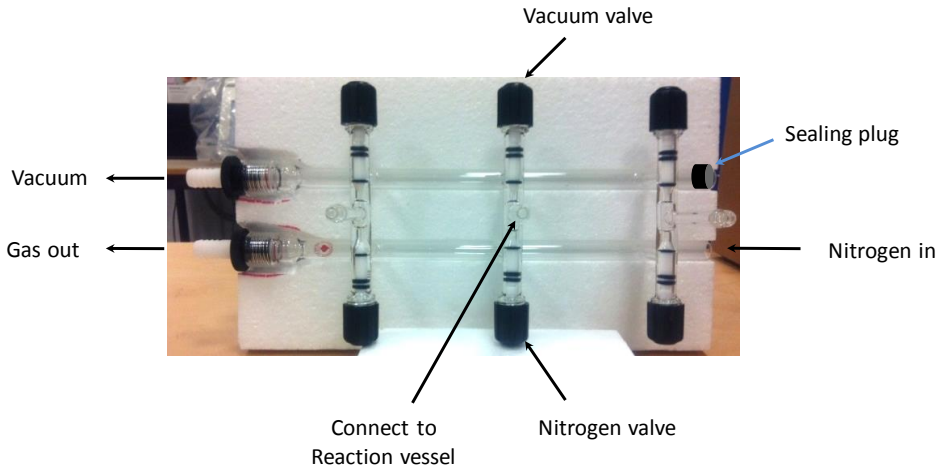

Figure 5.2 The connections of Schlenk manifold.

The reaction mixture was firstly put under vacuum and purged with nitrogen twice to remove residual water and oxygen dissolved in the solvents, which are detrimental for the reduction reaction to synthesis CZTS. After the degassing process, the temperature of the mixture is then increased to the reaction temperature after which 1M sulphur-OLA solution is then injected into the mixture. After injection, the reaction solution was held at the reaction temperature to allow the growth of the nanoparticles. The chemical reaction is given in Equation 5-1.

$$2Cu(acac)_2+Zn(acac)_2+Sn(acac)_2Cl_2+4S \xrightarrow[OLA]{\Delta} \text{CZTS nanoparticles + byproducts} \qquad (5\text{-}1)$$

For comparison purposes, a control sample was created by performing the reaction at 225 ℃ for 30 minutes, and then cooled down slowly (~5 ℃ /min) on the reaction mantle. For the rapidly cooled sample however, an ice-bath was used to quench the reaction system with a high cooling rate of (~ 20 ℃/min). Additionally, temperature-dependent experiments were performed by setting the reaction

temperature to 195, 210 and 240 ℃ for a fixed reaction time of 30 minutes, and time-dependent experiments were performed by setting the time to 15, 45 and 60 minutes at a fixed temperature of 225 ℃.

5.1.2 CZTS nanoparticle collection

After the reaction, 5 ml of toluene and 40 ml of isopropanol (IPA) were added into the reaction mixture and the nanoparticles were collected using two 50 ml tubes in a centrifuge. After centrifuging at 8450 rpm for 10 minutes, the supernatant containing unreacted precursor and by-products were discarded. The CZTS nanoparticles were then washed twice with toluene and IPA. Finally, before storing the nanocrystal ink in a glass vial, a size selection process was performed to remove large particles and agglomerates by centrifuging at 7000 rpm for 3 minutes. The schematic of typical CZTS nanoparticle ink synthesis process is shown in Figure 5.3.

The as-synthesised CZTS nanoparticle ink dispersed in toluene had a concentration of approximately 10 mg/ml. However, the ink needed to be concentrated to higher concentration to yield efficient deposition. Hexanethiol was selected as the solvent because of its ability to create a stable high concentration solution and wet the Mo-substrate well. In addition, because of its intermediate boiling point (~150-154 ℃), the residual hexanethiol in the nanoparticle thin film could easily be removed by mild heating in air. A CZTS nanoparticle ink was therefore dispersed into hexanethiol with the aid of sonication and then filtered through a 1 micron

syringe filter to remove large agglomerates. The filtrate was then sonicated for 10 minutes to yield the final concentration of ~ 100 mg/ml.

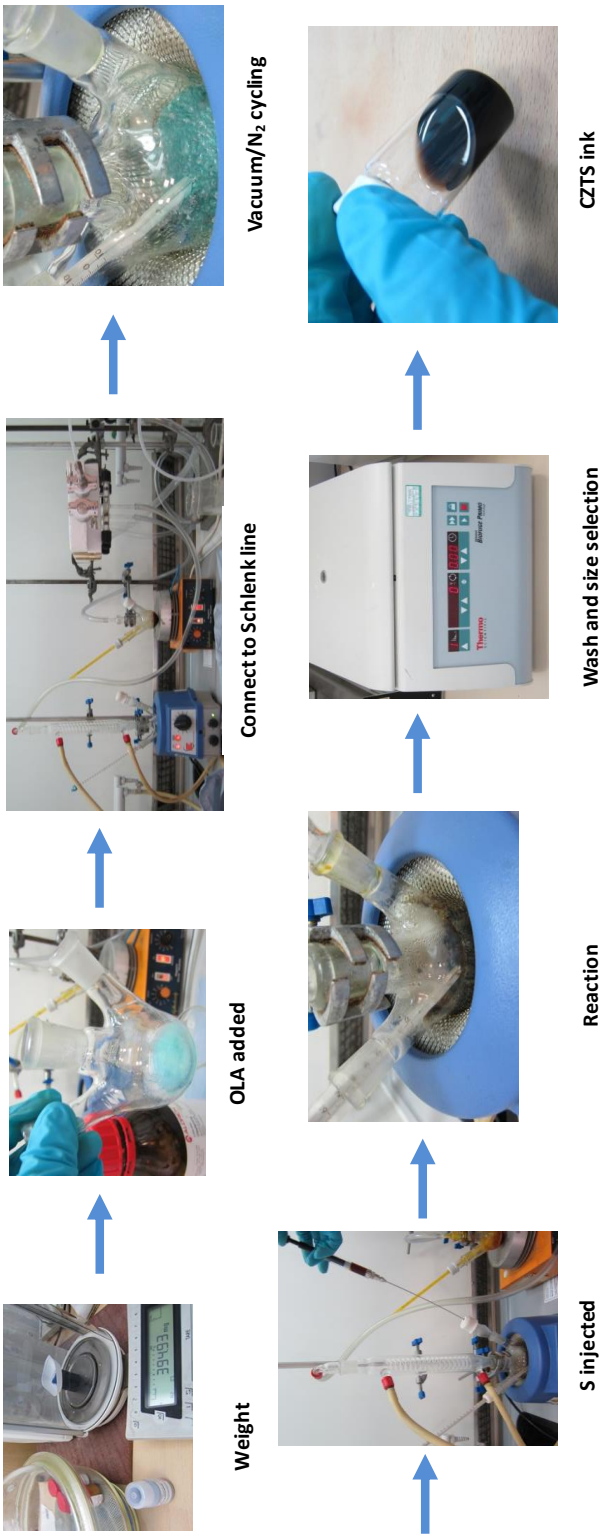

Figure 5.3 The schematic illustration of CZTS nanoparticle inks synthesis process.

5.2 Control sample properties

5.2.1 Morphology

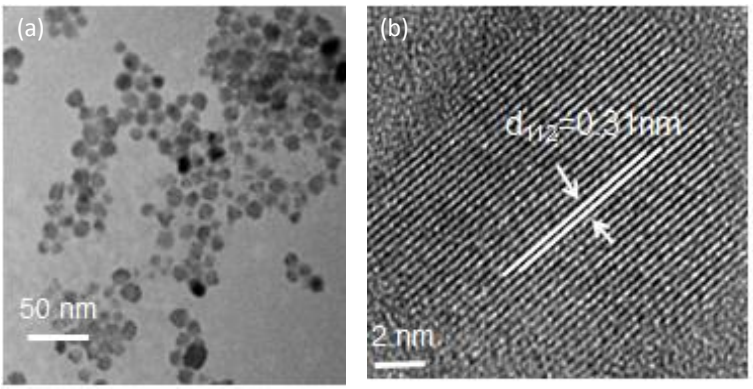

Figure 5.4 TEM images of CZTS nanoparticles at (a) low and (b) high magnification.

Figure 5.4 (a) shows a low-magnification TEM image of the control sample prepared at 225 ℃ for 30 minutes. It can be seen that the CZTS nanoparticles have an irregular spherical shape and are slightly polydispersed with most of the nanoparticles having diameters in the range 10-25 nm. A high magnification TEM image of a single CZTS nanoparticle is shown in Figure 5.4 (b), which shows good crystallinity of the nanoparticles. The inter-planar spacing is measured to be 0.31 nm, corresponding to the (112) planes in a kesterite structure.

5.2.2 Crystal structure

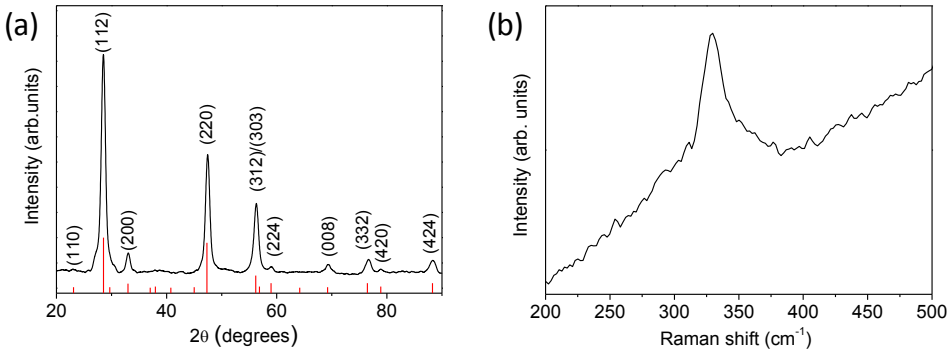

Figure 5.5 (a) XRD pattern of as-synthesised CZTS nanoparticles compared to the reference pattern (red lines) for kesterite CZTS (PDF 026-0575) and (b) Raman spectrum of CZTS nanoparticles.

The XRD pattern of a typical control sample is shown in Figure 5.5 (a). The peaks of the as-synthesised CZTS nanoparticles are indexed to tetragonal CZTS (PDF 026-0575). The major XRD diffraction peaks appear at ~ 28.5 °, 47.5 °, 56.3 ° and can be attributed to the (112), (220) and (312) planes of kesterite CZTS respectively. The lattice parameters calculated for the CZTS nanocrystals were 5.410 Å and 10.843 Å for lattice parameters *a* and *c* respectively. The lattice spacing of the (112) plane is calculated to be 0.31 nm which matches the lattice spacing obtained from high magnification TEM.

The kesterite crystal structure of the nanoparticles is further confirmed by Raman spectroscopy as shown in Figure 5.5 (b). The peak located at 329 cm^{-1} is close to the reported values of the characteristic CZTS peak (325-339 cm^{-1}) [40, 78, 107, 110, 115, 127-129]. This peak is somewhat asymmetrical however characteristic peaks

from $Cu_{2-x}S$ (475 cm^{-1}), Cu_2SnS_3 (298 cm^{-1}), Cu_3SnS_4 (318 cm^{-1}) and ZnS (355 cm^{-1}) were not observed [127]. The main band at 329 cm^{-1} is thought to be down-shifted from the reported characteristic peak of 338 cm^{-1} due to cation sublattice disorder in non-stoichiometric CZTS material [130].

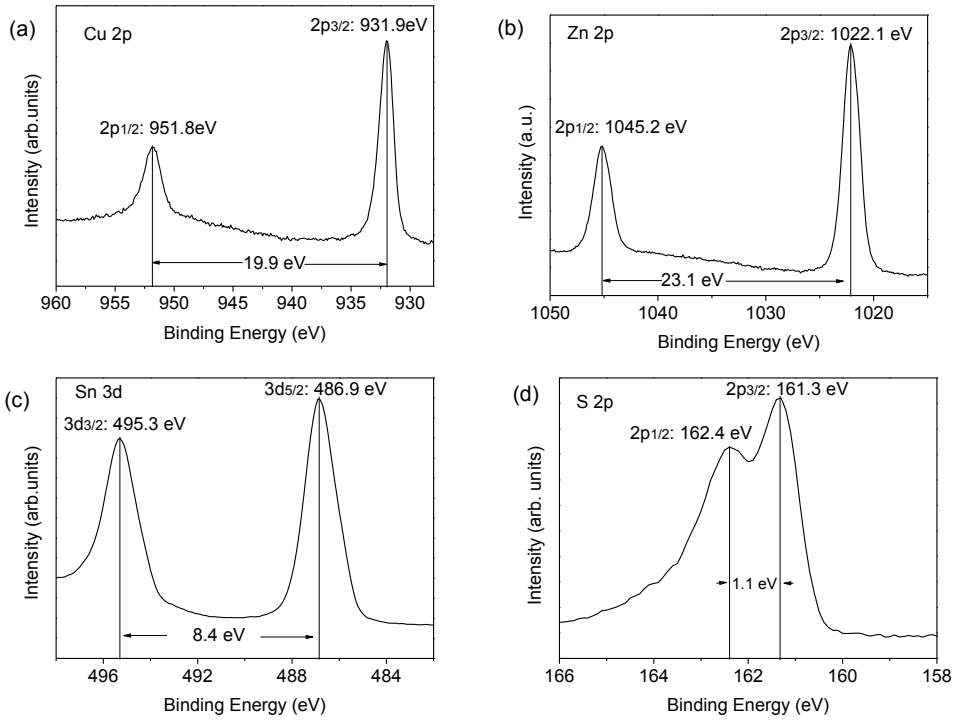

Figure 5.6 XPS spectra of Cu 2p, Zn 2p, Sn 3d and S 2p spectra of the CZTS nanoparticles.

XPS was further used to confirm that the chemical synthesis method resulted in the formation of Cu (I) valence states in the CZTS nanoparticles. As shown in Figure 5.6 (a), the copper spectrum shows two narrow peaks at 931.9 and 951.8 eV, with a peak splitting of 19.9 eV. No satellite features at 943 eV of Cu (II) indicates the sole presence of Cu (I). The zinc 2*p* peaks at 1022.1 and 1045.2 eV show a separation of 23.1 eV, consistent with the standard splitting of 23 eV for Zn (II). The tin 3*d* peaks

at 486.9 and 495.3 eV with a splitting of 8.4 eV indicate Sn (IV). The binding energies of S $2p_{1/2}$ and S $2p_{3/2}$ are 162.4 eV and 161.3 eV respectively, revealing the valance state of S (-II).

5.2.3 Composition

Elemental analysis of CZTS nanoparticles was performed using EDS. The average composition of an as-synthesised CZTS nanoparticle control sample was $Cu_{1.72\pm0.02}Zn_{1.13\pm0.02}Sn_{0.96\pm0.01}S_{4\pm0.06}$ with a Cu/(Sn+Zn) ratio of 0.83 and a Zn/Sn ratio of 1.18. A quasi-ternary composition diagram of the nanocrystals is presented in Figure 5.7. The average composition of the control sample is Cu-poor and Zinc-rich, falling in the region of high performance solar cells as summarised in Figure 3.7.

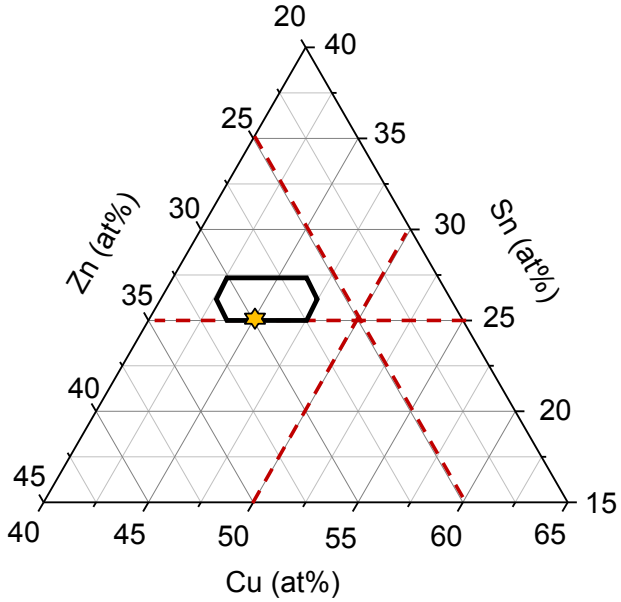

Figure 5.7 Quasi-ternary diagram based on the atomic percentage of Cu, Sn, and Zn in the nanoparticles. The golden star shows the composition of the control sample. The intersection of the dashed lines shows the stoichiometric point of CZTS. The highest efficiency CZTS-based PV devices lie inside the region indicated by the black hexagon.

5.2.4 Optical properties

Transmission T (%) and reflection R (%) spectroscopy of CZTS thin film was performed to study the optical properties of the CZTS thin films and the results are shown in Figure 5.8 (a). The optical absorption coefficient (α) was calculated using Equation 4-6 as discussed in section 4.1.7. The thickness of the control thin film was 1100 nm measured using DEKTAK XT profilometer.

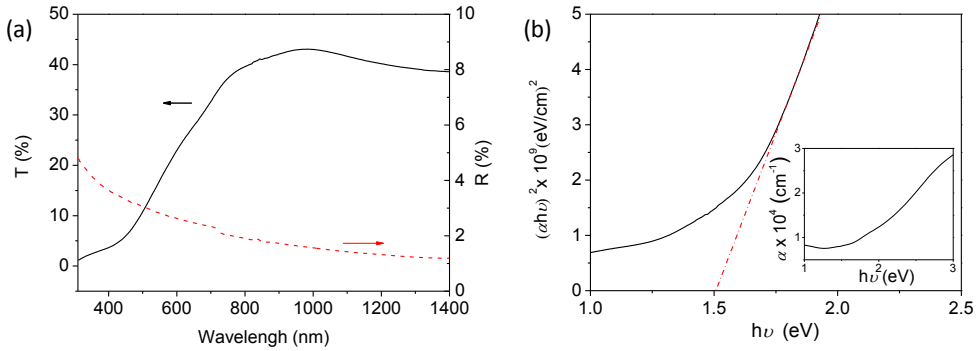

Figure 5.8 (a) Optical transmission *T* (%) and reflection *R* (%) curves of the control CZTS thin film. (b) Energy bandgap of the control CZTS thin film on a glass substrate. The inset shows the optical absorption spectra.

Following Equation 4-11, the energy bandgap of the CZTS nanoparticle was estimated to be 1.51 eV by the extrapolating the linear portion of the curve $(\alpha hv)^2$ versus energy as shown in Figure 5.8 (b). This is in good agreement with values reported in the literatures (1.3-1.6 eV) [74, 109, 111, 113]. The inset of Figure 5.8 (b) shows that the CZTS thin film has a high absorption coefficient (greater than 10^4 cm^{-1}) in the visible light region.

5.3 Effect of reaction temperature

Temperature-dependent experiments were performed by setting the reaction temperature to 195, 210, 225 and 240 ℃ for a fixed reaction time of 30 minutes.

5.3.1 Morphology

The morphologies and grain size distributions of CZTS nanoparticles prepared at different temperatures are shown in Figure 5.9. The nanoparticle sizes generally increase with the reaction temperature. The average grain sizes (determined from the

AFM images) of CZTS nanoparticles prepared at different temperatures are given in Figure 5.10. It can be seen that the average grain sizes of CZTS nanoparticles have a trend to increase from 14 nm for 195 ℃ to 20 nm for 240 ℃. At higher temperatures, the ions have a greater reactivity, which facilitates the growth of the nanoparticles.

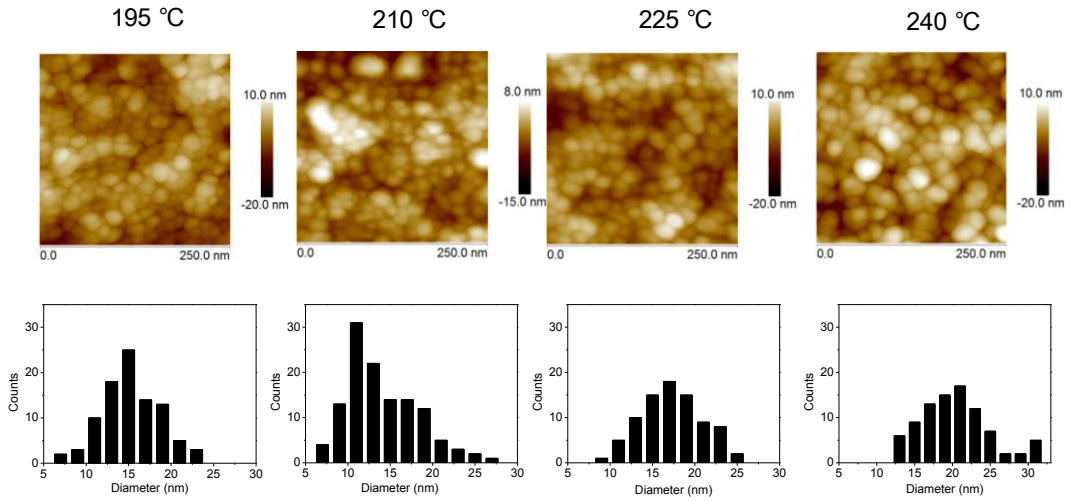

Figure 5.9 AFM images and corresponding size distribution histograms of CZTS nanoparticles prepared at different temperatures.

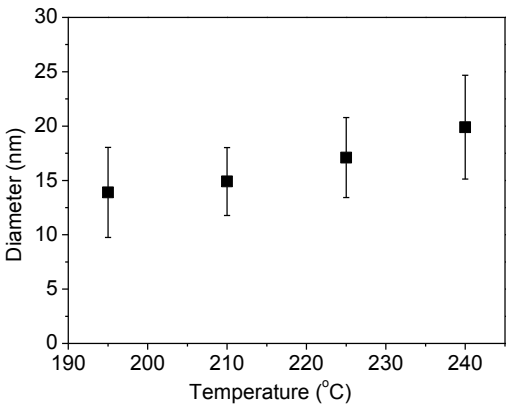

Figure 5.10 Average grain sizes of CZTS nanoparticles prepared at different temperatures.

5.3.2 Crystal structure

The XRD patterns of the CZTS nanocrystals prepared at different temperatures

(195-240 ℃) are shown in Figure 5.11 (a). The major diffraction peaks of all samples can be indexed to kesterite phase (PDF 026-0575). As shown in Table 5.1, the intensity of the (112) and (220) diffraction peaks increases gradually with increasing reaction temperature, indicating an improvement in crystallinity. The crystal domain size determined using the Scherrer equation (Equation 4-4) was found to increase from 4.4 nm at 195 ℃ to 11.5 nm at 240 ℃ as shown in Table 5.1. This is consistent with the AFM images which exhibited the same trend toward large grains with increasing temperature.

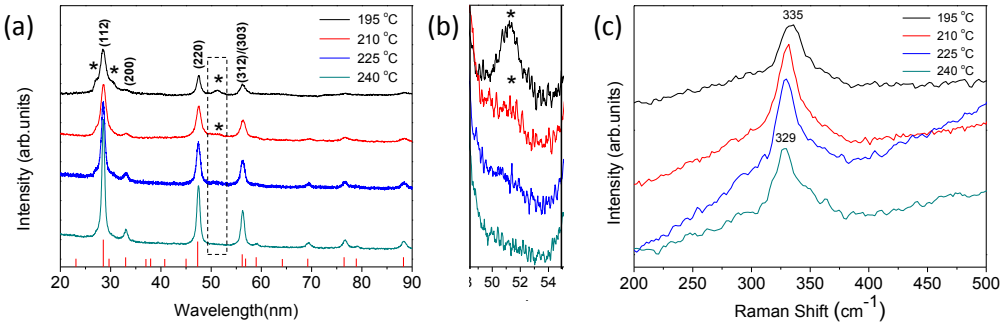

Figure 5.11 (a) XRD patterns, (b) enlarged picture of dashed rectangle in (a), and (c) Raman spectra of CZTS nanoparticles prepared at different temperatures for a fixed reaction time of 30 minutes. The red lines in (a) are the reference XRD pattern of CZTS (PDF 026-0575). Diffraction patterns and Raman spectra are off-set for better visibility. The Raman data were smoothed using a Savitzky-Golay method.

Table 5.1 XRD peak intensity, calculated crystal size, characteristic Raman peak, and energy bandgap of CZTS nanoparticles fabricated at different temperatures.

Sample	Peak intensity (a.u.)		Crystal size	Raman peak	Bandgap
	(112)	(220)	(nm)	(cm^{-1})	(eV)
195 ℃	1070	483	4.4	335	1.65
210 ℃	1346	785	6.3	332	1.61
225 ℃	1699	954	10.0	329	1.52
240 ℃	3127	1543	11.5	329	1.39

In addition to the main peaks, the CZTS nanoparticles prepared at 195 ℃ also exhibit three weak diffraction peaks marked by asterisks in Figure 5.11 (a). The sample prepared at 210 ℃ exhibits one of these three diffraction peaks around 51 °as shown in Figure 5.11 (b). These peaks can be indexed to either wurtzite CZTS [33, 82] or wurtzite ZnS [131, 132]. However, as shown in Figure 5.11 (c), there is only the characteristic peak of CZTS in the Raman data located around 330 cm^{-1} and this rules out the existence of ZnS. First-principle calculations suggest that wurtzite CZTS is unstable and prone to transit to the more stable kesterite CZTS phase [41]. However, some metastable wurtzite CZTS may not have enough time to finish this transition before the temperature cools down from the lowest reaction temperature to 70 ℃ when toluene was added to quench the reaction.

The change in the Raman spectra as a function of temperature is shown in Figure 5.11 (c) correlates with the XRD data. At 195 ℃, a broad peak characteristic of

CZTS was observed at 335 cm^{-1}. This is likely to be a result of a mixed kesterite and wurtzite atomic arrangement [78]. Increasing the temperature caused the peak to downshift as the kesterite component becomes more dominant. Similar to the XRD, no further change was observed ≥ 225 ℃ as the characteristic CZTS peak remained at 329 cm^{-1}. At 240 ℃ however, the characteristic Raman peak was observed to broaden relative to the lower temperatures. Peak fitting as shown in Figure 5.12 allows deconvolution of the data into peaks at 295 cm^{-1} and 359 cm^{-1} which matches with tetragonal Cu_2SnS_3 (CTS) at 297 and 352 cm^{-1} [127] . For nanoparticles fabricated at the highest temperature, secondary phase CTS is likely to be present.

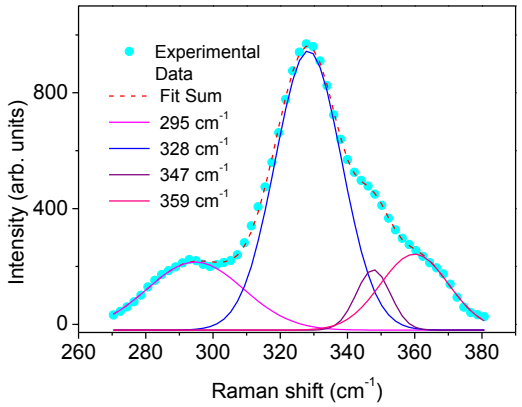

Figure 5.12 Deconvolution of experimental Raman data of the sample fabricated at 240 ℃ (30 minutes) using peaks of Gaussian distribution. The Raman spectra were smoothed using a Savitzky-Golay method before peak fitting. Peak at 328 cm^{-1} corresponds to the A_1 mode of CZTS, and the peak at 347 cm^{-1} may correspond to a shoulder for CZTS (350 cm^{-1}) [127].

5.3.3 Composition

Elemental analysis of the samples fabricated at different temperatures are summarised in Table 5.2. As the reaction temperature increases from 195 to 240 ℃,

the nanocrystals become richer in zinc and poorer in tin. In addition, nanoparticles fabricated at 195, 210, and 225 ℃ fall in the composition region suitable for high efficiency solar cells as shown in Figure 5.13.

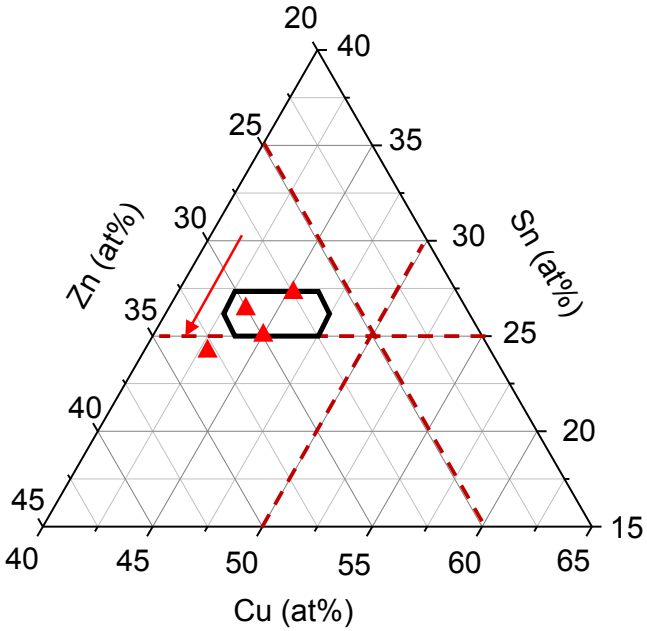

Figure 5.13 The red triangles show the compositions of nanoparticles fabricated at different temperatures and the red arrow points the direction of increasing temperature.

From a kinetics point of view, increasing the reaction temperature increases the reactivity of all cations. However, it appears that the relative increase in reactivity of Zn^{2+} is larger than that of Sn^{4+}, which results in more Zn being incorporated into the lattice making the nanoparticles richer in zinc and poorer in tin at higher temperature.

Table 5.2 Elemental ratios of CZTS nanocrystals fabricated at different temperatures according to EDS measurements.

Temperature (℃)	Cu/Zn/Sn/S	Cu/(Zn+Sn)	Zn/Sn
195	1.62/1.01/0.98/4	0.81	1.02
210	1.83/1.23/1.08/4	0.80	1.14
225	1.72/1.13/0.96/4	0.83	1.18
240	1.57/1.21/0.87/4	0.75	1.39

5.3.4 Optical properties

The absorption spectra of the CZTS nanoparticles fabricated at different temperatures are shown in Figure 5.14 (a). It can be seen that all the samples exhibited broad absorption in the visible region. The bandgaps of the CZTS nanoparticles were estimated by extrapolating the linear part of the function $(Ahv)^2$ versus energy (hv) (where A = absorbance, h = Planck's constant, and v = frequency) as shown in Figure 5.14 (b).

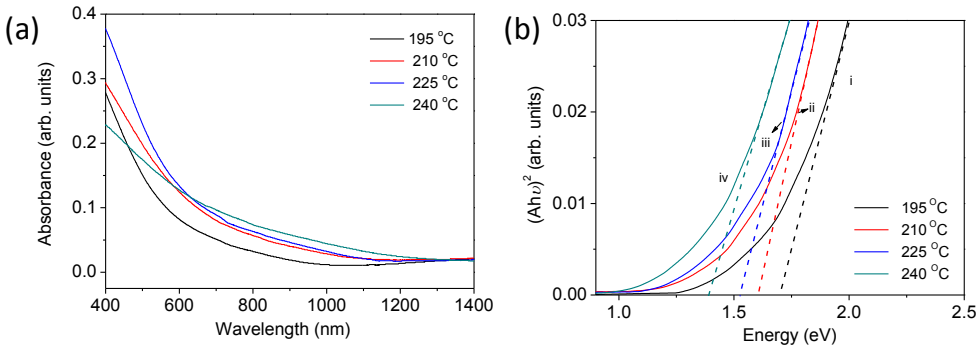

Figure 5.14 (a) Absorption spectra and (b) dependence of $(Ahv)^2$ on hv of CZTS nanoparticles prepared at different temperatures.

The obtained bandgaps are red-shifted as the reaction temperature was increased as

shown in Table 5.1. Although the average CZTS nanoparticle diameter was observed to increase as temperature increased (Figure 5.10), the change in the bandgap is not due to quantum confinement effects. The majority of the nanoparticles are much larger than the Bohr exciton radius of CZTS, estimated to be 3 nm depending on the values reported by Persson [59]. The presence of wurtzite CZTS at lower temperature accounts for the larger energy bandgap because the wurtzite-kesterite CZTS is calculated to have larger bandgap than kesterite CZTS [41]. For the sample fabricated at 240 ℃, the presence of ternary phase CTS (which has a relatively narrow energy bandgap of 1.35 eV) is likely to account for the reduction in the energy bandgap.

5.4 Effect of cooling rate

Cooling rate-dependent experiments were performed by setting the reaction temperature at 225 ℃ for 30 minutes. The rapidly cooled sample was quenched in an ice-bath with a high cooling rate of ~20 ℃/min while the slowly cooled sample was allowed to cool down naturally on a mantle with a low cooling rate of ~ 5 ℃/min. Both of the samples were cooled down to 70 ℃ where toluene was added to quench the reaction.

The crystal structure of the samples was then studied using XRD and the results are shown in Figure 5.15 (a). Compared with the slowly cooled sample, XRD peaks belonging to wurtzite CZTS are evident for the rapidly cooled sample. This rapid

quenching of the reaction leads to some metastable wurtzite CZTS in the sample. This observation indicates that the cooling mode plays an important role and will have a potential impact on achieving pure CZTS phase.

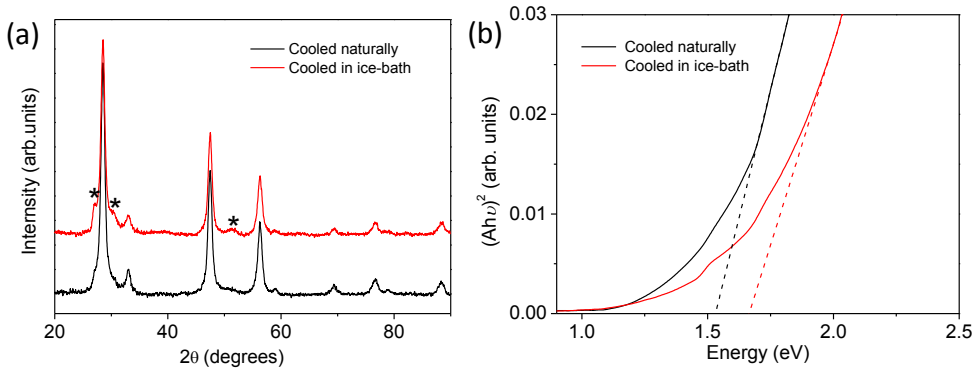

Figure 5.15 (a) XRD pattern and (b) dependence of $(Ahv)^2$ on hv of the CZTS nanoparticles prepared at 225 ℃ for 30 min. After the reaction, the reaction vessel was cooled down to 70 ℃ (i) naturally (black line) and (ii) in an ice-water bath (red line). The peaks belonging to wurtzite CZTS in (a) are indexed using asterisks.

Additionally, the bandgaps of the CZTS nanoparticles with different cooling rate were estimated by extrapolating the linear part of the function $(Ahv)^2$ versus energy (hv) (where A = absorbance, h = Planck's constant, and v = frequency) as shown in Figure 5.15 (b). Analysis of Figure 5.15 (b) reveals a higher energy bandgap for the rapidly cooled sample relative to a sample which cooled slowly. This phenomenon is also observed for the sample fabricated at 195 ℃ and further proves the presence of wurtzite CZTS accounts for the larger energy bandgap [41].

5.5 Effect of reaction time

Time-dependent experiments were performed by setting the reaction time to 15, 30,

45 and 60 minutes for a fixed reaction temperature of 225 ℃.

5.5.1 Morphology

The morphologies of CZTS nanoparticles prepared at different times are shown in Figure 5.16.

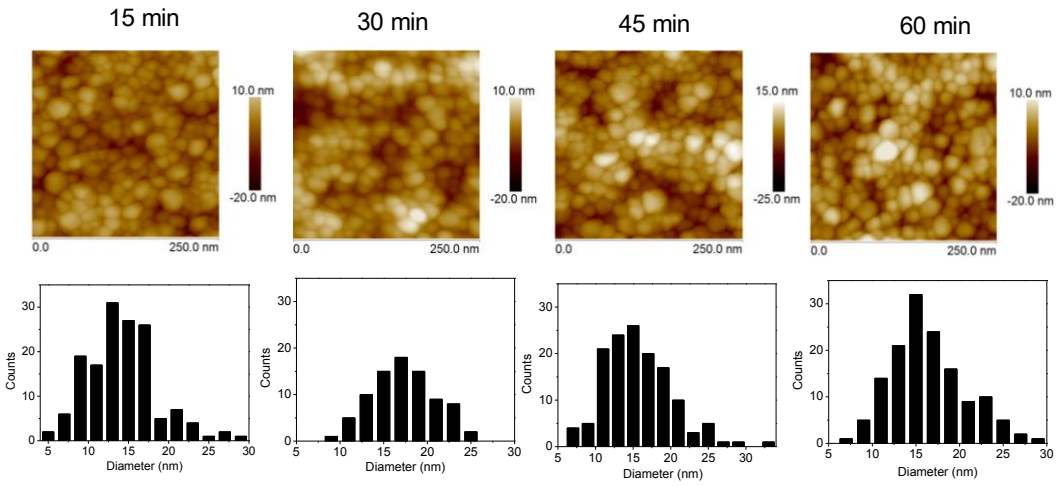

Figure 5.16 AFM images and corresponding size distribution histograms of CZTS nanoparticles prepared at different times.

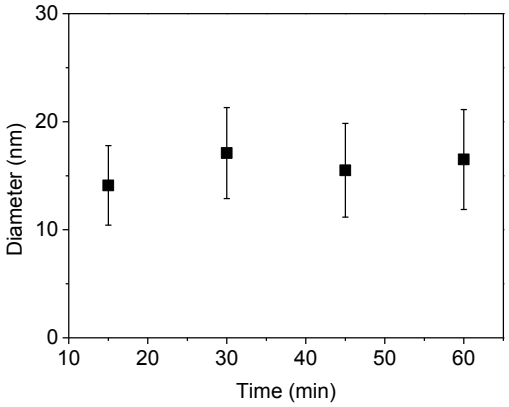

Figure 5.17 Average grain sizes of CZTS nanoparticles prepared at different time.

In contrast to the temperature dependent experiments, no obvious grain size

variations are observed when the reaction time changes. The average grain sizes of CZTS nanoparticles prepared at different times are given in Figure 5.17. It can be seen that the grain sizes of CZTS nanoparticles only fluctuate within a narrow region around 15 nm. However, the CZTS nanoparticles are more polydispersed as the standard deviation becomes larger which suggests the growth of the nanoparticles follows Ostwald ripening. The polydispersion of CZTS nanoparticles over time is due to the small nanoparticles dissolution and the redepositition on the surfaces of larger nanoparticles.

5.5.2 Crystal structure

The XRD patterns of the CZTS nanoparticles fabricated at different reaction times (15-60 minutes) are shown in Figure 5.18 (a). All diffraction patterns could be indexed to kesterite phase (PDF 026-0575). No weak peaks belonging to binary phases or wurtzite CZTS were detected. As calculated from the (112) diffraction peak, the crystal sizes only increased slightly from 8 nm to 11 nm when the reaction time was prolonged from 15 minutes to 60 minutes.

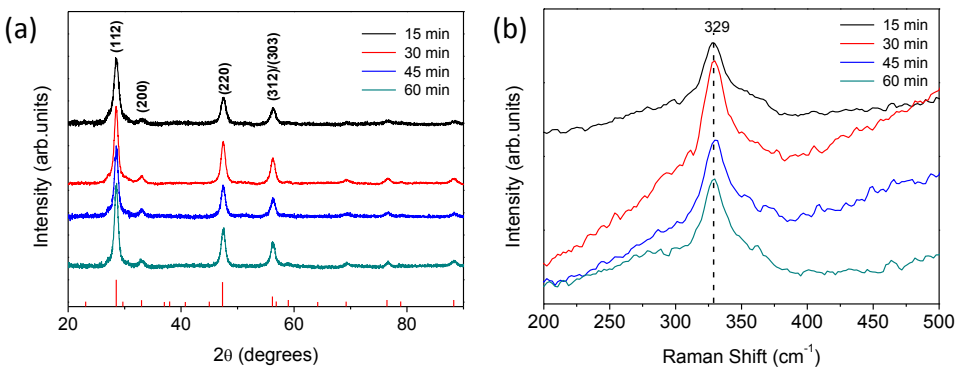

Figure 5.18 (a) X-ray diffraction patterns and (b) Raman spectra of CZTS nanocrystals prepared at a fixed temperature of 225 ℃ for different reaction times: (i) 15 min, (ii) 30 min, (iii) 45 min, (iv) 60 min. The red lines are the reference XRD pattern of CZTS (PDF 026-0575). Diffraction patterns and Raman spectra are off-set vertically for better visibility. The Raman spectra were smoothed using a Savitzky-Golay method.

Table 5.3 XRD peak intensity, calculated crystal size, characteristic Raman peak, and energy bandgap of CZTS nanoparticles fabricated at different times.

Sample	Peak intensity		Crystal size	Raman peak	Bandgap
	(112)	(220)	(nm)	(cm^{-1})	(eV)
15 min	1453	596	7.9	329	1.42
30 min	1699	954	10.0	329	1.52
45 min	1537	683	10.4	329	1.62
60 min	1830	855	11.0	329	1.84

Raman spectra of the samples shown in Figure 5.18 (b) were further used to confirm the structure of the CZTS nanoparticles. There is no shift of the characteristic peak of CZTS as the reaction time increased from 15 minutes to 60 minutes and only one clear peak exists at 329 cm^{-1}, which can be indexed to non-stoichiometry kesterite

CZTS material. No other characteristic peaks from secondary phases can be observed. The parameters extracted from XRD and Raman spectra are summarised in Table 5.3.

5.5.3 Composition

The average composition, Cu/(Zn+Sn) and Zn/Sn, of CZTS nanoparticles prepared at different times are summarised in Table 5.4.

Table 5.4 Elemental ratios of CZTS nanocrystals fabricated at different times according to EDS measurements.

time (min)	Cu/Zn/Sn/S	Cu/(Zn+Sn)	Zn/Sn
15	2.12/0.96/1.00/4	1.08	0.96
30	1.72/1.13/0.96/4	0.83	1.18
45	1.61/1.15/0.90/4	0.79	1.27
60	1.77/1.28/0.99/4	0.78	1.28

The composition position on the quasi-ternary diagram of the nanocrystals is also presented in Figure 5.19.

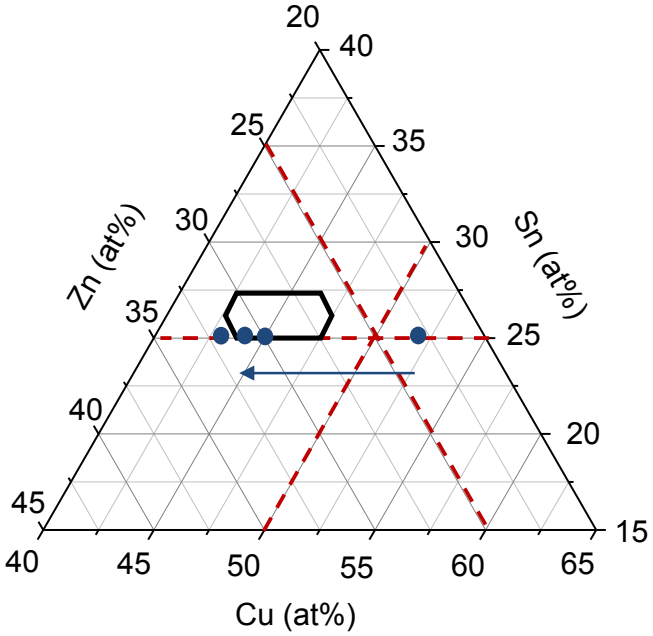

Figure 5.19 The blue dots show the compositions of samples prepared at different times and the blue arrow indicates the direction of increasing time.

It can be seen that nanoparticles fabricated for 30, 45 and 60 minutes fall within or just outside the composition region suitable for high efficiency solar cells. When the reaction time was 15 minutes, the composition of the nanoparticles lies in the Cu-rich and Zn-poor region. As the reaction time increases, the compositions of nanoparticles move into the Cu-poor and Zn-rich region with the composition of tin remaining constant at the stoichiometric ratio of 0.25.

The composition of the nanoparticles as a function of time can be explained by considering the hard-soft acid-base theory [133]. Cu^{+} is a soft Lewis acid and is therefore the most reactive metal precursor towards the soft Lewis base S^{2-}. Consequently, $Cu_{2-x}S$ is formed at the beginning of the reaction. As the reaction

evolves, Sn^{4+} and Zn^{2+} are gradually incorporated into the lattice of $Cu_{2-x}S$ replacing Cu ions. In this case, Sn^{4+} diffuses into the $Cu_{2-x}S$ nucleus to form Cu-Sn-S compounds at the beginning of the reaction followed by the replacement of Cu^{+} with Zn^{2+} to form CZTS. This model is supported by the constant composition of tin throughout the reaction progress. It is also likely that Cu^{+} will be preferentially replaced with Zn^{2+} rather than Sn^{4+} because its ionic radius (77 pm compared with 69 nm) is closer to that of Zn^{2+} (74 pm). This is supported by the increasing zinc composition as the reaction time increases (Table 5.4).

5.5.4 Optical properties

The influence of the reaction time on the optical properties of the CZTS nanoparticles is presented in Figure 5.20.

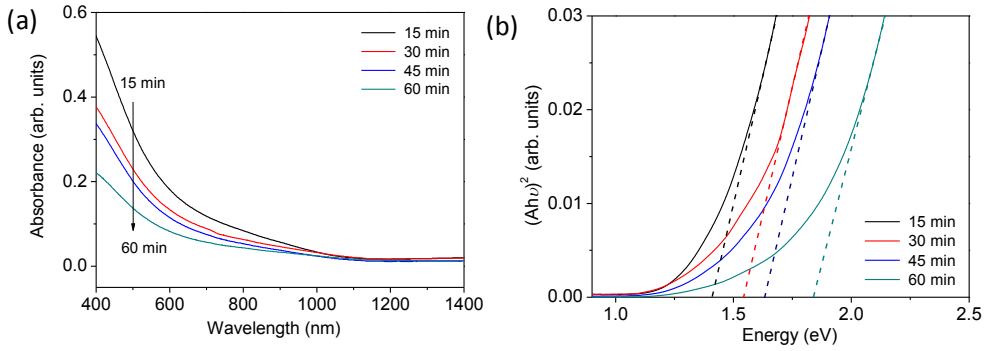

Figure 5.20 (a) Absorption spectra and (b) dependence of $(Ahv)^2$ on hv of the CZTS nanoparticles prepared at different times.

As in temperature-dependent experiments, all the samples exhibited broad absorption in the visible region as shown in Figure 5.20 (a). As the reaction time increased, the

absorption edge of CZTS nanoparticles gradually shifted towards shorter wavelengths. As shown in Figure 5.20 (b), the energy bandgaps were estimated to be 1.42, 1.52, 1.61, and 1.84 eV for CZTS nanoparticles prepared at 15, 30, 45, and 60 minutes respectively. The observed energy bandgap shift with reaction time is proposed to be stems from the doping level in the samples. It has been reported that CZTS is highly doped and that the degree of self-compensation is very high [15]. Under such circumstances, the excess electrons increase the conduction band minimum (CBM), and the excess holes reduce the valance band maximum (VBM) such that the bandgap is blue-shifted according to the Burstein-Moss effect [23, 134]. Under Cu-poor/Zn-rich conditions, V_{Cu}^{-} and Zn_{Cu}^{+} become the dominant defects in the system [48]. As the composition of nanocrystals become poorer in copper and richer in Zn, the excess holes provided by V_{Cu}^{-} reduce the VBM and the excess electrons provided by Zn_{Cu}^{+} increase the CBM. Therefore, the bandgap of CZTS nanocrystals may be expected to increase as the reaction evolves.

5.6 Nanoparticle growth mechanism

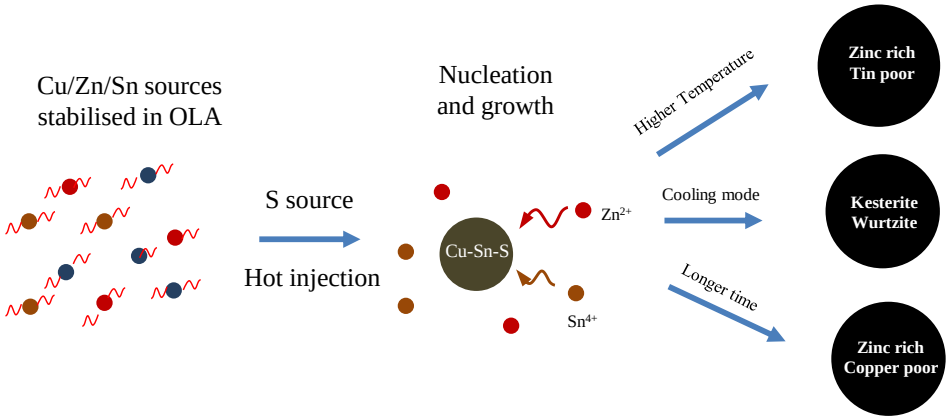

Figure 5.21 Schematic process of the controllable synthesis of CZTS nanoparticles.

Based on the above results, a possible reaction process is proposed to present the controlled fabrication of CZTS nanoparticles as shown in Figure 5.21. Firstly, metal salts are dissolved and stabilized in OLA by forming metal complexes. Following the hot injection of sulphur, nucleation immediately takes place between metal complexes and sulphur. At the beginning of the reaction, Sn^{4+} diffuses into the $Cu_{2-x}S$ nucleus to form Cu-Sn-S compounds followed by the competing doping of Zn^{2+} and Sn^{4+} to form CZTS. By increasing the reaction temperature, Zn-rich and Sn-poor nanoparticles are created because of the relative higher reactivity of Zn^{2+} than that of Sn^{4+} at higher temperature. However, when the reaction time increases, the composition of nanoparticles becomes Cu-poor and Zn-rich as Cu^{+} will be preferentially substituted by Zn^{2+} rather than Sn^{4+} because its ionic radius is closer to that of Zn^{2+}. In addition, the relatively short transition time of the fast cooling mode after the reaction leads to some metastable wurtzite CZTS in the samples.

5.7 Summary

In summary, CZTS nanoparticles have been synthesised using hot-injection of precursors. The reaction at 225 ℃ for 30 minutes with a slow cooling rate (~ 5 ℃/min) can synthesise pure kesterite CZTS nanoparticles with an energy bandgap of 1.5 eV. The influence of reaction temperature, cooling rate and reaction time on the structural, composition, and optical properties of CZTS nanoparticles has been systematically investigated. Wurtzite CZTS was formed at lower temperature or rapidly cooled sample whereas CTS was present at higher temperature. These factors were found to have a significant influence on the energy bandgap of the nanoparticles. Time-dependent experiments showed that the energy bandgap of as-synthesised CZTS was blue-shifted as the composition of the samples became poorer in copper and richer in zinc when the reaction time increased. Analysis of the experimental data indicates that it is crucial to optimise the reaction conditions to fabricate CZTS nanoparticles in a narrow region that is suitable for use in solar cell devices.

Chapter 6

Impact of nanoparticle inks on solar cell performance

CZTS nanoparticle inks offer an attractive route to the fabrication of earth-abundant CZTSSe thin film solar cells. In this chapter, the procedures to produce photovoltaic devices from CZTS nanoparticle inks are firstly described in section 6.1. As discussed in chapter 5, an experimental procedure has been developed to tune the properties of CZTS nanoparticle inks *via* the chemical reaction conditions. Although CZTS nanoparticle inks are the basis of the photovoltaic absorber layer, their impact on device performance has not yet been reported or investigated. The link between the properties of the nanoparticle inks and the completed solar cell performance is thus studied in section 6.2.

6.1 $Cu_2ZnSn(S,Se)_4$ thin film solar cells prepared from nanoparticle inks

In this section, the procedures to fabricate CZTSSe thin film solar cells from CZTS nanoparticle inks are discussed using the control sample described in section 5.2.

6.1.1 Precursor thin film deposited from CZTS nanoparticle inks

Following fabrication of a nanoparticle ink, CZTS precursor thin films were deposited using the spin-coating method. Approximately 30 μl of the concentrated

ink was applied onto a square (2.5 cm ×2.5 cm) Mo-coated glass substrate at a speed of 1200 rpm for 5 seconds. The samples were then dried on a hot plate at 150 ℃ for 30 seconds and then at 300 ℃ in air for 30 seconds (hereafter "soft-baking") to remove the residual solvents. The thickness of the deposited thin films could be accurately controlled and reproduced by repeated spin-coating and soft-baking procedures. A thickness of ~1 μm was set for efficient light absorption in all thin films.

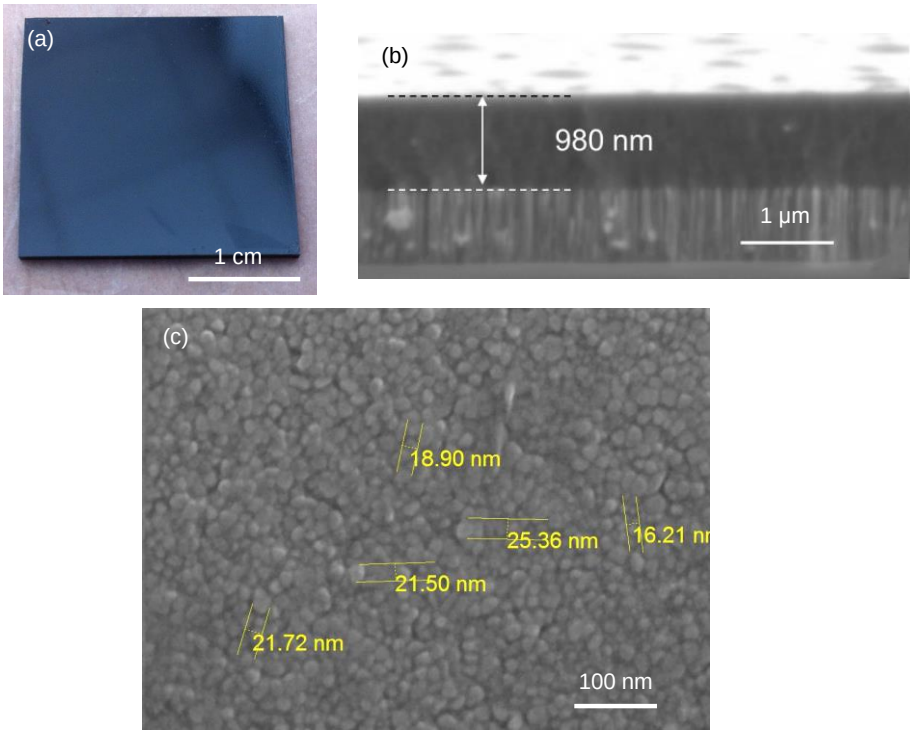

Figure 6.1 (a) Photo of as-deposited CZTS thin film on a 25×25 mm Mo-coated SLG. (b) Cross-sectional SEM image of the as-deposited CZTS film on Mo-coated SLG substrate. (c) Top view SEM image of the as-deposited CZTS nanoparticle thin film.

The as-deposited thin film appears smooth and uniform in a dark blue colour as shown in Figure 6.1 (a). Figure 6.1 (b) shows a representative cross-sectional SEM image of a CZTS nanoparticle thin film on Mo/SLG substrate following 10

spin-coating procedures. It can be seen that the film is uniform with a thickness of ~ 1 micron. The thickness of the thin film can be easily controlled by varying the number of coating repeats. Figure 6.1 (c) shows the top-view SEM image of the as-deposited CZTS nanoparticle thin film. It can be observed that the film is smooth and formed of densely packed, spherical nanoparticles with diameter around 20 nm.

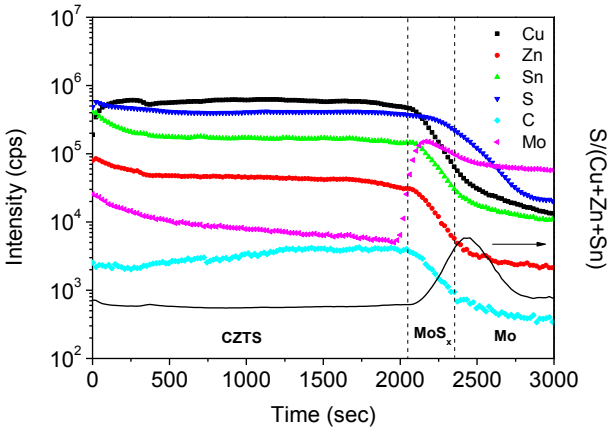

Figure 6.2 SIMS depth profiles of a CZTS thin film deposited on Mo-coated glass. The dashed vertical lines divide the profile into three composition zones. The solid line represents the S/metal count ratio.

The SIMS depth profiles of an as-deposited nanoparticle CZTS thin film are shown in Figure 6.2. Except at the very surface of the thin film where the oxygen increases the ion yield of positive ions, the constituent elements of CZTS exhibit uniform distribution throughout the as-deposited thin film. The profile S/metals ratio is also shown as the black solid line at the bottom of the graph which further demonstrates the uniformity of S and metals. The significant increase of Mo signal around 2100 seconds indicates the CZTS/Mo interface. Combining the curves of Mo and S/metal ratio, the spectra can be divided into three compositional zones marked by the

vertical dashed lines. A MoS_2 layer is formed during the soft-baking process between the CZTS layer and Mo substrate. Although most of the solvent was removed in the soft-baking process, the increase in C signal towards the interface with the substrate indicates some solvent molecular or molecular fragments are still present in the CZTS thin film with the soft-baking treatment gradually driving C towards the back of the film.

6.1.2 Selenisation into CZTSSe photovoltaic absorber layer

Although the aforementioned soft-baking procedure removed most of the ligand OLA on the nanoparticle surfaces, the as-deposited CZTS thin film exhibits poor optoelectronic properties due to the large number of grain boundaries existing within the nanoparticle thin film. For application in thin film photovoltaic cells, it is desirable for the light-absorbing film to have large grains which facilitate the transport of photo-generated carriers while minimising grain boundary recombination. To induce grain growth, the as-deposited CZTS thin films were heat treated in selenium atmosphere in a tube furnace. Specifically, the as-coated CZTS/Mo/glass films were placed face down inside a cylindrical graphite box with selenium pellets (~ 300 mg) placed on the two ends of the box. The graphite box was then loaded into a tube furnace to provide high temperature for the selenisation reaction as shown in Figure 6.3.

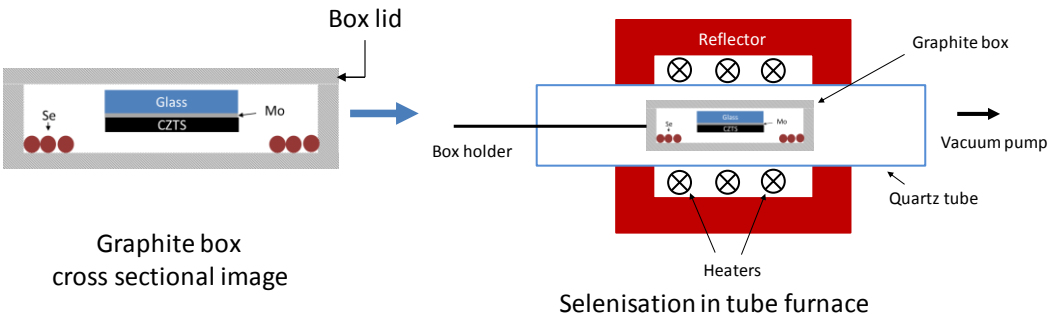

Figure 6.3 Schematic illustration of the selenisation process.

The furnace was evacuated (6.0×10^{-3} mbar) and backfilled with argon (~ 10 mbar) prior to increasing the temperature (~ 20 ℃/min) from room temperature to the selenisation temperature where it was held constant for a given time. The temperature profile of the selenisation process is given in Figure 6.4.

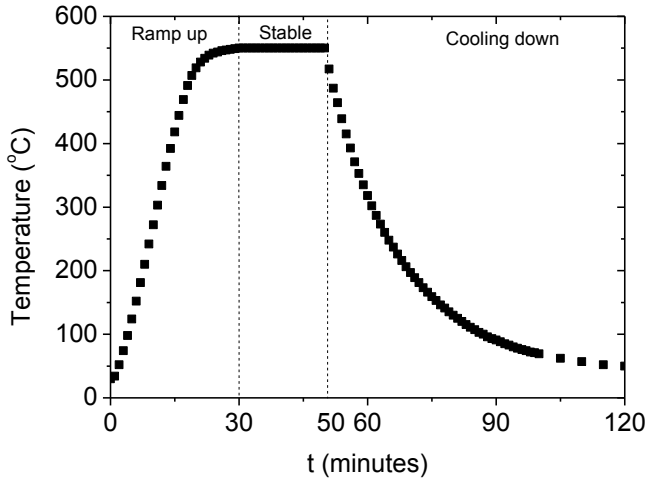

Figure 6.4 Temperature profile of the tube furnace.

As the graphite box was only partially closed, the selenium partial pressure inside the graphite box was not constant during the ramp up stage. Upon heating, the selenium evaporates and leaks through gaps to the whole quartz tube until equilibrium is

reached.

The equilibrium selenium vapour pressure can be determined using the model developed by Scragg [135]. The fraction (*F*) of selenium molecules that remains inside the box after equilibration is:

$$F = \frac{P_{Ar}+P_{Se_2}V_b/V_t}{P_{Ar}+P_{Se_2}} \qquad (6\text{-}1)$$

where P_{Se_2} is the pressure of Se_2 that can be obtained within the box if the box was kept sealed, P_{Ar} is the initial background pressure of Argon, V_b is the volume of the graphite box (3.0×10^{-5} m^3) and V_t is the total volume of the quartz tube (9.4×10^{-4} m^3).

Then the partial pressure of selenium P_{e,Se_2} within the graphite box after pressure equilibration can be given as:

$$P_{e,Se_2} = P_{Se_2} \times F \qquad (6\text{-}2)$$

Since P_{Ar}(10 mbar) is far lower than P_{Se_2}($>$ 4.0 bar when 300 mg of selenium was loaded), Equation 6-1 can be simplified and the partial pressure of Se_2 after equilibrium can be given by:

$$P_{e,Se_2} = P_{Se_2}\frac{V_b}{V_t} = n_{Se_2}\frac{RT}{V_t} \qquad (6\text{-}3)$$

where n_{Se_2} is the total number moles of selenium vapour, *R* is the ideal gas constant and *T* is the absolute temperature. In such conditions the pressure of selenium within the whole quartz tube after equilibration including the graphite box can be

determined from the initial amount of selenium loaded and the selenisation temperature. After the selenization process, the tube furnace was cooled down using a fan to the temperature below 300 ℃ in 10 minutes and to 50 ℃ in another 60 minutes as shown in Figure 6.4.

Compared with the dark blue as-deposited thin film, the selenised sampled plays a homogeneous grey colour as shown in Figure 6.5 (a).

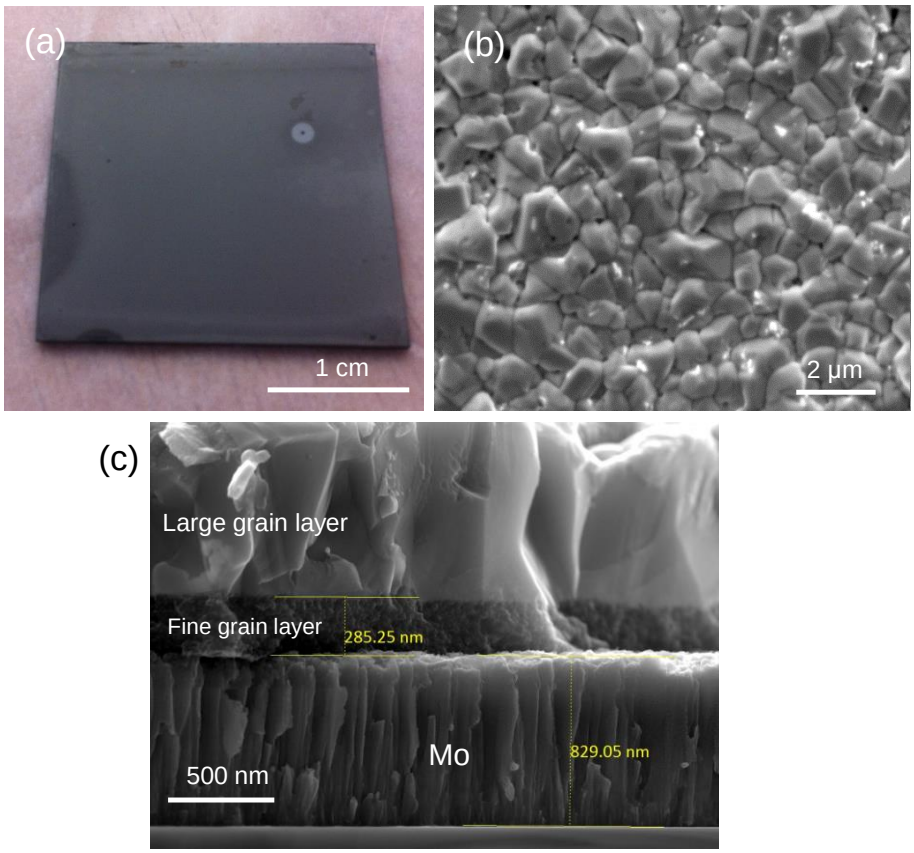

Figure 6.5 (a) Photo of selenised film on a 25×25 mm Mo-coated SLG. (b) Top-view and (c) cross-sectional SEM image of the selenised film. The thin films were selenised at 500 ℃ and selenium vapor pressure of 140 mbar for 20 minutes

From Figure 6.5 (b), it can be seen that the selenised thin film is composed of densely packed micrometre-sized grains, and with no obvious void or crack observed

on the surface. The cross-sectional SEM image (Figure 6.5 (c)) reveals a three-layer structure. The top CZTSSe layer is composed of a large grain upper layer (~ 1 μm thick) and a residual fine grain sublayer (~ 0.3 μm thick). The bottom layer is typical of Mo with a columnar grain structure. Under the selenium-rich thermal treatment conditions, a thin layer of $Mo(S,Se)_2$ forms on top of Mo layer. Although this is not easily seen in Figure 6.5 (c), it is further described next and in chapter 7. The morphology change of Mo layer during selenisation process is apparent from top view images. AFM top view images of a plain Mo substrate both before and after selenisation are shown in Figure 6.6. The Mo grains are in fusiform shape before selenisation. After selenisation however, the substrate grains change significantly into round nanoparticles, which reveals the morphology change of the Mo substrate during the selenisation process.

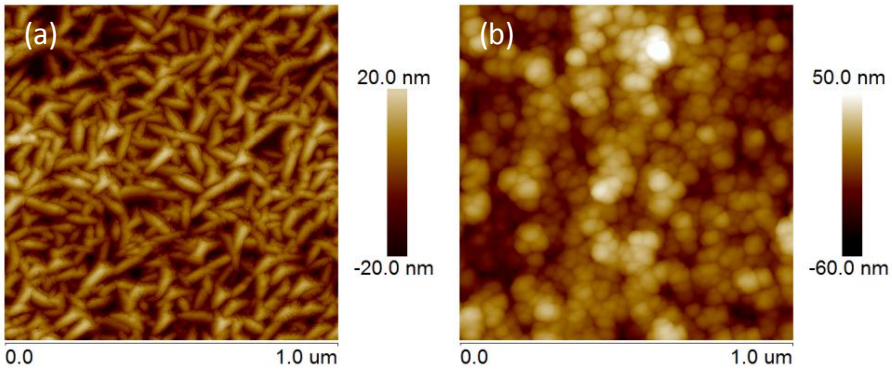

Figure 6.6 Top views of the plain Mo substrate (a) before and (b) after selenisation.

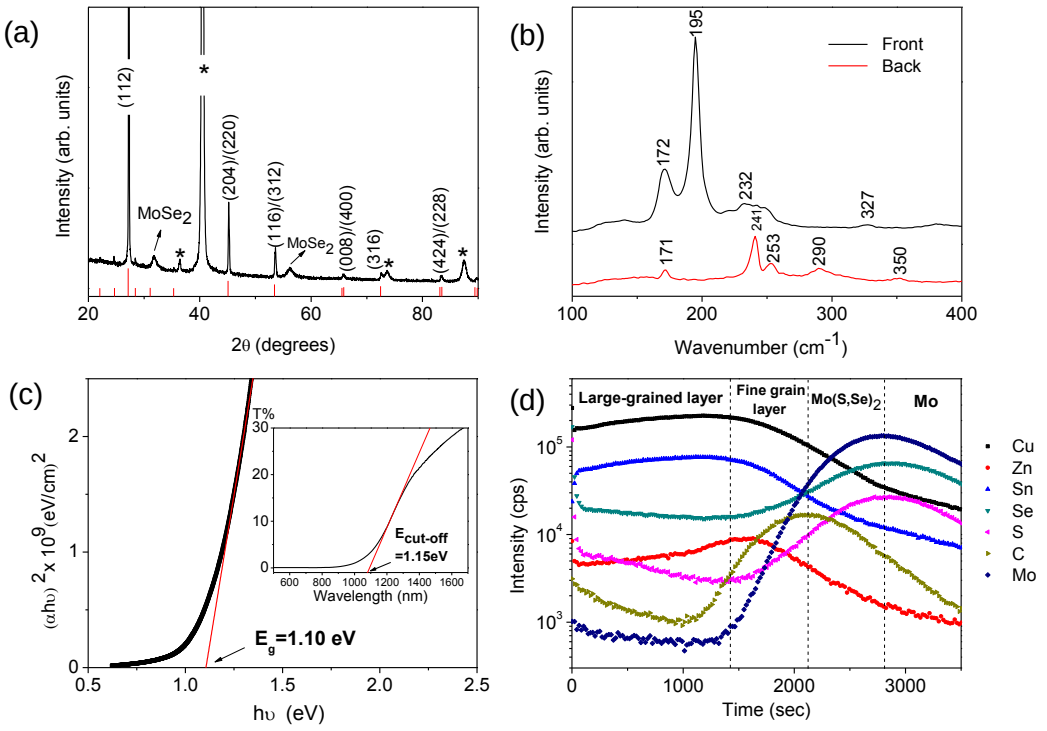

Figure 6.7 (a) XRD pattern of a selenised nanoparticle thin film compared to the reference pattern for pure CZTSe (PDF 052-0868). Peaks indexed to Mo are marked by * and $MoSe_2$ are also included. (b) Raman spectra of the thin film front surface and the remaining substrate after mechanically removing the absorber. Spectra are offset vertically for clarity. (c) E_g values of a CZTSe thin film estimated by plotting $(\alpha hv)^2$ vs hv from data obtained by transmission spectroscopy (inset). (d) SIMS depth profiles of the CZTSSe film. The dashed vertical lines divide the profiles into four composition zones.

The crystal structure of the thin film after selenisation was firstly studied by XRD. As shown in Figure 6.7 (a), the selenisation process causes a sharpening of the diffraction peaks compared with Figure 5.5 (a). All the peaks can be assigned to pure CZTSe (PDF 052-0868). However, a slight shift to higher angles is observed due to the residual sulphur present in the lattice. As shown in Table 6.1, about 10 % sulphur is left in the thin film after selenisation. The composition of the thin film is zinc rich

and copper poor. However, a zinc loss is observed during the selenisation process with a Cu/(Zn+Sn) ratio of 0.79 increasing to 0.90 and a Zn/Sn ratio of 1.15 decreasing to 1.07.

Table 6.1 The composition of as-deposited and selenised CZTS nanoparticle thin films. To avoid possible signal from the substrate Mo, these data were obtained from thin film selenised on bare SLG.

	Cu (at%)	Zn (at%)	Sn (at %)	S (at)%	Se (at)%	Cu/(Zn+Sn)	Zn/Sn	Se/(S+Se)
Before selenisation	23.95	16.21	14.14	45.70	0	0.79	1.15	0
After selenisation	22.18	12.70	11.87	5.24	48.01	0.90	1.07	0.90

Raman spectroscopy was also performed on the selenised films as shown in Figure 6.7 (b). The two sharp peaks at 172 and 195 cm^{-1}, and weak peaks at 233 and 244 cm^{-1} correspond to the literature values of CZTSe [79]. The peak at 248 cm^{-1} is possibly due to trace amount of ZnSe [136]. However, this contribution is difficult to determine with accuracy as it appears as a shoulder peak at the high frequency side of the 233 cm^{-1} peak. In addition, the wide peak at 327 cm^{-1} can be attributed to the residual CZTS [80]. In order to analyse the region close to the absorber/Mo interface, the measurement was repeated on the substrate after mechanically removing part of the absorber. As shown in Figure 6.7 (b), the spectrum from the substrate shows clear peaks at 241 and 253 cm^{-1} which can be identified as the main mode of $MoSe_2$ and ZnSe, respectively. In addition, weaker peaks at 171, 290 and 350 cm^{-1} can all be

indexed to $MoSe_2$ [79].

The energy bandgap of the CZTSSe thin film was estimated to be 1.10 eV by extrapolating the linear portion of a plot of $(\alpha h\upsilon)^2$ versus $h\upsilon$ as shown in Figure 6.7 (c). As the bandgap for pure CZTSe is reported to be 1.0 eV, this also indicates that some residual sulphur exists in the selenised film, which is consistent with the XRD and compositional analysis.

The elemental distribution in the selenised film was studied using SIMS and is shown in Figure 6.7 (d). Combined with the cross-sectional SEM image of Figure 6.5 (c), the SIMS spectra can be divided into the four sections mentioned previously with different compositions. The large-grain layer is composed of high purity CZTSSe with low carbon content. The residual fine-grain layer is rich in carbon, especially close to the substrate interface confirming the hypothesis that carbon is driven towards the back of absorber layer upon thermal annealing. The source of carbon stems from the long hydrocarbons chains of the capping ligand OLA used in the nanoparticle synthesis [137] since no fine-grain layer presents in the CZTSSe thin film when the absorber is prepared from aqueous CZTS nanoparticle inks [114]. It was speculated the high carbon content contributes the electrically conductivity of the fine-grain layer and these fine-grain layers are observed in the best performing CZTSSe devices made from nanoparticle inks [11, 12, 16]. However, the fine-grained nature of this layer may introduce high series resistance and reduce the fill factor of the solar cells [138].

Below the fine-grain layer, a $Mo(S,Se)_2$ layer is formed above the Mo substrate because high levels of S and Se signals are found between the CZTSSe film and Mo substrate according to the SIMS spectra. Even in selenium-rich conditions, some residual sulphur is still present in the lattice. This agrees with the Raman spectra shown in Figure 6.7 (b) where a slight Raman shift is observed compared with the reported position of pure $MoSe_2$ [79].

6.1.3 CZTSSe solar cell fabrication

The resulting CZTSSe thin films were embedded into solar cell devices with the configuration: Mo/CZTSSe/CdS/i-ZnO/ITO/Ni-Al. The CdS buffer layer was deposited using the chemical bath deposition. In this process, deionized water was first poured into a double-walled beaker connects to a circulating water bath. After the temperature inside the beaker stabilized at 70 ℃, $CdSO_4$ (2 mM) and ammonia (1.5 M) were added successively with continuously magnetic stirring to form a solution. The CZTSSe films were then soaked in the solution for 2 minutes before thiourea (12 mM) was mixed into the solution. This causes a CdS layer to form on the sample surface. After the reaction, the samples were removed from the bath, rinsed with deionised water, dried under a nitrogen stream and then annealed at 200 ℃ for 10 minutes in air [80, 139]. The transparent conductivity oxide layer (~ 35 Ω/□) was deposited by magnetron sputtering ~ 60 nm i-ZnO and ~200 nm ITO., The front contact grid was then deposited by electron beam evaporation of Ni (~50 nm) and Al (~1 μm) through a shadow mask. Finally, each substrate was defined by

mechanical scribing into nine 0.16 cm^2 devices.

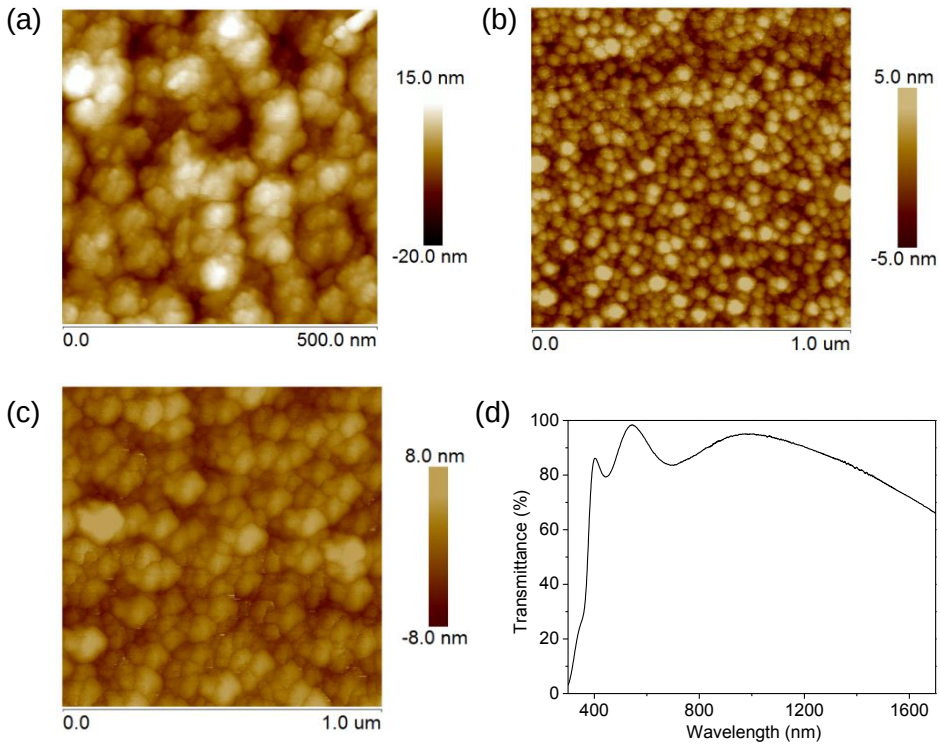

Figure 6.8 Top views of the different layers deposited in the device: (a) CdS, (b) i-ZnO, and (c) ITO. (d) Optical transmission curve of the i-ZnO/ITO layer.

The morphologies of the different layers deposited subsequently to the absorber layer are presented in Figure 6.8. The CdS layer is composed of irregular shaped particles in the absence of large agglomerates and pinholes. The i-ZnO layer is composed of small particles, whereas the ITO layer is formed by densely packed grains. As shown in Figure 6.8 (d), the i-ZnO/ITO combined layer yields good transparency as up to 95 % of the light is transmitted through the film in the visible region.

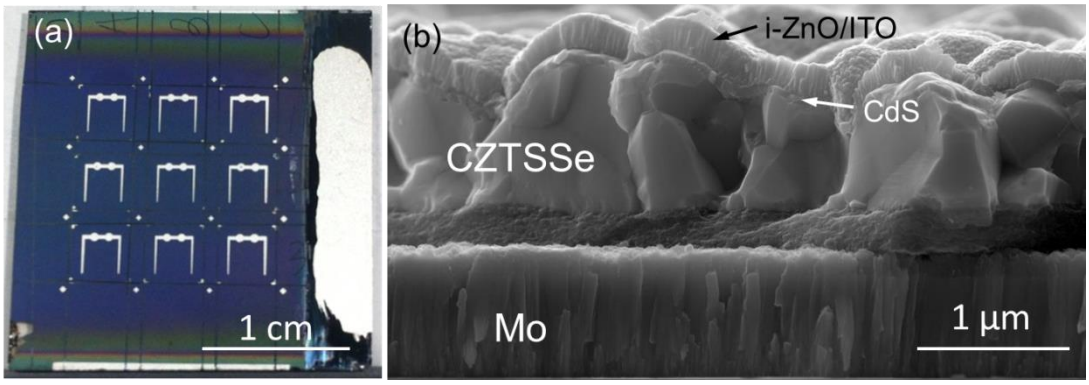

Figure 6.9 (a) Top-view photo of a typical completed PV substrate with nine 0.16 cm^2 devices defined by scribing. (b) Cross sectional SEM image of a complete device.

For efficient current collection, front contact grids were deposited by electron beam evaporation of ~50 nm thick Ni and ~1 μm thick Al through a shadow mask. The final devices were defined by mechanical scribing to provide a total area of ~0.16 cm^2. A photo of the final devices and a typical cross-sectional SEM image with the configuration of Mo/CZTSSe/CdS/i-ZnO/ITO/Ni-Al are given in Figure 6.9.

6.2 The effect of CZTS nanoparticle inks on the performance of CZTSSe solar cells

6.2.1 Four types of CZTS nanoparticle inks

The properties of the CZTS nanoparticle inks can be controlled via the reaction conditions as described in chapter 5. In this section, the reaction parameters temperature, time and cooling mode were selected to study their role in determining the device performance. To that end four CZTS nanoparticle inks were prepared. The first ink was a control sample which was obtained by setting the reaction temperature

to 225 ℃ for 30 minutes. Subsequent to the reaction, the control ink was allowed to cool down relatively slowly (~ 5 ℃/min) under ambient laboratory conditions with the aim of producing the kesterite structure. The remaining three nanoparticle inks were fabricated by systematically changing one of the reaction parameters. The reaction parameters that were not changed were set to be identical to the control sample. Specifically for investigation of the effect of cooling mode on PV cell performance, the reaction was quenched by rapidly cooling (~ 20 ℃/min) the reaction vessel in an ice-bath. Similarly, for temperature, a relatively hot temperature of 255 ℃ was set. Finally, for time, the reaction was prolonged to 60 minutes. The key reaction parameters for these four types of nanoparticle inks are summarised in Table 6.2.

Table 6.2 Reaction parameters and main differences between the four types of nanoparticle inks.

Samples	Key reaction parameters	Ink properties
Control	225 ℃, 30 min Slow cooling	Kesterite CZTS
Quenched	Rapid cooling	Kesterite + wurtizte CZTS
Hot	255 ℃	Kesterite CZTS + CTS
Prolonged	60 minutes	Kesterite CZTS

The crystal properties of the four types of nanoparticle ink were studied by XRD and Raman spectroscopy (Figure 6.10).

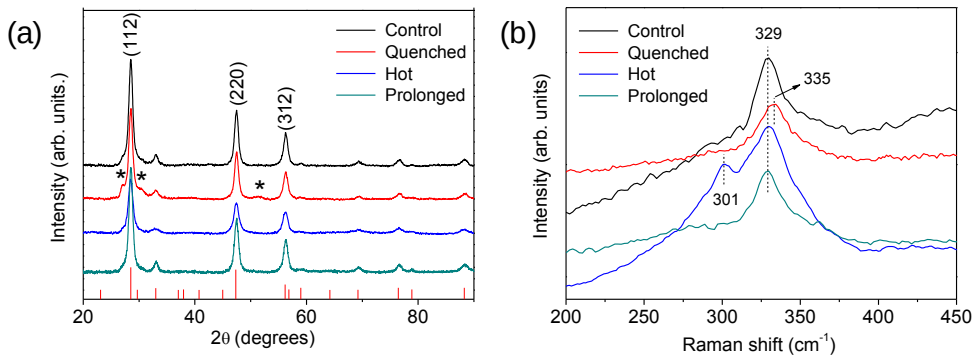

Figure 6.10 (a) XRD patterns of CZTS thin films deposited from different nanoparticle inks. The red reference pattern is kesterite CZTS (PDF 026-0575). (b) Raman spectra of CZTS nanoparticles prepared at different reaction conditions. Diffraction patterns and Raman spectra are off-set for better visibility.

As shown in Figure 6.10 (a), the major XRD diffraction peaks of the control sample can be indexed to kesterite CZTS (PDF 026-0575). The quenched sample exhibits three weak diffraction peaks marked by asterisks shown in Figure 6.10 (a) in addition to the primary peaks. As discussed in chapter 5, these three peaks belong to the co-existing wurtzite CZTS in the nanoparticle ink. XRD patterns of the hot and prolonged samples have a similar pattern to kesterite CZTS with no obvious secondary phases observed.

The crystal structures of the samples were further studied by Raman spectroscopy as shown in Figure 6.10 (b). For the control sample, the main peak located at 329 cm^{-1} belongs to kesterite CZTS. Due to the mixed atomic arrangement of kesterite and wurtzite phases, the main peak of the quenched sample shifts to 335 cm^{-1}. For the hot sample, a strong peak at 329 cm^{-1} corresponding to CZTS is detected, though there is

also a nearby shoulder peak at 301 cm^{-1}, which belongs to tetragonal CTS. For the prolonged sample however, only one characteristic peak located at 329 cm^{-1} is observed, and has a similar spectrum to the control. These differences are summarised in Table 6.2.

6.2.2 Photovoltaic device performance

Following the procedures described in section 6.1, four substrates were prepared with nine 0.16 cm^2 devices per substrate, using the four types of nanoparticle ink. Devices differ only in the precursor ink used and all other conditions were kept identical during the fabrication.

J-V curves of the best device built on each substrate are shown in Figure 6.11 with the device parameters extracted from these *J-V* curves summarised in Table 6.3. Additionally, the distributions of efficiency (η), open circuit voltage (V_{oc}), short circuit current density (J_{sc}), and fill factor (FF) of the nine devices on each substrate are shown in Figure 6.12 demonstrating the high uniformity of device performance across the substrates.

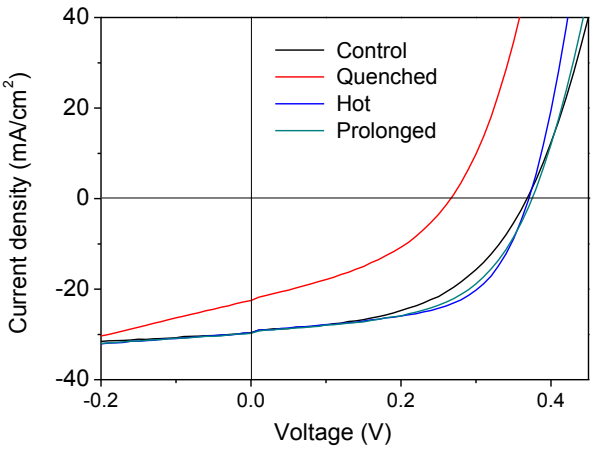

Figure 6.11 *J-V* curves of devices with absorber made from different nanoparticle inks.

Table 6.3 Device parameters for the solar cells shown in Figure 6.9.

Device	η (%)	V_{oc} (V)	J_{sc} (mA/cm^2)	FF (%)	R_S (Ω.cm^2)	R_{SH} (Ω.cm^2)	E_g-qV_{oc} *(eV)*
Control	5.41	0.36	29.6	50.7	3.09	77	0.70
Quenched	2.30	0.26	22.5	39.2	4.37	31	0.86
Hot	6.26	0.37	29.7	57.0	1.86	116	0.65
Prolonged	5.98	0.37	29.7	54.3	2.42	139	0.68

Baseline photovoltaic parameters for the control device can be derived from Figure 6.11: η = 5.41 %, V_{oc} = 0.36 V, J_{sc} = 29.6 mA/cm^2, and FF = 50.7 %. The most striking contrast to this set is found for the quenched reaction conditions as the presence of wurtzite phase CZTS has a profound effect on the device efficiency which drops to η = 2.30 %. This indicates that the reaction cooling mode which affects the atomic arrangement, has a direct negative influence upon the device performance.

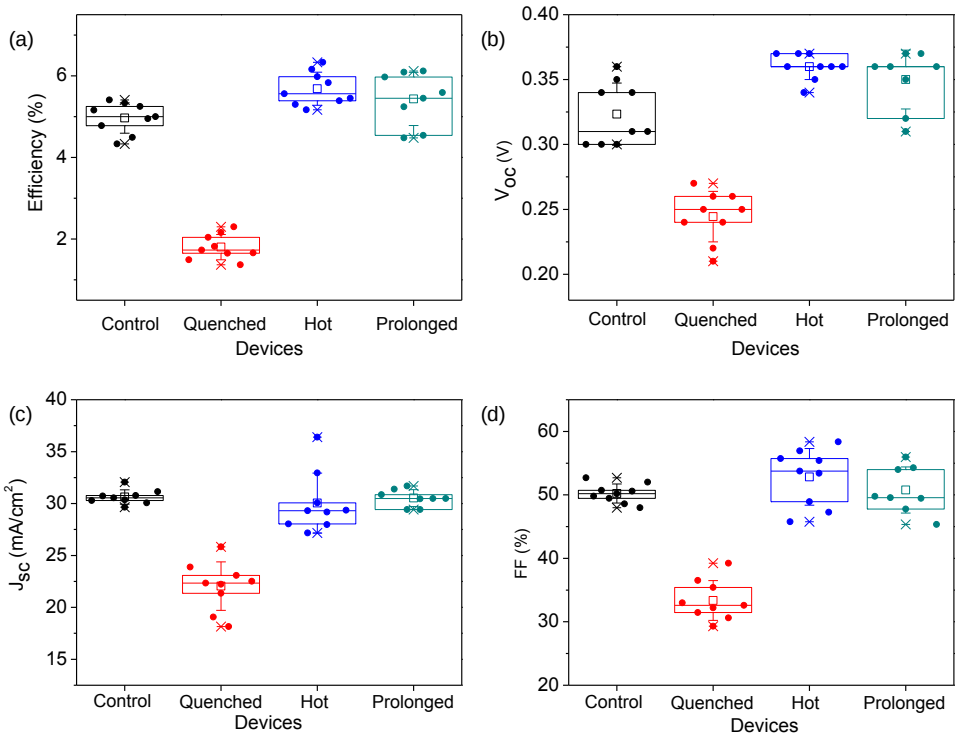

Figure 6.12 The distribution of (a) efficiency, (b) V_{oc}, (c) J_{sc} and (d) *FF* of the nine devices on each substrate. □ is the average value and × is the minimum and maximum position. The three horizontal lines of each box stand for the 25%, 50% and 75% of the reading distribution. The whisker range is determined by the standard deviation of the nine readings.

As shown in Table 6.3, the reduced efficiency of this device arises not only from reductions in V_{oc} and J_{sc}, but also a large drop in *FF* caused by higher series resistance (R_S) and lower shunt resistance (R_{SH}). As shown in Figure 6.13 (a), the selenised thin film made from control sample is composed of densely packed grains that can be up to 2 μm, with no obvious voids or cracks on the surface. However, as can be seen in Figure 6.13 (b), the grain size of the CZTSSe film made from the quenched sample is significantly smaller than that of the control. Considering the sheet resistance of the Mo and ITO is 0.2 Ω/□ and 35 Ω/□ respectively, the increased

parasitic resistance of the quenched device is likely derived from increased density of grain boundaries which act as recombination centres. It is possible that wurtzite phase CZTS undergoes a phase transition to kesterite during the selenisation stage [82], however this wurtzite CZTS may hinder the grain growth process and even present a residual component that significantly degrades device performance. Figure 6.11 (a) also shows the *J-V* characteristic for the devices with hot and prolonged reaction conditions. These devices have higher efficiencies relative to the control and this is manifested through higher fill factors which are accompanied by lower R_S and higher R_{SH} values. The former is likely to be influenced by the unconverted nanocrystals and the $Mo(S,Se_2)$ layer at the back of the device [16] while R_{SH} is influenced by the CZTSSe grain size. Analysis of Figure 6.13 reveals that the prolonged reaction time results in a selenised thin film that has slightly larger grains (Figure 6.13 (d)) compared with the hot reaction condition (Figure 6.13 (c)). This reduces the number of grain boundaries and in turn, the number of shunting pathways [140] resulting in higher R_{SH} values.

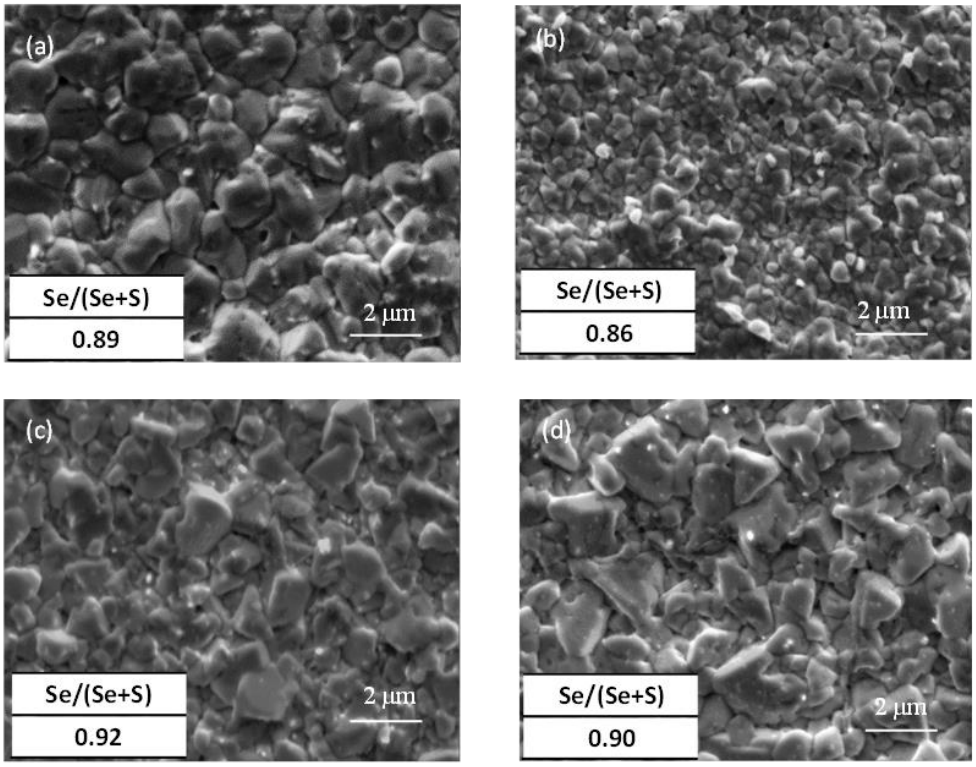

Figure 6.13. Surface morphologies of CZTSSe film made from (a) control sample, (b) quenched sample, (c) hot sample and (d) prolonged sample. The insets show the Se/(Se+S) ratios of the films.

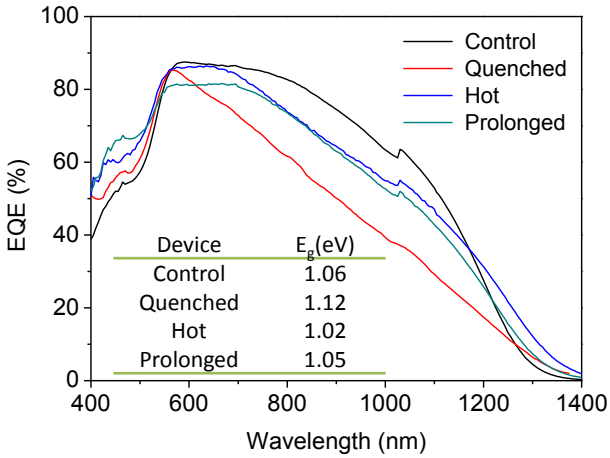

Figure 6.14 EQE spectra of devices with absorber made from different nanoparticle inks. The step in EQE spectra at 1030 nm is an artefact arising from a change in detector. The inset shows the energy bandgap E_g determined from the EQE spectra by the extrapolating the linear portion of the curve $[hv \times \ln(1\text{-EQE})]^2$ against hv.

The EQE spectra of the devices in Figure 6.14 show behaviour that is consistent with the *J-V* characteristics. All devices show less ideal EQE toward longer wavelengths which is a result of recombination losses that can be attributed to the fine-grain and $Mo(S,Se)_2$ layers [80]. In addition, the spectrum for the quenched device (E_g = 1.12 eV) exhibits a strong triangular shape indicative of severe current collection losses. The variations in energy bandgap derived from the band tail of the EQE spectra are consistent with the fluctuations in Se/(Se+S) ratios as measured by EDS (Figure 6.13 insets). It is interesting to note that quenched sample yields less Se incorporation into the CZTS lattice compare to the other three processes which have similar Se/(Se+S) ratio at around 0.90. This further proves the wurtzite CZTS may hinder the Se incorporation and grain growth.

The hot device exhibits the highest overall efficiency of η = 6.26 %, with V_{oc} = 0.37 V, J_{sc} = 29.7 mA/cm^2, and *FF* = 57.0 %. Raman spectroscopy revealed that this film contained secondary CTS phase and this champion efficiency is consistent with the current world record efficiency for CZTSe thin films fabricated using selenisation of CZTS nanoparticles which were also found to contain CTS [16]. The reason for this is currently not well-understood and merits further investigation.

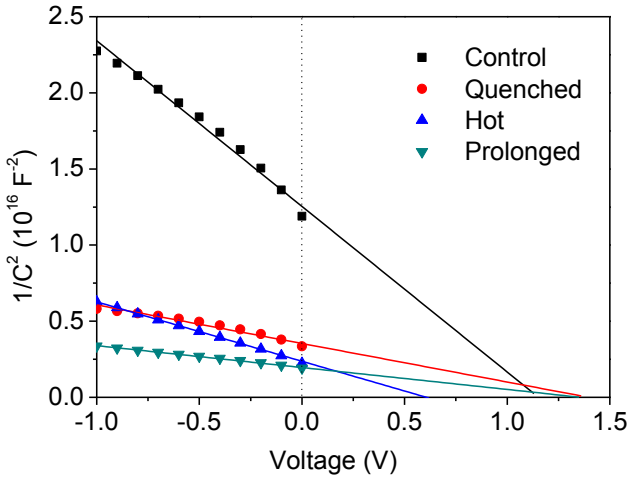

Figure 6.15 $1/C^2$ versus reverse bias voltage plots of devices with absorber made from different nanoparticle inks.

C-V measurements were performed to estimate the carrier density N_A, the built-in potential V_{bi} and depletion layer width W in the CZTSSe absorber layer of the completed devices using Equation 4-20. Figure 6.15 shows a plot of $1/C^2$ versus reverse bias voltage for the devices and from the slope and intercept of the linear fits, N_A and V_{bi} can be determined respectively. Additionally, the width of the depletion region W can be deduced from the data. These values for all four samples are listed in Table 6.4 where the values are comparable to vacuum [141] or hydrazine-based CZTS [15] fabrication methods confirming that there is no loss of junction quality using the nanocrystal fabrication route.

Table 6.4 Junction parameters extracted from *C-V* measurements.

Device	N_A (cm^{-3})	W (nm)	V_{bi} (V)
Control	4.4×10^{16}	117	1.14
Quenched	2.8×10^{17}	62	1.36
Hot	2.0×10^{17}	51	0.62
Prolonged	5.3×10^{17}	47	1.35

As discussed in section 3.1.5, CZTSSe is usually reported to be *p*-type arising from a large number of Cu vacancies V_{Cu}^{-}, and antisite defects such as Zn_{Cu}^{+}. Comparisons between all four devices in terms of doping are difficult because the crystal structure has been shown to be markedly different between the samples and therefore cannot easily be attributed to the density of V_{Cu}^{-} (despite all absorbers being Cu poor). However, we have demonstrated a high degree of similarity between the control and the prolonged samples and devices, and the most obvious discrepancy is indeed N_A which is an order of magnitude higher for the prolonged sample. It is this parameter that results in a higher solar energy conversion efficiency and indicates that the carrier density can be increased without changing the crystal structure of a CZTSSe absorber synthesised from nanoparticle inks. The increase in efficiency derives from an increase in V_{oc} and *FF* for the prolonged device.

Although the interpretation of the *C-V* data for the quenched and hot devices is more difficult, the increased values of N_A for these devices relative to the control could be a consequence of increased disorder in the crystal structure. The case of the hot

device is particularly interesting because it results in the highest efficiency of all the devices. This is consistent with the earlier analysis of the doping concentration between the control and the prolonged device. The key difference here however, is that the higher reaction temperature correlates with the presence of secondary phase CTS. These findings are important in the context of work by Miskin *et al.* who recently demonstrated a CZTSSe nanoparticle ink solar cell with η = 9 % (with an anti-reflection coating) [16] but do not account for an experimentally observed CTS phase which has previously been thought to be detrimental to solar cell performance due to a narrower energy bandgap. The results of this work indicate that the apparent positive effects of CTS may be due to an effective increase in the absorber doping which in turn enhances V_{oc} in the device. The apparent increase in V_{oc} is seen more clearly by considering that the voltage deficit (E_g-qV_{oc}) (also shown in Table 6.3) is minimised for the hot device.

As discussed in section 2.2.1, the electric field in the *n*-type and *p*-type region of a *p*-*n* junction depends on the density of donors and acceptors respectively. Continuity of the field requires that the width of the depletion region varies inversely with doping concentration *i.e.* that the depletion region extends into the side with lower doping. This is consistent with the control device having the largest *W* value (Table 6.4) and the highest EQE in the 700-1150 nm range testimony of the better charge collection in that device. The values of V_{bi} are similar apart from the hot sample and this is likely attributable to the presence of CTS which reduces the energy bandgap

of the absorber.

6.3 Summary

High quality CZTSSe photovoltaic absorber layers were fabricated from CZTS nanoparticle inks by selenising stacked layers of nanoparticles in a selenium rich atmosphere. These were subsequently incorporated into thin film solar cells and the device performance has been found to depend critically upon the chemical reaction conditions used to synthesise the nanoparticles. Crucially, rapid thermal quenching of the reaction results in wurtzite CZTS atomic arrangement which was observed to be strongly detrimental to the device performance. Prolonging the reaction offers a new route to increasing the concentration of acceptor levels in CZTSSe photovoltaic absorbers and results in higher device efficiency relative to a control device. The presence of CTS correlates with highest efficiency achieved of 6.3 % and the apparent positive effects of this phase are also accompanied by an increase in the doping levels.

Chapter 7

Selenisation kinetics and their effect on device performance

In addition to the nanoparticle ink fabrication, a key step in the fabrication of high quality CZTSSe thin film PV absorber layers is high temperature selenisation. Here the goal is to convert CZTS nanoparticles into large CZTSSe grains while minimising the number of grain boundaries. In order to optimise this part of the fabrication process, the film morphology and variation in composition are studied as a function of the selenisation process. In section 7.1, the composition and morphology of CZTS thin film absorbers are systematically investigated as a function of selenisation time, temperature and selenium vapour pressure, which provide systematic data to analyse the reaction kinetics of the selenisation process. The selenised films are subsequently incorporated into CZTSSe photovoltaic cells and their performance is assessed in section 7.2.

7.1 Selenisation process kinetics

To investigate the kinetics of the CZTS selenisation process, two series of experiments were conducted to systematically study variations of the thin film morphology and composition as a function of selenisation time and temperature. In the first series, time-dependent experiments were performed by changing the selenisation time (5, 10, 20 and 40 minutes) with the temperature held constant

(500 ℃). In the second series, temperature-dependent experiments were performed by changing the temperature (450, 500, 550 and 600 ℃) for a constant selenisation time (20 minutes). All time and temperature dependent experiments were performed with ~300 mg of selenium loaded in the graphite box. Using the methodology introduced in section 6.1.2, the partial pressure of selenium P_{e,Se_2}, within the graphite box after pressure equilibration was stable at 140 mbar for time-dependent experiments. For the temperature-dependent measurements, P_{e,Se_2} increased slightly from 120 mbar at 450 ℃ to 150 mbar at 600 ℃ and its influence on the grain growth was negligible in this series. However, the influence of selenium vapour pressure on the grain growth was detailed discussed in section 7.1.3. The selenium vapour pressure-dependent experiments were performed by changing the vapour pressure (31, 53, 75, 140, and 226 mbar) with temperature held constant at 500 ℃ for 20 minutes.

7.1.1 Time-dependent kinetics

Time-dependent experiments were firstly performed to understand kinetic variations of morphology and composition during the grain growth. The cross sectional SEM images of the thin films selenised for different times are shown in Figure 7.1.

For CZTSSe films fabricated from nanoparticle inks, the absorber layer generally has a bilayer structure composed of a thin fine-grained layer at the interface with the substrate and large-grained layer on top [11, 16]. From Figure 7.1, it is clear that a

longer selenisation period results in a thicker large-grained layer and a thinner fine-grained layer. However, it can be qualitatively seen that the rate of grain growth is not constant during the selenisation process: grain growth is initially fast and then slows for longer selenisation times.

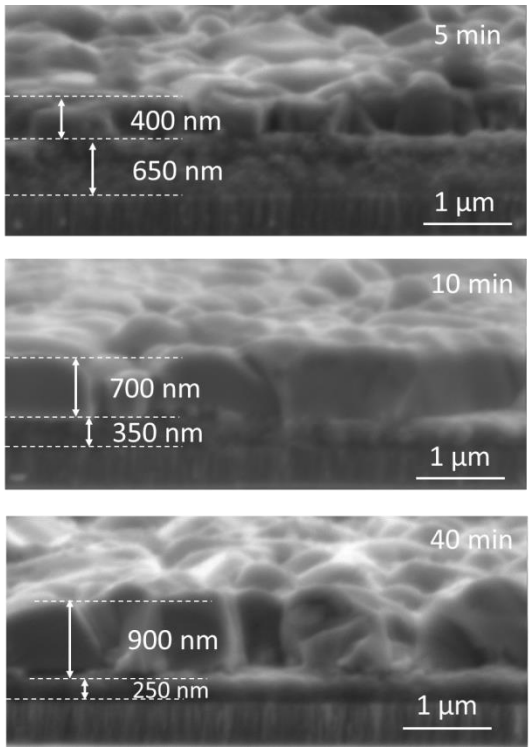

Figure 7.1 Cross-sectional SEM images of CZTSSe thin films obtained at different selenisation times each at 500 ℃.

The reaction kinetics of the selenisation process have previously been explained using a parabolic model [142, 143]. In this model, the selenisation process can be considered to be a solid-gas reaction as depicted in Figure 7.2 (a) where a layer of CZTSSe nuclei is formed at the interface between the CZTS precursor layer and the Se_2 gas phase at the start of the reaction. As the reaction proceeds, more selenium

diffuses into deep CZTS layer to induce large-scale CZTSSe grain growth. The parabolic growth model is described by:

$$x^2(t) = K_p t \qquad (7\text{-}1)$$

where $x\,(t)$ is the thickness (μm) of the CZTSSe layer, K_p is a rate constant (μm^2/min), t is heat treatment time (minutes).

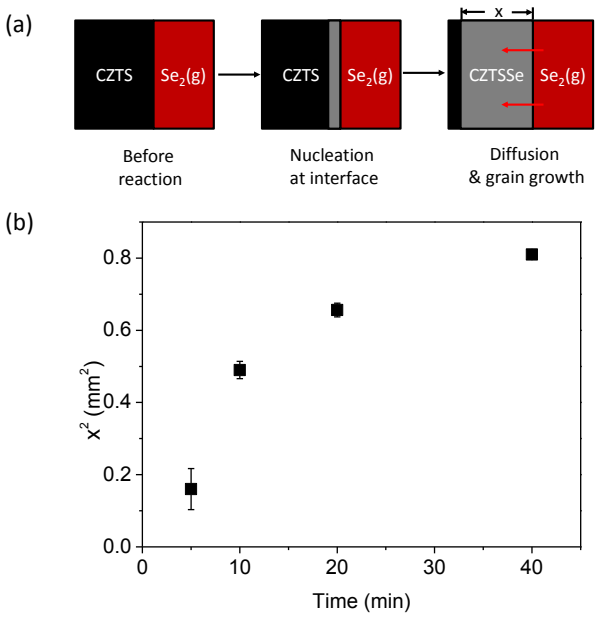

Figure 7.2 (a) Schematic diagram of grain growth in a solid-gas reaction process. (b) Plot of large grain layer thickness squared versus heat treatment time.

For parabolic grain growth, there should be a linear relationship between x^2 and t. However, as shown in Figure 7.2 (b), this is clearly not the case and suggests that the rate constant K_p, is time dependent. The parabolic model assumes that the selenisation rate is proportional to the flux of selenium anions through the resultant larger grain layer and the diffusion of selenium anions is the rate-controlling step of the reaction. For x^2 to depend linearly on time, the diffusivity of the CZTSSe large

grain layer is assumed to be a constant. This assumption implies that the resultant large grain should be uniform, continuous and of single phase during the heat treatment period. However, analysis of the thin films at different selenisation times reveals that the composition of the absorber layer is time-dependent. As shown in Table 7.1, about 80 % of sulphur is replaced by selenium in the first 5 minutes of the heat treatment. This increases to 94 % after 40 minutes. As a result, the CZTSSe grain growth reaction process cannot be simply described by parabolic kinetics.

Table 7.1 Composition variations of sulphur and selenium in CZTSSe thin films for different selenisation times at 500 ℃.

Time (minutes)	S (at%)	Se (at%)	α=Se/(S+Se)
5	12.44	48.21	0.79
10	6.30	48.36	0.88
20	5.24	48.01	0.90
40	2.97	49.85	0.94

In addition to the parabolic model (solid-gas reaction process), CZTSSe grain growth reaction can be described as a phase transformation from the parent CZTS phase to CZTSSe following Avrami's model [142, 143]. This is illustrated in Figure 7.3 (a) where a significant number of CZTSSe nuclei are rapidly formed at the beginning of reaction under an isothermal process. As more selenium diffuses into the thin film during the intermediate period, nuclei grow into large grains by dissolution of the

parent CZTS lattice and reformation of the selenium-based lattice. Once the conversion nears completion, there is little untransformed CZTS left for nuclei to form and the process begins to slow. The Avrami model is given as:

$$\ln[-\ln(1-\alpha)] = n_a \ln(K_a) + n_a \ln(t) \qquad (7\text{-}2)$$

where α is conversion ratio and equal to *Se/(S+Se)*, n_a is Avrami's exponent, K_a is Avrami's rate constant (min^{-1}) and t is the heat treatment time (min). A plot of $\ln[-\ln(1-\alpha)]$ versus $\ln(t)$ (known as a Sharp-Hancock plot) is given in Figure 7.3 (b). Fitting Equation 7-2 to these data yields an Avrami's exponent and rate constant of 0.24 and 1.95 min^{-1}, respectively. An Avrami exponent of <1 indicates that the selenisation reaction is controlled by an irregular one-dimensional process as explained next.

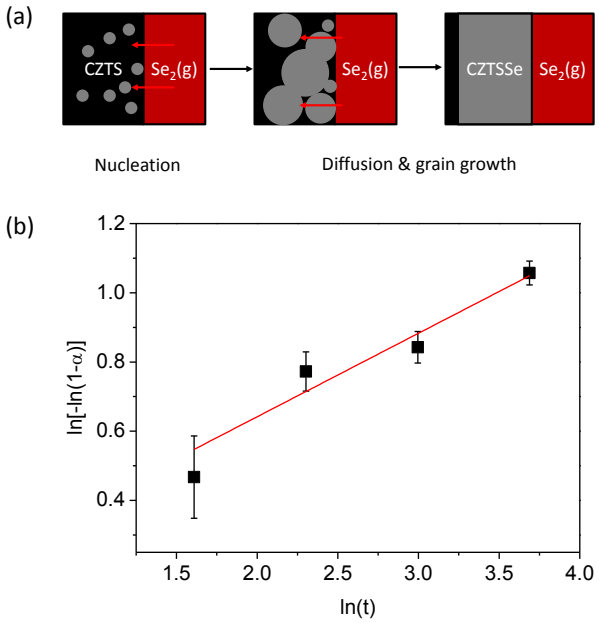

Figure 7.3 (a) Schematic diagram of grain growth following Avrami's model. (b) Sharp-Hancock plot for CZTS selenised at 500 ℃.

The half-selenisation time $t_{1/2}$ can be calculated for α = 0.5:

$$t_{1/2} = \frac{1}{K_a}(ln2)^{1/n_a} \qquad (7\text{-}3)$$

Using the values of n_a and K_a obtained from Figure 7.3, it only takes about 7 seconds to complete 50 % of the selenium conversion. The relatively fast selenium incorporation therefore indicates that the CZTSSe grain growth is limited by cation re-ordering rather than selenium incorporation. This finding is consistent with the work reported by Mainz *et al.* that selenium incorporation is completed during the first few seconds of $Cu_2InGaSe_4$ film formation [144]. However, longer annealing times are still required for the formation of large grains.

The CZTSSe grain growth process can be further studied by analysing the grain sizes of the layer as this is an important parameter indicative of the quality of polycrystalline thin films. Normal grain growth at a constant temperature can be explained by considering that the average grain radius r depends on the annealing time t through [145]:

$$r^n - {r_o}^n = Kt \qquad (7\text{-}4)$$

where r is the average grain radius after selenisation (μm), r_o is the initial grain radius (which can be ignored here as the initial nanoparticles are much smaller than the converted CZTSSe grains), K is the grain growth coefficient, n is the grain growth exponent and related to the initial grain structures. It is expected to have a

value of 2 when the as-deposited film has an equiaxed grain structure and can be up to 5 if the initial structure is columnar [145, 146].

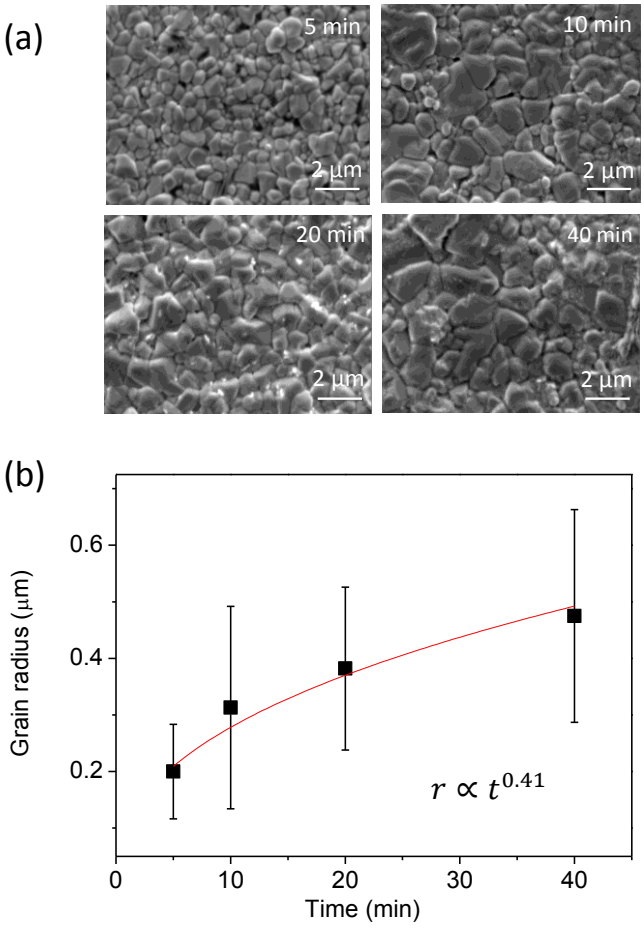

Figure 7.4 (a) Top view SEM images and (b) the average grain radius of CZTSSe thin film for different selenisation periods at 500 ℃. The red line is the fitted power function curve.

The average grain radius r of the CZTSSe thin film after selenisation can be measured from top-view SEM images as shown in Figure 7.4 (a) where it is qualitatively shown that a longer selenisation time results in larger grains. From Equation 7-4, it can be seen that $r \propto t^{\frac{1}{n}}$ (neglecting the intial grain radius). A fit to the data (Figure 7.4 (b)) yields n=2.44 which further indicates that the as-deposited thin film is formed by nearly equiaxed grains.

7.1.2 Temperature-dependent kinetics

From the previous section, the grain growth exponent *n* was calculated to be 2.44. Using this value and $K = K_o \exp(-\frac{Q}{RT})$ [145] as the model of grain growth coefficient, Equation 7-4 can be revised into a temperature-dependent model:

$$\ln(r^{2.44}) = \ln(K_o t) - \frac{Q}{RT} \qquad (7\text{-}5)$$

where K_o is weakly temperature dependent constant and depends on the grain geometry and average grain boundary energy, *t* is the selenisation time, *Q* is the activation energy for grain boundary motion (kJ/mol), *R* is the gas constant (8.31 J mol^{-1} K^{-1}) and *T* is the selenisation temperature (K). In order to validate Equation 7-5, a series of experiments were performed in which the selenisation temperature was altered from 450 to 600 ℃ with a fixed dwell time of 20 minutes. The top view and corresponding cross-sectional SEM images of the thin films are shown in Figure 7.5 where increasing the selenisation temperature produces larger grains from less than 0.5 μm at 450 ℃ to more than 1.5 μm at 600 ℃ (Figure 7.6).

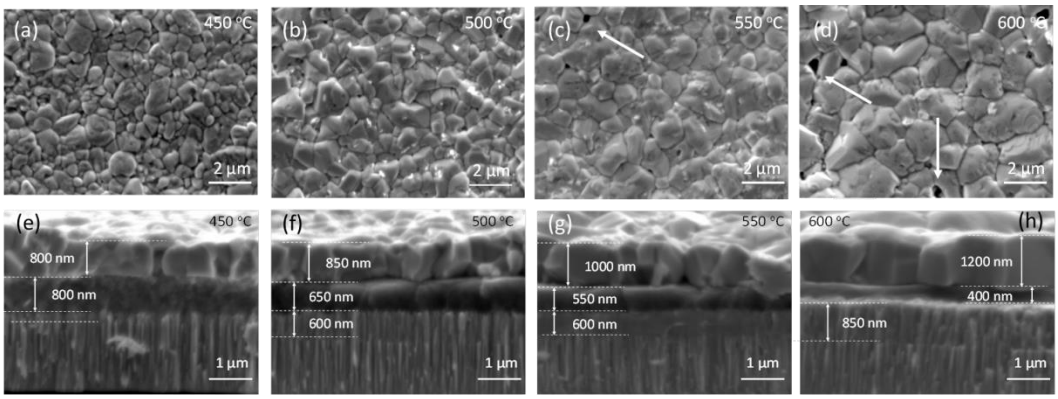

Figure 7.5 (a-d) Top-view and (e-h) cross sectional SEM images of CZTSSe thin film obtained at different selenisation temperatures for 20 minutes. White arrows highlight features refered to in section 7.2.2.

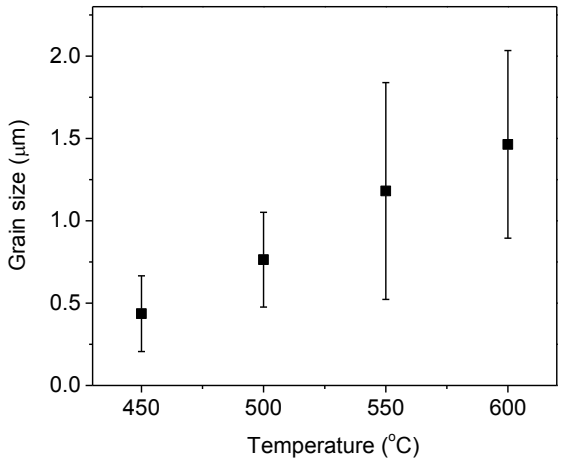

Figure 7.6 Average grain sizes at different selenisation temperatures.

Furthermore, higher temperatures result in more selenium being incorporated into the lattice to facilitate grain growth (Table 7.2), which indicates that the selenium conversion process is both time and temperature dependent. Similar to the time-dependent experiments, higher temperature results in thicker large-grained layers and thinner fine-grained layers (Figure 7.5 (e-h)). Once the thin films have an average grain size comparable to the thickness of the large-grained layer, the grain

growth slows down and eventually stops resulting in columnar grain structures [145].

Table 7.2 Composition variations of sulphur and selenium in the thin films at different temperatures for a selenisation time of 20 minutes.

Temp. (℃)	S (at%)	Se (at%)	α=Se/(S+Se)
450	8.51	45.24	0.84
500	5.24	48.01	0.90
550	4.47	50.05	0.92
600	3.89	51.07	0.93

Based on Equation 7-5, a plot of $\ln(r^{2.44})$ versus $1000/T$ is given in Figure 7.7. A linear fit indicates CZTSSe grain growth follows a normal grain growth process and from the slope of the fit, an energy of 85.38 kJ/mol is needed to activate the CZTSSe grain boundary migration for consume of small grains.

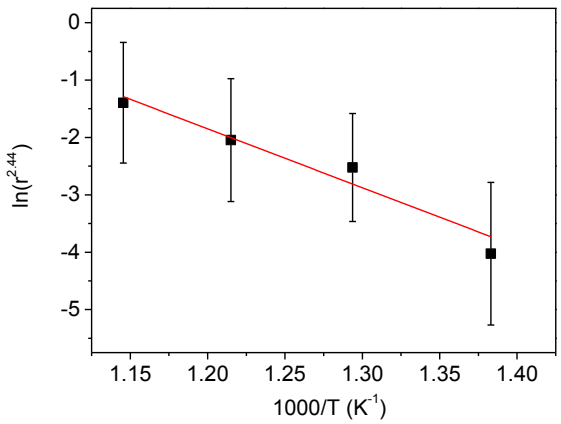

Figure 7.7 A plot of $\ln(r^{2.44})$ versus 1000/T.

7.1.3 Dependence on selenium vapour pressure

Although the selenium vapour pressure variations can be ignored when the selenisation temperature increases from 450 ℃ to 600 ℃, it is necessary to investigate the effect of selenium vapour pressure at fixed temperature in determining the properties of absorber layer. Selenium vapour pressure dependent experiments were performed by varying the equilibrium selenium vapour pressure from 31 mbar to 226 mbar by changing the amount of selenium loaded in the graphite box with temperature fixed at 500 ℃ for 20 min.

The top-view SEM images of the thin film selenised in different selenium vapour pressures are summarised in Figure 7.8. It is shown that higher vapour pressure results in larger grains.

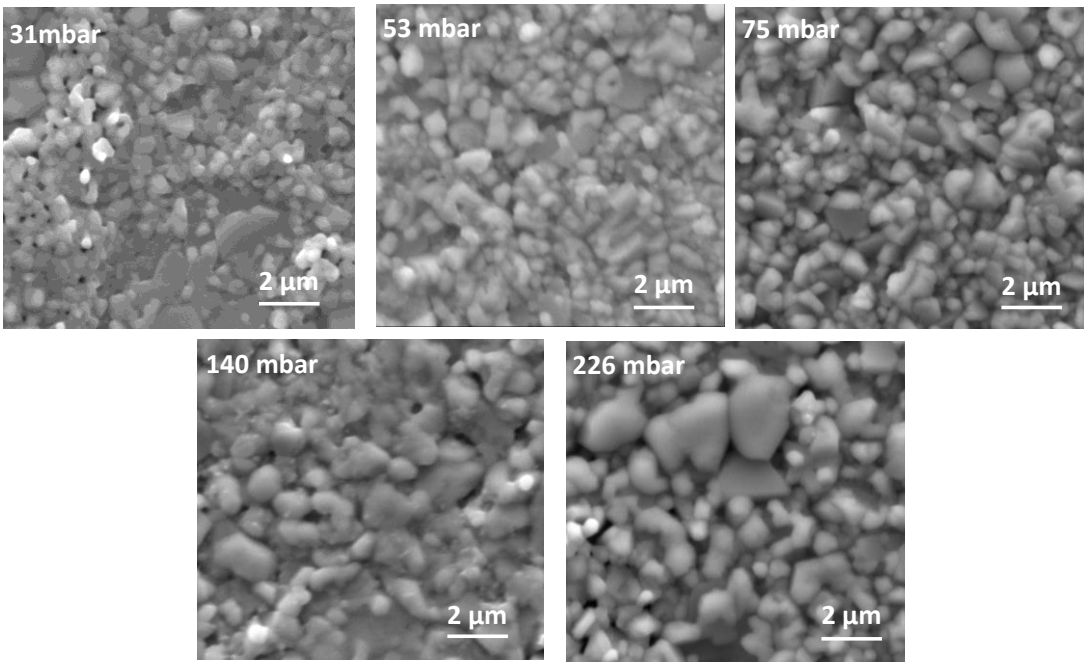

Figure 7.8 Top view SEM images of CZTSSe thin film selenised under different selenium vapour pressure at 500 ℃ for 20 minutes.

The average grain radius *r* of the CZTSSe thin film after annealing can be measured from top-view SEM images. The average grain radius is then plotted as a function of selenium vapour pressure in Figure 7.9.

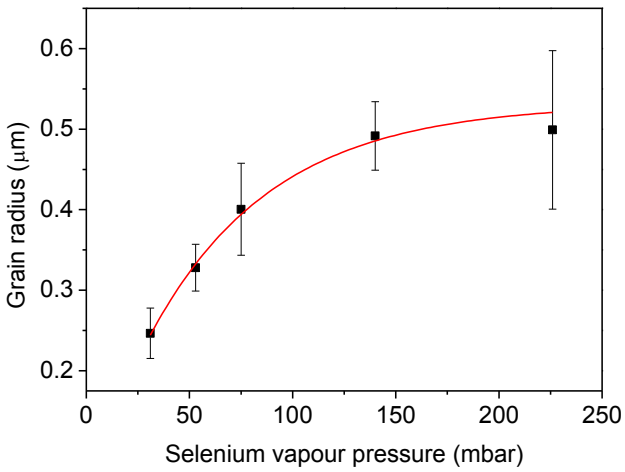

Figure 7.9 The average grain radius of CZTSSe thin film obtained under different selenium vapour pressure at 500 ℃ for 20 minutes. The red line is the fitted exponential curve.

As shown in Figure 7.9, an exponential function fits the average radius data well as given by:

$$r = 0.53 - 0.48 \cdot \exp\left(\frac{-P_{e,Se_2}}{59.8}\right) \qquad (7\text{-}6)$$

where r is the average grain radius after selenisation (μm), P_{e,Se_2} is the selenium equilibrium vapour pressure (mbar). According to Equation 7-6, the grain radius of the initial nanoparticles is estimated to be 50 nm when P_{e,Se_2} is 0 and no selenisation process is applied to the CZTS nanoparticle precursor thin film. This fitting grain radius agrees well with the actual CZTS nanoparticle sizes as studied in section 6.1. According to Equation 7-6, even extremely high selenium vapour pressure is applied in the selenisation process at 500 ℃ for 20 minutes, CZTSSe grains cannot grow infinitely but will saturate with an average radius of ~ 0.53 μm.

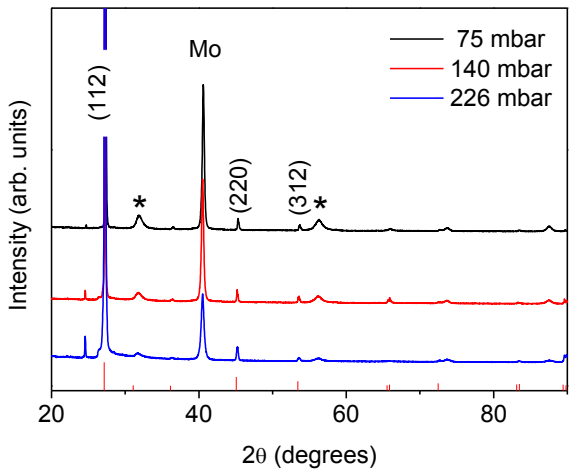

Figure 7.10 XRD patterns of thin film selenised under different selenium vapour pressures at 500 ℃ for 20 minutes. The peaks marked by * belong to $Mo(S,Se)_2$. The red lines at the bottom are the reference pattern of CZTSe (PDF 052-0868).

XRD was used to study the crystal quality variations of the thin films. As shown in Figure 7.10, the sharp peaks of the thin films can be assigned to CZTSe (PDF 052-0868, Mo peak is from the Mo-SLG substrate). However, there is a slight shift of the reflections to higher angles because of residual sulphur present in the lattice even under high selenium vapour pressure [114]. Depending on this XRD shift, the Se/(S+Se) ratio is calculated to increase from 0.89 for 75 mbar to 0.97 for 226 mbar. Higher selenium vapour pressure results in more selenium being incorporated into the lattice to facilitate grain growth, which indicates that the selenium conversion process is also selenium vapour pressure dependent. As shown in Figure 7.10, among the diffraction peaks belonging to CZTSSe lattice planes, the intensity of the (112) diffraction peaks increases with increasing selenium vapour pressure, which indicates the improvement of the CZTSSe crystallinity along the [112] direction

under higher selenium vapour pressure. In addition to the characteristic peaks of CZTSSe, two peaks belonging to $Mo(S,Se)_2$ are also observable around 32 ° and 56 °. Opposite to the crystallinity improvement of CZTSSe thin films, it is interesting to find that the $Mo(S,Se)_2$ peaks show degraded intensity when higher selenium vapour pressure was applied in the selenisation process. The cross sections of the CZTSSe thin films are further explored to explain these XRD pattern variations.

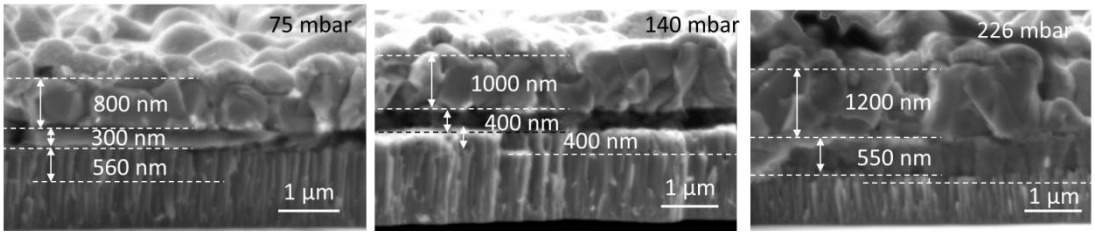

Figure 7.11 Cross-sectional SEM images of finished devices using CZTSSe thin film selenised under different selenium vapour pressures.

As shown in Figure 7.11, the cross-sectional images of the selenised thin films all reveal a four-layer structure. As studied in section 6.1.1, from the bottom is the Mo substrate with a columnar grain structure, a $Mo(S,Se)_2$ layer formed under the selenium-rich selenisation conditions, a carbon rich residual fine-grained layer, and a carbon free large-grained CZTSSe layer. Higher selenium vapour pressure promotes selenium diffusion into the precursor thin film and facilitates the growth of large-grained layer. The thicker large-grained CZTSSe layer obtained under higher vapour pressure provides stronger XRD diffraction as observed in Figure 7.10. However, thicker residual fine-grained layers and thinner $Mo(S,Se)_2$ layers are observed under higher selenium vapour pressures. The decreasing of $Mo(S,Se)_2$ layer

thickness then takes account for the decay of $Mo(S,Se)_2$ XRD characteristic peaks as studied in Figure 7.10.

7.2 Device performance

CZTSSe thin films prepared at different times, temperatures and selenium vapour pressures were integrated into thin film solar cells and performance of the devices is analysed in this section.

7.2.1 Influence of selenisation time

J-V curves obtained from the best devices at each selenisation time are shown in Figure 7.12 with the device parameters extracted from the *J-V* curves summarised in Table 7.3. Additionally, the distributions of η, V_{oc}, J_{sc}, and *FF* from all nine devices on each substrate are shown in Figure 7.13 demonstrating the high uniformity of device performance across the substrates.

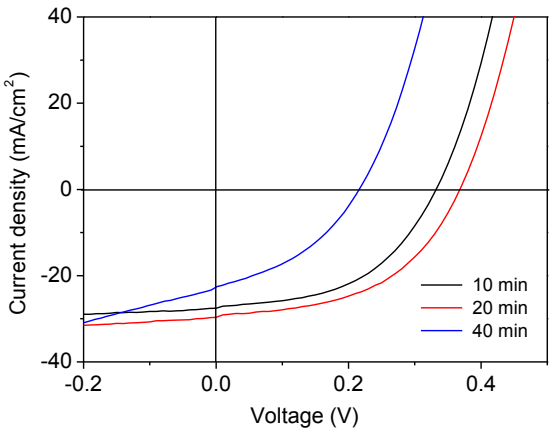

Figure 7.12 *J-V* curves of solar cells with CZTSSe thin film absorbers annealed for different times at 500 ℃.

Table 7.3 Device parameters for the solar cells with *J-V* curves shown in Figure 7.12.

Device (minute)	η (%)	V_{OC} (V)	J_{SC} (mA/cm^2)	*FF* (%)	R_S (Ω·cm^2)	R_{SH} (Ω·cm^2)
10	4.48	0.33	27.5	49.3	3.2	122
20	5.41	0.36	29.6	50.7	3.1	77
40	1.90	0.21	22.5	39.8	3.9	21

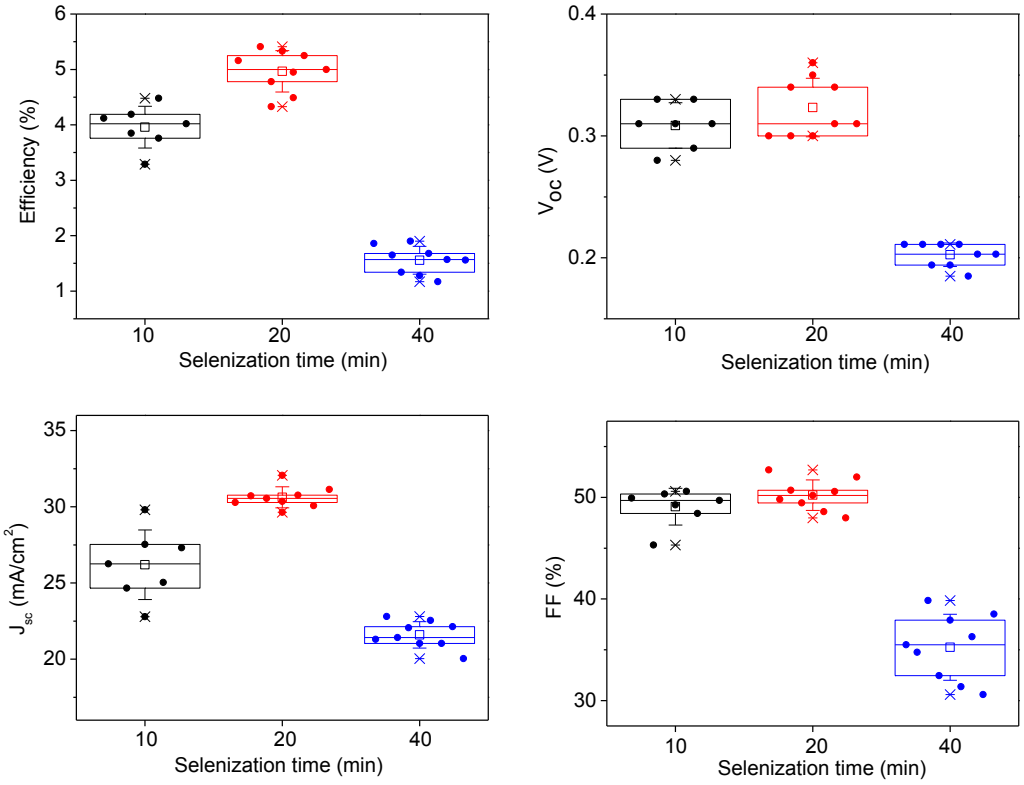

Figure 7.13 Performance distributions of solar cells fabricated using CZTSSe thin films annealed different times. □ is the average value and × is the minimum and maximum position. The three horizontal lines of each box stand for the 25%, 50% and 75% of the reading distribution. The whisker range is determined by the standard deviation of the nine devices per substrate.

The device with an absorber layer selenised for 20 minutes exhibits the highest overall efficiency of η = 5.41 %, with V_{oc} = 0.36 V, J_{sc} = 29.6 mA/cm^2, and *FF* =

50.7 %. In distinct contrast, the efficiency of the device with an absorber that was selenised for 40 minutes is only η = 1.90 %. As shown in Table 7.3, the reduced efficiency of this device arises not only from reductions in V_{oc} and J_{sc}, but also a large drop in *FF* caused by higher series resistance R_S and lower shunt resistance R_{SH}. Compared with the clean surface and smooth grains of other samples, small particles are dispersed on the absorber after a relatively long selenisation time as shown in Figure 7.14 and are likely to account for the degeneration in device performance. The reason for this is currently not well understood and needs further investigation. Inspection of the device parameter distributions summarised in Figure 7.13 shows that the relatively low efficiency of the 10 minutes annealed sample mainly arises from inferior J_{sc} compared with the 20 minutes annealed sample. Longer annealing time causes more selenium incorporation into the lattice and thicker, large-grained layers are developed, which account for more efficient absorption of the incident light.

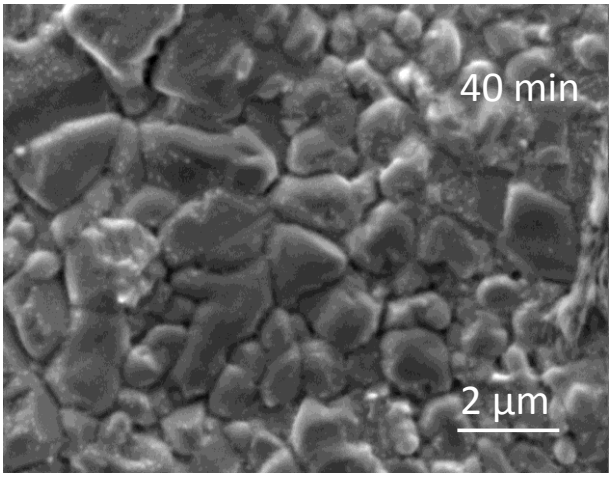

Figure 7.14 Top view SEM images CZTSSe thin film selenised at 500 ℃ for 40 minutes.

7.2.2 Influence of selenisation temperature

The influence of the selenisation temperature on the device performance was also considered. *J-V* curves of the best device at each selenisation temperature are shown in Figure 7.15 with the device parameters extracted from the *J-V* curves summarised in Table 7.4. The variations in device performance for all nine devices on each substrate are also shown in Figure 7.16.

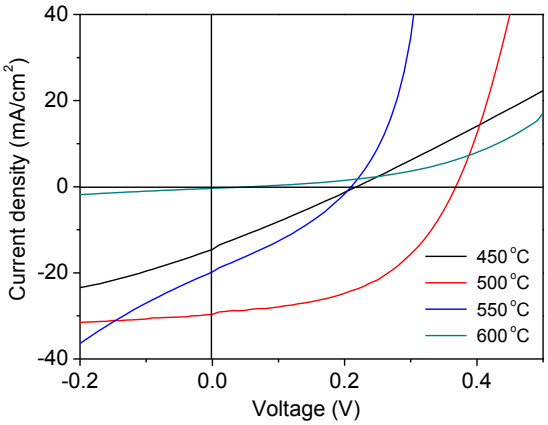

Figure 7.15 *J-V* curves of solar cells with CZTSSe thin film absorbers selenised at different temperatures for 20 minutes.

Table 7.4 Device parameters for the solar cells with *J-V* curves shown in Figure 7.15.

Device (℃)	η (%)	V_{OC} (V)	J_{SC} (mA/cm^2)	FF (%)	R_S (Ω·cm^2)	R_{SH} (Ω·cm^2)
450	0.82	0.21	14.6	26.9	13.9	17
500	5.41	0.36	29.6	50.7	3.1	77
550	1.32	0.21	19.8	31.8	5.5	14
600	0.22	0.05	1.5	28.5	137.6	156

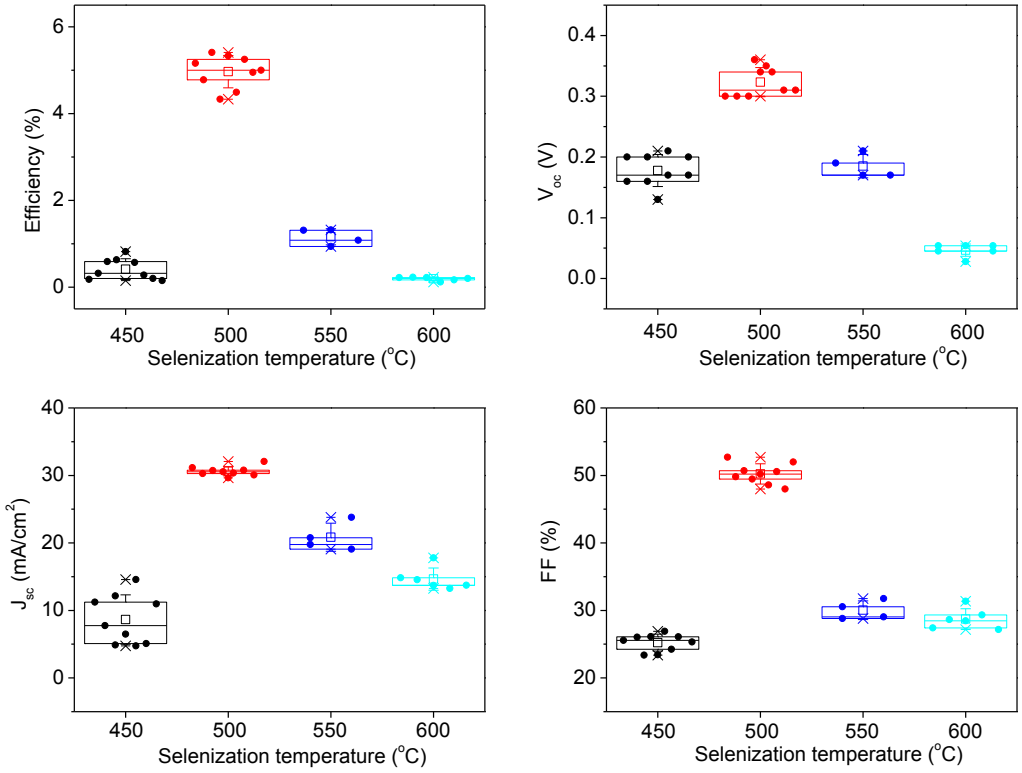

Figure 7.16 Performance distribution of solar cells fabricated using CZTSSe thin films annealed at different temperatures. □ is the average value and × is the minimum and maximum position. The three horizontal lines of each box stand for the 25%, 50% and 75% of the reading distribution. The whisker range is determined by the standard deviation of the nine readings.

The selenisation temperature plays an important role in determining the device performances due to its significant influence on the absorber morphology. For CZTS thin films selenised at low temperature, small and loosely packed grains are obtained as shown in Figure 7.5 (a). These thin films yield inferior devices with poor photovoltaic parameters which degrade the device efficiency to ~1.0 %. When the selenisaton temperature increases to 500 ℃, larger grains are obtained. Perhaps more importantly, the grains become densely packed and yield smooth and crack free thin

films (Figure 7.5(b)). From the cross-sectional views shown in Figure 7.5 (e-h), thicker large-grained layers and thinner fine-grained layers are developed at higher temperature. This is thought to improve the device performance by enhancing absorption of low energy photons and reducing parasitic resistance [80]. Using these thin films, devices with efficiencies of up to 5.41 % are achieved. However, for samples annealed at higher temperatures such as 550 ℃ and 600 ℃, the detrimental effects of holes on the surface of the absorber (as indicated by the arrows in Figure 7.5 (c-d)) can be observed as the device efficiency is reduced. Therefore, it is crucial to optimise the selenisation conditions to find the optimum balance between grain growth and thin film stability. Furthermore, compared with 550 ℃ the device with absorber annealed at, 600 ℃ exhibits even worse performance with almost no diode characteristic. A possible reason is a thicker $Mo(S,Se)_2$ interfacial layer is formed (as shown in Figure 7.5 (h)) and although thin $Mo(S,Se)_2$ interfacial layers are widely found in high efficiency solar cells [11, 16], too thick a layer will limit the device performance as a consequence of high resistivity and poor adhesion [84, 85].

7.2.3 Influence of selenium vapour pressure

The influence of the selenisation vapour pressure on the device performance was also considered. *J-V* curves of the best device at each selenisation vapour pressure are shown in Figure 7.17 with the device parameters extracted from the *J-V* curves summarised in Table 7.5. The variations in device performance for all nine devices on each substrate are also shown in Figure 7.18.

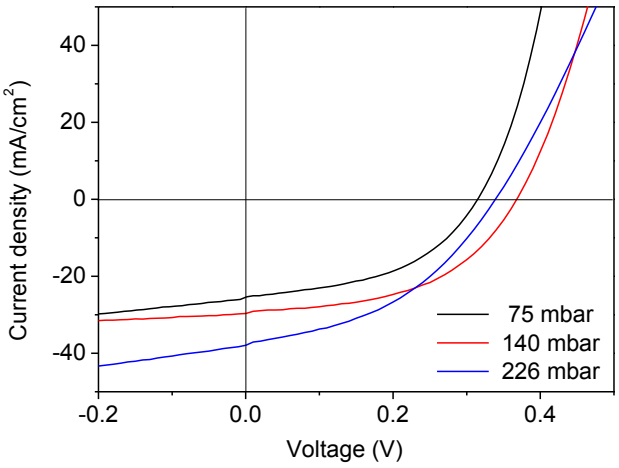

Figure 7.17 *J-V* curves of solar cells with CZTSSe thin film absorbers selenised at different vapour pressures.

Table 7.5 Device parameters for the solar cells with *J-V* curves shown in Figure 7.17. Also listed are energy bandgap determined from the EQE spectra (see Figure 7.17), selenium content calculated from XRD (See Figure 7.10), and V_{oc} deficit.

P_{Se} (mbar)	η (%)	V_{oc} (V)	J_{sc} (mA/cm^2)	FF (%)	R_S (Ω.cm^2)	R_{SH} (Ω.cm^2)	E_g (eV)	Se /(S+Se)	E_g-qV_{oc} (eV)
75	3.76	0.31	25.3	48.3	3.3	40	1.07	0.89	0.76
140	5.41	0.36	29.6	50.7	3.1	77	1.04	0.94	0.68
226	5.38	0.33	37.9	43.0	3.9	26	0.95	0.97	0.62

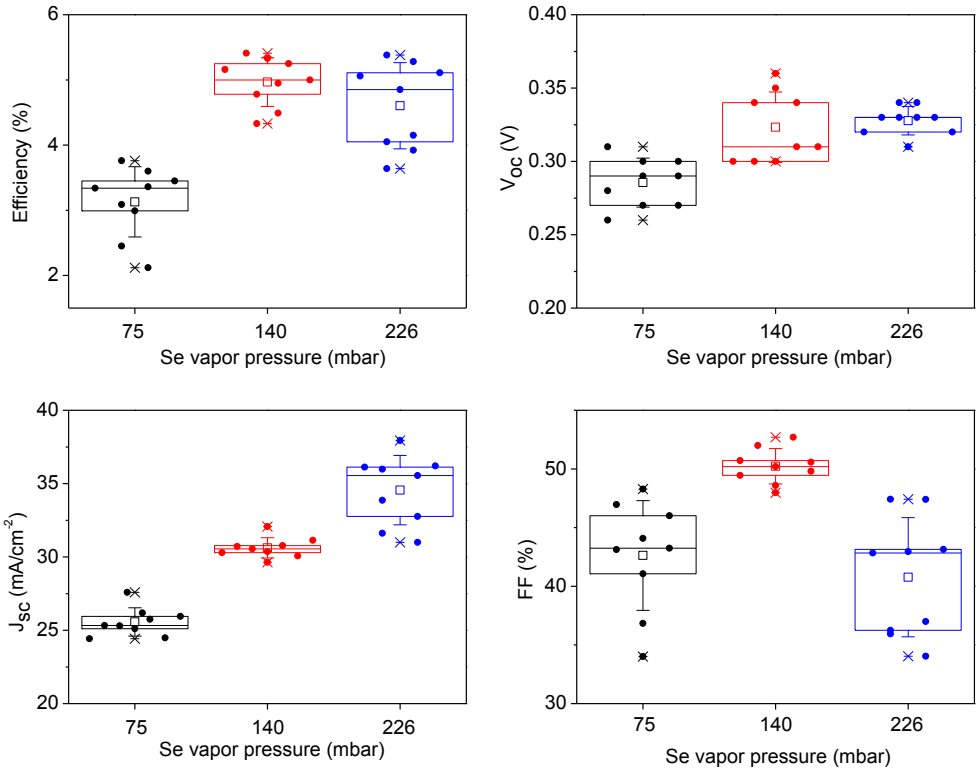

Figure 7.18 Performance distribution of solar cells fabricated using CZTSSe thin films selenised at different vapour pressures. □ is the average value and × is the minimum and maximum position. The three horizontal lines of each box stand for the 25%, 50% and 75% of the reading distribution. The whisker range is determined by the standard deviation of the nine readings.

From Figure 7.17, the absorber annealed under a selenium vapour pressure of 140 mbar yields a peak device efficiency of 5.41% with correspondingly higher V_{oc}, J_{sc} and FF. For low selenium vapour pressure at 75 mbar, inferior device efficiency of 3.76 % is observed. Comparing the cross-sectional images in Figure 7.11, the relatively thinner large-grained layer and thicker $Mo(S,Se)_2$ layer of the 75 mbar selenised sample may take account for the inferior V_{oc} and FF. For the device made from the absorber selenised under selenium vapor pressure of 226 mbar, a thicker

large-grained layer (~1.2 μm) in good crystallinity and a very thin $MoSe_2$ layer (~ 80 nm) are obtained. However, the V_{oc} and *FF* decrease against expectations. It therefore appears that the V_{oc} here may be affected by the thicker fine grain layer that high series resistances are introduced to limit the voltage available across to the device. The parasite resistance introduced by the thicker fine-grained layer degrades the *FF* obviously. Despite the decreasing of V_{oc} and *FF*, no notable reduction in efficiency is observed for this device. This is due to a significant gain in J_{sc} (38 mA/cm^2), which counterbalances the losses in *FF* and V_{oc}.

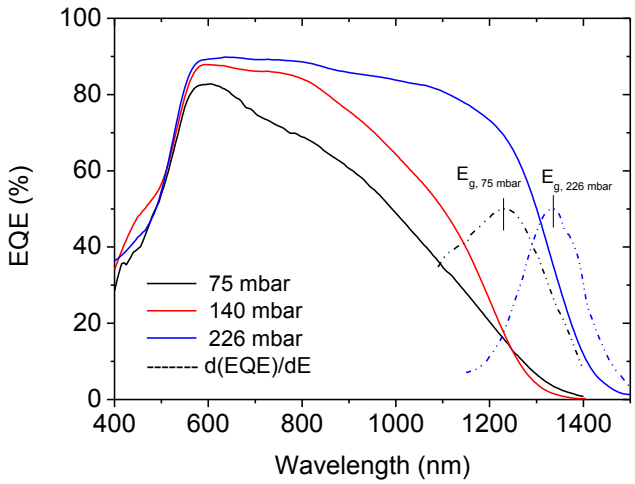

Figure 7.19 EQE spectra of solar cells fabricated using CZTSSe thin films selenised under different selenium vapour pressures.

In Figure 7.19, EQE measurements of the devices offer further insight into in the device performance. The devices show improved carrier collection efficiencies in the visible and near-infrared wavelength ranges when higher selenium vapour pressure is used in the selenisation process. A nearly ideal EQE shape is observed when

selenium vapour pressure is increased to 226 mbar and this device reveals a photocurrent efficiency of $>$ 85 % over the wavelength range 550 nm to 1050 nm. From the dark EQE spectrum, the maximum J_{sc} achievable for this device is calculated to be 39 mA/cm^2. Plotting d(EQE)/dE versus wavelength in Figure 7.19 shows that the CZTSSe bandgap decreases due to the increased selenium incorporation in the film with higher selenium vapour pressure as summarised in Table 7.5. The V_{oc} deficit is observed to be minimised as a result of the smaller energy bandgap E_g obtained under higher selenium vapour pressure. Although one would expect an increase in J_{sc} for lower energy bandgap values, the large improvement cannot solely explained by a reduction in E_g. As shown in Figure 7.11, thicker upper large grain layer annealed at higher selenium vapour pressure is likely to account for the improvement in the photocurrent.

7.3 Summary

High quality CZTSSe photovoltaic absorber layers were fabricated by selenising the as-deposited thin film made from CZTS nanoparticle inks. Selenisation time and temperature are found to significantly affect the morphology and composition of the thin film. Longer time, higher temperature and higher selenium vapour pressure result in larger CZTSSe grains and more selenium being incorporated into the lattice. The reaction of the CZTS selenisation process is found to be controlled by cation re-ordering and grain boundary migration (Avrami's model) rather than selenium incorporation (parabolic model). The CZTSSe grain growth follows normal grain

growth behaviour. It was found that an energy of 85.38 kJ/mol is needed to activate the CZTSSe boundary migration to consume the small grains and grow larger grains. A relatively moderate selenisation condition of 500 ℃ for 20 minutes under a 140 mbar selenium vapour pressure yields a peak device efficiency of 5.4 %. Furthermore, an ideal EQE "top hat" shape is observed for a selenium vapour pressure of 226 mbar and results in a significantly improved J_{sc}. The device performance is highly sensitive to the selenisation conditions, indicating that it is essential to find the correct balance between grain growth and thin film quality.

Chapter 8

Conclusions

8.1 Thesis summary

This thesis details CZTSSe thin film solar cells made from CZTS nanoparticle inks. In particular, three aspects of the fabrication have been investigated to study their effect on CZTSSe solar cell performance. These were (a) the controllable fabrication of CZTS nanoparticle inks, (b) the role of the nanoparticle inks in determining the device performance and (iii) the kinetics of the selenisation process used to convert thin films of CZTS nanoparticles to large grain CZTSSe photovoltaic absorbers.

In Chapter 5, CZTS nanoparticles were successfully synthesised by injection of precursors into a hot surfactant. The CZTS nanoparticles had an irregular spherical shape and were slightly polydispersed with most of the nanoparticles having diameters in the range 10-25 nm. A control sample composed of CZTS nanoparticles was prepared at 225 ℃ for 30 minutes and had a kesterite crystal structure. By controlling the precursor molar ratios in a Cu-poor and Zn-rich region of the phase diagram, the average composition of the CZTS nanoparticles was $Cu_{1.72\pm0.02}Zn_{1.13\pm0.02}Sn_{0.96\pm0.01}S_{4\pm0.06}$ with a Cu/(Sn+Zn) ratio of 0.83 and a Zn/Sn ratio of 1.18. The CZTS film was studied to have a high absorption coefficient (greater than 10^4 cm^{-1}) in the visible light region and the energy bandgap was estimated to be

1.51 eV from optical spectroscopy.

The influences of reaction temperature and time on the structural, compositional, and optical properties of CZTS nanoparticles were then systematically investigated. Temperature-dependent experiments revealed that higher temperature facilitated nanoparticle growth and resulted in larger CZTS nanoparticles. As the reaction temperature increased from 195 to 240 ℃, the nanoparticles became richer in zinc and poorer in tin. Wurtzite CZTS was formed at lower temperature whereas CTS was present at higher temperature. These factors were found to have a strong influence on the energy bandgap of nanoparticles.

Time-dependent experiments showed that the CZTS nanoparticles were more polydispersed as the reaction time increased which suggests the growth of the nanoparticles follows Ostwald ripening. Throughout the reaction, the CZTS nanoparticles maintained the kesterite structure and the composition of Sn composition remained constant at the stoichiometric ratio of 0.25. However, the composition of nanoparticles changed from Cu-rich and Zn-poor region at 15 minutes to being Cu-poor and Zn-rich when the reaction period was extended. Analysis of the experimental data indicates that it is crucial to optimise the reaction conditions to fabricate Cu_2ZnSnS_4 nanoparticles in a narrow composition region that is suitable for use in high efficient solar cell devices.

In Chapter 6, smooth and crack-free CZTS nanoparticle thin films were provided by

repeated spin-coating of nanoparticle inks on Mo-SLG substrate. Studied by SIMS, the constituent elements of the as-deposited CZTS nanoparticle thin film exhibited uniform distribution throughout the film thickness. Furthermore, a MoS_2 layer was formed between the CZTS layer and the Mo substrate during the soft-baking process. CZTSSe photovoltaic absorber layers were then fabricated by selenising the CZTS nanoparticle thin films. After selenisation, the resulting CZTSSe layer was composed of a densely packed large-grain CZTSSe layer and a carbon rich residual fine-grain sublayer. The composition of the thin film remained Cu-poor and Zinc-rich. Even in selenium-rich conditions, some residual sulphur was still present in the lattice. The selenised thin film therefore had a slightly shifted kesterite crystal structure compared with the pure CZTSe and the energy bandgap was estimated to be relatively higher at 1.10 eV. In addition to the absorber layer, a $Mo(S,Se)_2$ was formed on top of the Mo substrate. The resultant CZTSSe thin films were then fabricated into PV devices with a configuration of Mo/CZTSSe/CdS/i-ZnO/ITO/Ni-Al.

Three types of nanoparticle inks fabricated at different temperature, time and cooling mode were selected to fabricate the complete device. The device performance was found to depend critically upon the chemical reaction conditions used to synthesise the nanoparticles. Crucially, rapid thermal quenching of the reaction resulted in wurtzite CZTS atomic arrangement which was observed to be strongly detrimental to the device performance. Prolonging the reaction offers a new route to increasing the

concentration of acceptor levels in CZTSSe photovoltaic absorbers and resulted in higher device efficiency relative to a control device. The presence of CTS was found to correlate with increased efficiency and the apparent positive effects of this phase were also accompanied by an increase in the doping levels. The highest overall device efficiency was η = 6.26 %, and was based on a kesterite nanoparticle ink made using 255 ℃ for a reaction time of 30 minutes.

The selenisation process used to convert thin films of CZTS nanoparticles to thin films of composed of large grains suitable for light absorption, is another key step in the fabrication of PV devices. The results of a systemtic investigation of this process are detailed in Chapter 7. The kinetics of selenisation were analysed by studying variations of the thin film morphology and composition as a function of selenisation time, temperature and selenium vapour pressure. Longer time, higher temperature and higher selenium vapour pressure resulted in larger CZTSSe grains and more selenium being incorporated into the lattice. Furthermore, a longer selenisation period resulted in a thicker layer composed of large grains of CZTSSe. However, the selenisation rate was found to be time dependent and the CZTSSe grain growth reaction process therefore cannot be simply described by parabolic kinetics. Depending on the selenium conversion ratio, a Sharp-Hancock plot was fitted to yield an Avrami exponent and rate constant of 0.24 and 1.95 min^{-1}, respectively. Moreover, it was found that 50 % of the selenium conversion was completed in only 7 seconds. The relatively fast selenium incorporation indicated that the CZTSSe

grain growth was limited by cation re-ordering (Avrami's model) rather than selenium incorporation (parabolic model). However, longer annealing times were still required for the formation of large grains. The CZTSSe grain growth was found to follow normal grain growth behaviour and an energy of 85.38 kJ/mol was needed to activate the CZTSSe boundary migration to consume the small grains and grow larger grains.

CZTSSe thin films prepared at different selenisation times, temperatures and selenium vapour pressures were embedded into solar cells and their PV performances were compared. It was found that relatively moderate selenisation conditions of 500 ℃ for 20 minutes under a 140 mbar selenium vapour pressure yielded a peak device efficiency of 5.4 %. A small concentration of detrimental defects such as pinholes on the surface of the absorber and a thicker $Mo(S,Se)_2$ interfacial layer formed at relatively intense selenisation conditions account for the inferior device performance at high temperature. In addition, an ideal 'top hat' shape EQE characteristic was observed and J_{sc} had been significantly improved by 30 % for higher selenium vapour pressure of 226 mbar. The device performance is highly sensitive to the selenisation conditions, indicating that it is essential to find the correct balance between grain growth and thin film quality.

8.2 Suggestions for further work

Further to the work described in this thesis, a number of research challenges remain

and more research is required in order to further improve the device performance of CZTSSe solar cells.

Firstly, CZTS nanoparticle inks were prepared using a hot injection method, and in this work, long chain ligands were used to provide stable nanoparticle dispersions. Short chain ligands or even hydrophilic solvent systems could offer an alternative in an effect to minimise or avoid introducing carbon impurities into the completed films. In addition, one of the most difficult challenges in the nanoparticle synthesis may be to understand the mechanism by which metallic cations are incorporated into the growing nanoparticles.

Secondly, a bilayer structure composed of a large-grain CZTSSe layer on top and a thin fine-grain carbon rich CZTSSe layer at the interface with the substrate was generally observed. The role of the fine-grain layer in determining the device performance currently lacks understanding. More investigations of the selenisation process are required to minimising any negative effects of the fine-grain layer. This would help in understanding the effect of fine-grain layer that seems to limit the device performance. The ultimate success of this selenisation strategy will rely on the elimination of fine-grain layer while maximising of the effective large-grain layer.

Finally, the V_{oc} deficit is considered to be the main limitation for further efficiency increasing of the CZTSSe thin film solar cells. However, the selenisation

optimisation in this work provides an avenue to improve device performance by significantly increase the J_{sc}. Using a selenium vapour pressure of 226 mbar in the selenisation process, a highest J_{sc} of 38 mA/cm^2 is achieved among the CZTSSe solar cells that made from CZTS nanoparticle inks. The challenge is to further narrowing the V_{oc} deficit while preserving this increase in J_{sc}. If this can be achieved, this technique will stand as stiff competition for the widespread CZTSSe thin film solar cells due to the best mix of high device performance, material abundance and cost effectiveness.

References

[1] O. Morton, Solar energy: A new day dawning?: Silicon Valley sunrise, Nature, 443 (2006) 19-22.

[2] M.A. Green, K. Emery, Y. Hishikawa, W. Warta, E.D. Dunlop, Solar cell efficiency tables (version 44), Progress in Photovoltaics: Research and Applications, 22 (2014) 701-710.

[3] B.A. Andersson, Materials availability for large-scale thin-film photovoltaics, Progress in Photovoltaics: Research and Applications, 8 (2000) 61-76.

[4] H. Katagiri, K. Jimbo, W.S. Maw, K. Oishi, M. Yamazaki, H. Araki, A. Takeuchi, Development of CZTS-based thin film solar cells, Thin Solid Films, 517 (2009) 2455-2460.

[5] D.B. Mitzi, O. Gunawan, T.K. Todorov, K. Wang, S. Guha, The path towards a high-performance solution-processed kesterite solar cell, Solar Energy Materials and Solar Cells, 95 (2011) 1421-1436.

[6] K. Wang, O. Gunawan, T. Todorov, B. Shin, S.J. Chey, N.A. Bojarczuk, D. Mitzi, S. Guha, Thermally evaporated Cu_2ZnSnS_4 solar cells, Appl Phys Lett, 97 (2010) 143508.

[7] W. Yang, H.S. Duan, B. Bob, H. Zhou, B. Lei, C.H. Chung, S.H. Li, W.W. Hou, Y. Yang, Novel solution processing of high-efficiency earth-abundant $Cu_2ZnSn(S,Se)_4$ solar cells, Advanced Materials, 24 (2012) 6323-6329.

[8] B. Shin, O. Gunawan, Y. Zhu, N.A. Bojarczuk, S.J. Chey, S. Guha, Thin film solar cell with 8.4% power conversion efficiency using an earth-abundant Cu_2ZnSnS_4 absorber, Progress in Photovoltaics: Research and Applications, 21 (2013) 72-76.

[9] I. Repins, C. Beall, N. Vora, C. DeHart, D. Kuciauskas, P. Dippo, B. To, J. Mann, W.C. Hsu, A. Goodrich, R. Noufi, Co-evaporated $Cu_2ZnSnSe_4$ films and devices, Solar Energy Material Solar Cells, 101 (2012) 154-159.

[10] Q. Guo, G.M. Ford, W.C. Yang, B.C. Walker, E.A. Stach, H.W. Hillhouse, R. Agrawal, Fabrication of 7.2% efficient CZTSSe solar cells using CZTS nanocrystals, Journal of the American Chemical Society, 132 (2010) 17384-17386.

[11] Y. Cao, M.S. Denny, J.V. Caspar, W.E. Farneth, Q. Guo, A.S. Ionkin, L.K. Johnson, M. Lu, I. Malajovich, D. Radu, H.D. Rosenfeld, K.R. Choudhury, W. Wu, High-efficiency solution-processed $Cu_2ZnSn(S,Se)_4$ thin-film solar cells prepared from binary and ternary nanoparticles, Journal of the American Chemical Society, 134 (2012) 15644-15647.

[12] Q. Guo, J.V. Caspar, K.E. Roelofs, S. Subramoney, H.D. Rosenfeld, Formation of Cu-rich and Sn-poor CZTSSe via $Cu_3Sn(S,Se)_4$-ZnS solid-solution as the intermediate, Chemistry of Materials, 26 (2014) 5664-5674.

[13] T.K. Todorov, K.B. Reuter, D.B. Mitzi, High-Efficiency Solar Cell with Earth-Abundant Liquid-Processed Absorber, Advanced Materials, 22 (2010) E156-E159.

[14] T.K. Todorov, J. Tang, S. Bag, O. Gunawan, T. Gokmen, Y. Zhu, D.B. Mitzi, Beyond 11% efficiency: characteristics of state-of-the-art $Cu_2ZnSn(S,Se)_4$ Solar Cells, Advanced Energy Materials, 3 (2013) 34-38.

[15] W. Wang, M.T. Winkler, O. Gunawan, T. Gokmen, T.K. Todorov, Y. Zhu, D.B. Mitzi, Device characteristics of CZTSSe thin-film solar cells with 12.6% efficiency, Advanced Energy Materials, 4 (2014) 1301465.

[16] C.K. Miskin, W.C. Yang, C.J. Hages, N.J. Carter, C.S. Joglekar, E.A. Stach, R. Agrawal, 9.0% efficient $Cu_2ZnSn(S,Se)_4$ solar cells from selenized nanoparticle inks, Progress in Photovoltaics: Research and Applications, 23 (2015) 654-659.

[17] W. Shockley, H.J. Queisser, Detailed Balance Limit of Efficiency of p-n junction solar sells, J. Appl. Phys., 32 (1961) 10.

[18] C. Kittel, Introduction to solid state physics, 8th ed., Wiley, New York, 2005.

[19] C. Hu, White, R. M., Solar cells: from basics to advanced systems, McGraw-Hill, New York, 1983.

[20] R.W. Miles, G. Zoppi, I. Forbes, Inorganic photovoltaic cells, Materials Today, 10 (2007) 20-27.

[21] R.v. Overstraeten, Mertens, R. P., Physics, technology and use of photovoltaics, Adam Hilger Ltd, Bristol and Boston, 1986.

[22] S.M. Sze, Semiconductor Devices: Physics and Technology., 2nd ed., Wiley, New York, 2001.

[23] E. Burstein, Anomalous Optical Absorption Limit in InSb, Physical Review, 93

(1954) 632-633.

[24] R. Aninat, Study of Cu(In,Al)Se_2 thin films prepared by selenisation of sputtered metallic precursors for application in solar cells, in, Northumbria Univeristy, 2012.

[25] Z. Guillaume, Studies of CdTe thin films and solar cells grown by MOCVD, in, Durham University, 2005.

[26] S.S. Hegedus, W.N. Shafarman, Thin-film solar cells: device measurements and analysis, Progress in Photovoltaics: Research and Applications, 12 (2004) 155-176.

[27] R.W. Miles, K.M. Hynes, I. Forbes, Photovoltaic solar cells: An overview of state-of-the-art cell development and environmental issues, Progress in Crystal Growth and Characterization of Materials, 51 (2005) 1-42.

[28] M.T. Winkler, W. Wang, O. Gunawan, H.J. Hovel, T.K. Todorov, D.B. Mitzi, Optical designs that improve the efficiency of $Cu_2ZnSn(S,Se)_4$ solar cells, Energy Environ. Sci., 7 (2014) 1029-1036.

[29] M.A. Green, Solar cells-operating principles, technology and system application, Prentice-Hall, Kensington, 1992.

[30] R. Nitsche, D.F. Sargent, P. Wild, Crystal growth of quaternary 1_2246_4 chalcogenides by iodine vapor transport, Journal of Crystal Growth, 1 (1967) 52-53.

[31] D. Brandon, Kaplan, W. D. , Microstructural characterization of materials, John Wiley & Sons, Ltd, Chichester, 1999.

[32] J. Paier, R. Asahi, A. Nagoya, G. Kresse, Cu_2ZnSnS_4 as a potential photovoltaic

material: A hybrid Hartree-Fock density functional theory study, Physical Review B, 79 (2009) 115126.

[33] X. Lu, Z. Zhuang, Q. Peng, Y. Li, Wurtzite Cu_2ZnSnS_4 nanocrystals: a novel quaternary semiconductor, Chemical Communications, 47 (2011) 3141-3143.

[34] S. Chen, X.G. Gong, A. Walsh, S.-H. Wei, Crystal and electronic band structure of Cu_2ZnSnX_4 (X=S and Se) photovoltaic absorbers: First-principles insights, Appl Phys Lett, 94 (2009) 041903.

[35] S. Chen, X.G. Gong, A. Walsh, S.-H. Wei, Electronic structure and stability of quaternary chalcogenide semiconductors derived from cation cross-substitution of II-VI and I-III-VI_2 compounds, Physical Review B, 79 (2009) 165211.

[36] S. Siebentritt, S. Schorr, Kesterites-a challenging material for solar cells, Progress in Photovoltaics: Research and Applications, 20 (2012) 512-519.

[37] S. Schorr, The crystal structure of kesterite type compounds: A neutron and X-ray diffraction study, Solar Energy Materials and Solar Cells, 95 (2011) 1482-1488.

[38] B.G. Mendis, M.D. Shannon, M.C.J. Goodman, J.D. Major, R. Claridge, D.P. Halliday, K. Durose, Direct observation of Cu, Zn cation disorder in Cu_2ZnSnS_4 solar cell absorber material using aberration corrected scanning transmission electron microscopy, Progress in Photovoltaics: Research and Applications, 22 (2014) 24-34.

[39] A. Shavel, J. Arbiol, A. Cabot, Synthesis of quaternary chalcogenide nanocrystals: stannite $Cu_2Zn_xSn_ySe_{1+x+2y}$, Journal of the American Chemical Society,

132 (2010) 4514-4515.

[40] M. Li, W.H. Zhou, J. Guo, Y.L. Zhou, Z.L. Hou, J. Jiao, Z.J. Zhou, Z.L. Du, S.X. Wu, Synthesis of pure metastable wurtzite CZTS nanocrystals by facile one-pot method, The Journal of Physical Chemistry C, 116 (2012) 26507-26516.

[41] S. Chen, A. Walsh, Y. Luo, J.H. Yang, X.G. Gong, S.H. Wei, Wurtzite-derived polytypes of kesterite and stannite quaternary chalcogenide semiconductors, Physical Review B, 82 (2010) 195203.

[42] S. Chen, X.G. Gong, S.H. Wei, Band-structure anomalies of the chalcopyrite semiconductors $CuGaX_2$ versus $AgGaX_2$ (X=S and Se) and their alloys, Physical Review B, 75 (2007) 205209.

[43] K. Jimbo, R. Kimura, T. Kamimura, S. Yamada, W.S. Maw, H. Araki, K. Oishi, H. Katagiri, Cu_2ZnSnS_4-type thin film solar cells using abundant materials, Thin Solid Films, 515 (2007) 5997-5999.

[44] H. Katagiri, K. Saitoh, T. Washio, H. Shinohara, T. Kurumadani, S. Miyajima, Development of thin film solar cell based on Cu_2ZnSnS_4 thin films, Solar Energy Materials and Solar Cells, 65 (2001) 141-148.

[45] D.P. Halliday, R. Claridge, M.C.J. Goodman, B.G. Mendis, K. Durose, J.D. Major, Luminescence of Cu_2ZnSnS_4 polycrystals described by the fluctuating potential model, J. Appl. Phys., 113 (2013) 223503.

[46] J.P. Leitão, N.M. Santos, P.A. Fernandes, P.M.P. Salomé, A.F. da Cunha, J.C. González, G.M. Ribeiro, F.M. Matinaga, Photoluminescence and electrical study of

fluctuating potentials in Cu_2ZnSnS_4-based thin films, Physical Review B, 84 (2011) 024120.

[47] A. Nagoya, R. Asahi, R. Wahl, G. Kresse, Defect formation and phase stability of Cu_2ZnSnS_4 photovoltaic material, Physical Review B, 81 (2010) 113202.

[48] S. Chen, X.G. Gong, A. Walsh, S.H. Wei, Defect physics of the kesterite thin-film solar cell absorber Cu_2ZnSnS_4, Appl Phys Lett, 96 (2010) 021902.

[49] S. Chen, J.H. Yang, X.G. Gong, A. Walsh, S.H. Wei, Intrinsic point defects and complexes in the quaternary kesterite semiconductor Cu_2ZnSnS_4, Physical Review B, 81 (2010) 245204.

[50] T. Maeda, S. Nakamura, T. Wada, First-principles calculations of vacancy formation in In-free photovoltaic semiconductor $Cu_2ZnSnSe_4$, Thin Solid Films, 519 (2011) 7513-7516.

[51] A. Walsh, S. Chen, S.H. Wei, X.G. Gong, Kesterite thin-film solar cells: advances in materials modelling of Cu_2ZnSnS_4, Advanced Energy Materials, 2 (2012) 400-409.

[52] O. Lundberg, M. Edoff, L. Stolt, The effect of Ga-grading in CIGS thin film solar cells, Thin Solid Films, 480-481 (2005) 520-525.

[53] S. Jung, S. Ahn, J.H. Yun, J. Gwak, D. Kim, K. Yoon, Effects of Ga contents on properties of CIGS thin films and solar cells fabricated by co-evaporation technique, Current Applied Physics, 10 (2010) 990-996.

[54] K. Sakurai, R. Scheer, S. Nakamura, Y. Kimura, T. Baba, C.A. Kaufmann, A.

Neisser, S. Ishizuka, A. Yamada, K. Matsubara, K. Iwata, P. Fons, H. Nakanishi, S. Niki, Structural changes of CIGS during deposition investigated by spectroscopic light scattering: A study on Ga concentration and Se pressure, Solar Energy Materials and Solar Cells, 90 (2006) 3377-3384.

[55] E. Dilena, Y. Xie, R. Brescia, M. Prato, L. Maserati, R. Krahne, A. Paolella, G. Bertoni, M. Povia, I. Moreels, L. Manna, $CuIn_xGa_{1-x}S_2$ nanocrystals with tunable composition and band gap synthesized via a phosphine-free and scalable procedure, Chemistry of Materials, 25 (2013) 3180-3187.

[56] M.I. Alonso, M. Garriga, C.A. Durante Rincón, E. Hernández, M. León, Optical functions of chalcopyrite $CuGa_xIn_{1-x}Se_2$ alloys, Appl Phys A, 74 (2002) 659-664.

[57] S. Kang, R. Sharma, J.K. Sim, C.R. Lee, Band gap engineering of tandem structured CIGS compound absorption layer fabricated by sputtering and selenization, Journal of Alloys and Compounds, 563 (2013) 207-215.

[58] G.M. Ford, Q.J. Guo, R. Agrawal, H.W. Hillhouse, Earth abundant element $Cu_2Zn(Sn_{1-x}Ge_x)S_4$ nanocrystals for tunable band gap solar cells: 6.8% efficient device fabrication, Chemistry of Materials, 23 (2011) 2626-2629.

[59] C. Persson, Electronic and optical properties of Cu_2ZnSnS_4 and $Cu_2ZnSnSe_4$, J. Appl. Phys., 107 (2010) 053710.

[60] A. Khare, A.W. Wills, L.M. Ammerman, D.J. Norris, E.S. Aydil, Size control and quantum confinement in Cu_2ZnSnS_4 nanocrystals, Chemical Communications, 47 (2011) 11721-11723.

[61] R. Haight, A. Barkhouse, O. Gunawan, B. Shin, M. Copel, M. Hopstaken, D.B. Mitzi, Band alignment at the $Cu_2ZnSn(S_xSe_{1-x})_4$/CdS interface, Appl Phys Lett, 98 (2011) 253502.

[62] H. Wei, Z. Ye, M. Li, Y. Su, Z. Yang, Y. Zhang, Tunable band gap $Cu_2ZnSnS_{4x}Se_{4(1-x)}$ nanocrystals: experimental and first-principles calculations, CrystEngComm, 13 (2011) 2222-2226.

[63] K. Woo, Y. Kim, W. Yang, K. Kim, I. Kim, Y. Oh, J.Y. Kim, J. Moon, Band-gap-graded $Cu_2ZnSn(S_{1-x},Se_x)_4$ solar cells gabricated by an ethanol-based, particulate precursor ink route, Scientific Reports, 3 (2013) 3069.

[64] S. Chen, A. Walsh, J.H. Yang, X.G. Gong, L. Sun, P.-X. Yang, J.H. Chu, S.H. Wei, Compositional dependence of structural and electronic properties of $Cu_2ZnSn(S,Se)_4$ alloys for thin film solar cells, Physical Review B, 83 (2011) 125201.

[65] S.C. Riha, B.A. Parkinson, A.L. Prieto, Compositionally tunable $Cu_2ZnSn(S_{1-x}Se_x)_4$ nanocrystals: probing the effect of Se-inclusion in mixed chalcogenide thin films, Journal of the American Chemical Society, 133 (2011) 15272-15275.

[66] F.J. Fan, L. Wu, M. Gong, G. Liu, Y.X. Wang, S.H. Yu, S. Chen, L.W. Wang, X.G. Gong, Composition- and band-gap-tunable synthesis of wurtzite-derived $Cu_2ZnSn(S_{1-x}Se_x)_4$ nanocrystals: theoretical and experimental insights, ACS nano, 7 (2013) 1454-1463.

[67] S. Ahn, S. Jung, J. Gwak, A. Cho, K. Shin, K. Yoon, D. Park, H. Cheong, J.H. Yun, Determination of band gap energy (E_g) of $Cu_2ZnSnSe_4$ thin films: On the discrepancies of reported band gap values, Appl Phys Lett, 97 (2010) 021905.

[68] S.B. Zhang, S.H. Wei, A. Zunger, A phenomenological model for systematization and prediction of doping limits in II–VI and I–III–VI_2 compounds, J. Appl. Phys., 83 (1998) 3192-3196.

[69] I.D. Olekseyuk, I.V. Dudchak, L.V. Piskach, Phase equilibria in the Cu_2S-ZnS-SnS_2 system, Journal of Alloys and Compounds, 368 (2004) 135-143.

[70] J.J. Scragg, P.J. Dale, L.M. Peter, G. Zoppi, I. Forbes, New routes to sustainable photovoltaics: evaluation of Cu2ZnSnS4 as an alternative absorber material, physica status solidi (b), 245 (2008) 1772-1778.

[71] T. Todorov, M. Kita, J. Carda, P. Escribano, Cu_2ZnSnS_4 films deposited by a soft-chemistry method, Thin Solid Films, 517 (2009) 2541-2544.

[72] A. Weber, R. Mainz, H.W. Schock, On the Sn loss from thin films of the material system Cu-Zn-Sn-S in high vacuum, J. Appl. Phys., 107 (2010) 013516.

[73] J.J. Scragg, J.T. Wätjen, M. Edoff, T. Ericson, T. Kubart, C. Platzer-Björkman, A detrimental reaction at the molybdenum back contact in $Cu_2ZnSn(S,Se)_4$ thin-film solar cells, Journal of the American Chemical Society, 134 (2012) 19330-19333.

[74] S.C. Riha, B.A. Parkinson, A.L. Prieto, Solution-based synthesis and characterization of Cu_2ZnSnS_4 nanocrystals, Journal of the American Chemical Society, 131 (2009) 12054-12055.

[75] X.Y. Wang, Z.C. Sun, C. Shao, D.M. Boye, J.L. Zhao, A facile and general approach to polynary semiconductor nanocrystals via a modified two-phase method, Nanotechnology, 22 (2011) 245605.

[76] K. Wang, B. Shin, K.B. Reuter, T. Todorov, D.B. Mitzi, S. Guha, Structural and elemental characterization of high efficiency Cu_2ZnSnS_4 solar cells, Appl Phys Lett, 98 (2011) 051912-051913.

[77] X. Fontané, L. Calvo-Barrio, V. Izquierdo-Roca, E. Saucedo, A. Pérez-Rodriguez, J.R. Morante, D.M. Berg, P.J. Dale, S. Siebentritt, In-depth resolved Raman scattering analysis for the identification of secondary phases: characterization of Cu_2ZnSnS_4 layers for solar cell applications, Appl Phys Lett, 98 (2011) 181905-181903.

[78] J.M.R. Tan, Y.H. Lee, S. Pedireddy, T. Baikie, X.Y. Ling, L.H. Wong, Understanding the synthetic pathway of a single-phase quarternary semiconductor using surface-enhanced Raman scattering: a case of wurtzite Cu_2ZnSnS_4 nanoparticles, Journal of the American Chemical Society, 136 (2014) 6684-6692.

[79] A. Redinger, K. Hönes, X. Fontané, V. Izquierdo-Roca, E. Saucedo, N. Valle, A. Pérez-Rodríguez, S. Siebentritt, Detection of a ZnSe secondary phase in coevaporated $Cu_2ZnSnSe_4$ thin films, Appl Phys Lett, 98 (2011) 101907.

[80] J. van Embden, A.S.R. Chesman, E. Della Gaspera, N.W. Duffy, S.E. Watkins, J.J. Jasieniak, $Cu_2ZnSnS_{4x}Se_{4(1-x)}$ solar cells from polar nanocrystal inks, Journal of the American Chemical Society, 136 (2014) 5237-5240.

[81] Q. Tian, G. Wang, W. Zhao, Y. Chen, Y. Yang, L. Huang, D. Pan, Versatile and low-toxic solution approach to binary, ternary, and quaternary metal sulfide thin films and its application in $Cu_2ZnSn(S,Se)_4$ solar cells, Chemistry of Materials, 26 (2014) 3098-3103.

[82] W.C. Yang, C.K. Miskin, C.J. Hages, E.C. Hanley, C. Handwerker, E.A. Stach, R. Agrawal, Kesterite $Cu_2ZnSn(S,Se)_4$ absorbers converted from metastable, wurtzite-derived Cu_2ZnSnS_4 nanoparticles, Chemistry of Materials, 26 (2014) 3530-3534.

[83] U. Rau, H.W. Schock, Electronic properties of $Cu(In,Ga)Se_2$ heterojunction solar cells-recent achievements, current understanding, and future challenges, Appl Phys A, 69 (1999) 131-147.

[84] B. Shin, Y. Zhu, N.A. Bojarczuk, S. Jay Chey, S. Guha, Control of an interfacial $MoSe_2$ layer in $Cu_2ZnSnSe_4$ thin film solar cells: 8.9% power conversion efficiency with a TiN diffusion barrier, Appl Phys Lett, 101 (2012) 053903.

[85] X. Zhu, Z. Zhou, Y. Wang, L. Zhang, A. Li, F. Huang, Determining factor of $MoSe_2$ formation in $Cu(In,Ga)Se_2$ solar Cells, Solar Energy Materials and Solar Cells, 101 (2012) 57-61.

[86] H. Katagiri, Cu_2ZnSnS_4 thin film solar cells, Thin Solid Films, 480-481 (2005) 426-432.

[87] G. Zoppi, I. Forbes, R.W. Miles, P.J. Dale, J.J. Scragg, L.M. Peter, $Cu_2ZnSnSe_4$ thin film solar cells produced by selenisation of magnetron sputtered precursors,

Progress in Photovoltaics: Research and Applications, 17 (2009) 315-319.

[88] R.A. Wibowo, W.S. Kim, E.S. Lee, B. Munir, K.H. Kim, Single step preparation of quaternary thin films by RF magnetron sputtering from binary chalcogenide targets, Journal of Physics and Chemistry of Solids, 68 (2007) 1908-1913.

[89] H. Katagiri, K. Jimbo, S. Yamada, T. Kamimura, W.S. Maw, T. Fukano, T. Ito, T. Motohiro, Enhanced conversion efficiencies of Cu_2ZnSnS_4-based thin film solar cells by using preferential etching technique, Appl. Phys. Express, 1 (2008) 041201.

[90] T. Tanaka, A. Yoshida, D. Saiki, K. Saito, Q. Guo, M. Nishio, T. Yamaguchi, Influence of composition ratio on properties of Cu_2ZnSnS_4 thin films fabricated by co-evaporation, Thin Solid Films, 518 (2010) S29-S33.

[91] O. Volobujeva, J. Raudoja, E. Mellikov, M. Grossberg, S. Bereznev, R. Traksmaa, $Cu_2ZnSnSe_4$ films by selenization of Sn-Zn-Cu sequential films, Journal of Physics and Chemistry of Solids, 70 (2009) 567-570.

[92] H. Katagiri, N. Sasaguchi, S. Hando, S. Hoshino, J. Ohashi, T. Yokota, Preparation and evaluation of Cu_2ZnSnS_4 thin films by sulfurization of E-B evaporated precursors, Solar Energy Materials and Solar Cells, 49 (1997) 407-414.

[93] A.V. Moholkar, S.S. Shinde, A.R. Babar, K.-U. Sim, H.K. Lee, K.Y. Rajpure, P.S. Patil, C.H. Bhosale, J.H. Kim, Synthesis and characterization of Cu_2ZnSnS_4 thin films grown by PLD: solar cells, Journal of Alloys and Compounds, 509 (2011) 7439-7446.

[94] J.J. Scragg, D.M. Berg, P.J. Dale, A 3.2% efficient Kesterite device from

electrodeposited stacked elemental layers, Journal of Electroanalytical Chemistry, 646 (2010) 52-59.

[95] J.J. Scragg, P.J. Dale, L.M. Peter, Synthesis and characterization of Cu_2ZnSnS_4 absorber layers by an electrodeposition-annealing route, Thin Solid Films, 517 (2009) 2481-2484.

[96] S. Ahmed, K.B. Reuter, O. Gunawan, L. Guo, L.T. Romankiw, H. Deligianni, A high efficiency electrodeposited Cu_2ZnSnS_4 solar cell, Advanced Energy Materials, 2 (2012) 253-259.

[97] A. Ennaoui, M. Lux-Steiner, A. Weber, D. Abou-Ras, I. Kötschau, H.W. Schock, R. Schurr, A. Hölzing, S. Jost, R. Hock, T. Voß, J. Schulze, A. Kirbs, Cu_2ZnSnS_4 thin film solar cells from electroplated precursors: novel low-cost perspective, Thin Solid Films, 517 (2009) 2511-2514.

[98] N. Kamoun, H. Bouzouita, B. Rezig, Fabrication and characterization of Cu_2ZnSnS_4 thin films deposited by spray pyrolysis technique, Thin Solid Films, 515 (2007) 5949-5952.

[99] Y.B.K. Kumar, P.U. Bhaskar, G.S. Babu, V.S. Raja, Effect of copper salt and thiourea concentrations on the formation of Cu_2ZnSnS_4 thin films by spray pyrolysis, physica status solidi (a), 207 (2010) 149-156.

[100] N. Moritake, Y. Fukui, M. Oonuki, K. Tanaka, H. Uchiki, Preparation of Cu_2ZnSnS_4 thin film solar cells under non-vacuum condition, physica status solidi (c), 6 (2009) 1233-1236.

[101] K. Tanaka, M. Oonuki, N. Moritake, H. Uchiki, thin film solar cells prepared by non-vacuum processing, Solar Energy Materials and Solar Cells, 93 (2009) 583-587.

[102] K. Maeda, K. Tanaka, Y. Fukui, H. Uchiki, Influence of H_2S concentration on the properties of Cu_2ZnSnS_4 thin films and solar cells prepared by sol-gel sulfurization, Solar Energy Materials and Solar Cells, 95 (2011) 2855-2860.

[103] W. Yang, H.S. Duan, K.C. Cha, C.J. Hsu, W.C. Hsu, H. Zhou, B. Bob, Y. Yang, Molecular solution approach to synthesize electronic quality Cu_2ZnSnS_4 thin films, Journal of the American Chemical Society, 135 (2013) 6915-6920.

[104] J.W. Cho, A. Ismail, S.J. Park, W. Kim, S. Yoon, B.K. Min, Synthesis of Cu_2ZnSnS_4 thin films by a precursor solution paste for thin film solar cell applications, ACS applied materials & interfaces, 5 (2013) 4162-4165.

[105] S.G. Haass, M. Diethelm, M. Werner, B. Bissig, Y.E. Romanyuk, A.N. Tiwari, 11.2% Efficient Solution Processed Kesterite Solar Cell with a Low Voltage Deficit, Advanced Energy Materials, 5 (2015) n/a-n/a.

[106] Y.F. Du, J.Q. Fan, W.H. Zhou, Z.J. Zhou, J. Jiao, S.X. Wu, One-step synthesis of stoichiometric $Cu_2ZnSnSe_4$ as counter electrode for dye-sensitized solar cells, ACS applied materials & interfaces, 4 (2012) 1796-1802.

[107] J. Xu, X. Yang, Q.D. Yang, T.L. Wong, C.S. Lee, Cu_2ZnSnS_4 hierarchical microspheres as an effective counter electrode material for quantum dot sensitized solar cells, The Journal of Physical Chemistry C, 116 (2012) 19718-19723.

[108] H. Yang, L.A. Jauregui, G. Zhang, Y.P. Chen, Y. Wu, Nontoxic and abundant copper zinc tin sulfide nanocrystals for potential high-temperature thermoelectric energy harvesting, Nano letters, 12 (2012) 540-545.

[109] Q.J. Guo, H.W. Hillhouse, R. Agrawal, Synthesis of Cu_2ZnSnS_4 nanocrystal ink and its use for solar cells, Journal of the American Chemical Society, 131 (2009) 11672-11673.

[110] A. Carrete, A. Shavel, X. Fontané, J. Montserrat, J. Fan, M. Ibáñez, E. Saucedo, A. Pérez-Rodríguez, A. Cabot, Antimony-based ligand exchange to promote crystallization in spray-deposited $Cu_2ZnSnSe_4$ solar cells, Journal of the American Chemical Society, 135 (2013) 15982-15985.

[111] C. Steinhagen, M.G. Panthani, V. Akhavan, B. Goodfellow, B. Koo, B.A. Korgel, Synthesis of Cu_2ZnSnS_4 nanocrystals for use in low-cost photovoltaics, Journal of the American Chemical Society, 131 (2009) 12554-12555.

[112] S.C. Riha, S.J. Fredrick, J.B. Sambur, Y. Liu, A.L. Prieto, B.A. Parkinson, Photoelectrochemical characterization of nanocrystalline thin-film Cu_2ZnSnS_4 photocathodes, ACS applied materials & interfaces, 3 (2011) 58-66.

[113] Q.J. Guo, G.M. Ford, W.C. Yang, C.J. Hages, H.W. Hillhouse, R. Agrawal, Enhancing the performance of CZTSSe solar cells with Ge alloying, Solar Energy Materials and Solar Cells, 105 (2012) 132-136.

[114] J. Zhong, Z. Xia, C. Zhang, B. Li, X. Liu, Y.-B. Cheng, J. Tang, One-pot synthesis of self-stabilized aqueous nanoinks for $Cu_2ZnSn(S,Se)_4$ Solar Cells,

Chemistry of Materials, 26 (2014) 3573-3578.

[115] Y.L. Zhou, W.H. Zhou, M. Li, Y.F. Du, S.X. Wu, Hierarchical Cu_2ZnSnS_4 particles for a low-cost solar cell: morphology control and growth mechanism, The Journal of Physical Chemistry C, 115 (2011) 19632-19639.

[116] Q. Tian, X. Xu, L. Han, M. Tang, R. Zou, Z. Chen, M. Yu, J. Yang, J. Hu, Hydrophilic Cu_2ZnSnS_4 nanocrystals for printing flexible, low-cost and environmentally friendly solar cells, CrystEngComm, 14 (2012) 3847-3850.

[117] W. Xie, X. Jiang, C. Zou, D. Li, J. Zhang, J. Quan, L. Shao, Synthesis of highly dispersed Cu_2ZnSnS_4 nanoparticles by solvothermal method for photovoltaic application, Physica E: Low-dimensional Systems and Nanostructures, 45 (2012) 16-20.

[118] J. Joo, H.B. Na, T. Yu, J.H. Yu, Y.W. Kim, F. Wu, J.Z. Zhang, T. Hyeon, Generalized and facile synthesis of semiconducting metal sulfide nanocrystals, Journal of the American Chemical Society, 125 (2003) 11100-11105.

[119] M.G. Panthani, V. Akhavan, B. Goodfellow, J.P. Schmidtke, L. Dunn, A. Dodabalapur, P.F. Barbara, B.A. Korgel, Synthesis of $CuInS_2$, $CuInSe_2$, and $Cu(In_xGa_{1-x})Se_2$ (CIGS) nanocrystal "inks" for printable photovoltaics, Journal of the American Chemical Society, 130 (2008) 16770-16777.

[120] S. Mourdikoudis, L.M. Liz-Marzán, Oleylamine in nanoparticle synthesis, Chemistry of Materials, 25 (2013) 1465-1476.

[121] M. Chen, Y.G. Feng, X. Wang, T.C. Li, J.Y. Zhang, D.J. Qian, Silver

nanoparticles capped by oleylamine: formation, growth, and self-organization, Langmuir : the ACS journal of surfaces and colloids, 23 (2007) 5296-5304.

[122] A. Singh, H. Geaney, F. Laffir, K.M. Ryan, Colloidal synthesis of wurtzite Cu_2ZnSnS_4 nanorods and their perpendicular assembly, Journal of the American Chemical Society, 134 (2012) 2910-2913.

[123] G.M. Ford, Q.J. Guo, R. Agrawal, H.W. Hillhouse, $CuIn(S,Se)_2$ thin film solar cells from nanocrystal inks: effect of nanocrystal precursors, Thin Solid Films, 520 (2011) 523-528.

[124] Q. Guo, G.M. Ford, R. Agrawal, H.W. Hillhouse, Ink formulation and low-temperature incorporation of sodium to yield 12% efficient $Cu(In,Ga)(S,Se)_2$ solar cells from sulfide nanocrystal inks, Progress in Photovoltaics: Research and Applications, 21 (2013) 64-71.

[125] H.C. Leidholm C. , Breeze A. , Sunderland C. , Ki W. , and Zehnder D. , Final Report: Sintered CZTS Nanoparticle Solar Cells on Metal Foil, in, 2012.

[126] W. Wu, Y. Cao, J.V. Caspar, Q. Guo, L.K. Johnson, I. Malajovich, H.D. Rosenfeld, K.R. Choudhury, Studies of the fine-grain sub-layer in the printed CZTSSe photovoltaic devices, Journal of Materials Chemistry C, 2 (2014) 3777-3781.

[127] P.A. Fernandes, P.M.P. Salomé, A.F. da Cunha, Study of polycrystalline Cu_2ZnSnS_4 films by Raman scattering, Journal of Alloys and Compounds, 509 (2011) 7600-7606.

[128] Y. Zou, X. Su, J. Jiang, Phase-controlled synthesis of Cu_2ZnSnS_4 nanocrystals: the role of reactivity between Zn and S, Journal of the American Chemical Society, 135 (2013) 18377-18384.

[129] S. Suehiro, K. Horita, K. Kumamoto, M. Yuasa, T. Tanaka, K. Fujita, K. Shimanoe, T. Kida, Solution-processed Cu_2ZnSnS_4 nanocrystal solar cells: efficient stripping of surface insulating layers using alkylating agents, The Journal of Physical Chemistry C, 118 (2013) 804-810.

[130] R. Caballero, E. Garcia-Llamas, J.M. Merino, M. León, I. Babichuk, V. Dzhagan, V. Strelchuk, M. Valakh, Non-stoichiometry effect and disorder in Cu_2ZnSnS_4 thin films obtained by flash evaporation: Raman scattering investigation, Acta Materialia, 65 (2014) 412-417.

[131] X. Fang, T. Zhai, U.K. Gautam, L. Li, L. Wu, Y. Bando, D. Golberg, ZnS nanostructures: From synthesis to applications, Progress in Materials Science, 56 (2011) 175-287.

[132] M. Cao, Y. Shen, A mild solvothermal route to kesterite quaternary Cu_2ZnSnS_4 nanoparticles, Journal of Crystal Growth, 318 (2011) 1117-1120.

[133] R.G. Pearson, Hard and soft acids and bases, Journal of the American Chemical Society, 85 (1963) 3533-3539.

[134] K. Tanaka, Y. Fukui, N. Moritake, H. Uchiki, Chemical composition dependence of morphological and optical properties of Cu_2ZnSnS_4 thin films deposited by sol-gel sulfurization and Cu_2ZnSnS_4 thin film solar cell efficiency,

Solar Energy Materials and Solar Cells, 95 (2011) 838-842.

[135] J.J. Scragg, Studies of Cu_2ZnSnS_4 films prepared by sulfurisation of electrodeposited precursors, in, University of Bath, University of Bath, 2010.

[136] M. Grossberg, J. Krustok, J. Raudoja, K. Timmo, M. Altosaar, T. Raadik, Photoluminescence and Raman study of $Cu_2ZnSn(Se_xS_{1-x})_4$ monograins for photovoltaic applications, Thin Solid Films, 519 (2011) 7403-7406.

[137] T.J. Huang, X. Yin, C. Tang, G. Qi, H. Gong, A low-cost, ligand exchange-free strategy to synthesize large-grained Cu_2ZnSnS_4 thin-films without a fine-grain underlayer from nanocrystals, Journal of Materials Chemistry A, 3 (2015) 17788-17796.

[138] H. Zhou, W.C. Hsu, H.S. Duan, B. Bob, W. Yang, T.B. Song, C.J. Hsu, Y. Yang, CZTS nanocrystals: a promising approach for next generation thin film photovoltaics, Energy Environ. Sci., 6 (2013) 2822-2838.

[139] H. Metin, R. Esen, Annealing studies on CBD grown CdS thin films, Journal of Crystal Growth, 258 (2003) 141-148.

[140] B.L. Williams, S. Smit, B.J. Kniknie, K.J. Bakker, W. Keuning, W.M.M. Kessels, R.E.I. Schropp, M. Creatore, Identifying parasitic current pathways in CIGS solar cells by modelling dark J-V response, Progress in Photovoltaics: Research and Applications, (2015) DOI: 10.1002/pip.2582.

[141] P.A. Fernandes, P.M.P. Salomé, A.F. Sartori, J. Malaquias, A.F. da Cunha, B.A. Schubert, J.C. González, G.M. Ribeiro, Effects of sulphurization time on Cu_2ZnSnS_4

absorbers and thin films solar cells obtained from metallic precursors, Solar Energy Materials and Solar Cells, 115 (2013) 157-165.

[142] W.K. Kim, S. Kim, E.A. Payzant, S.A. Speakman, S. Yoon, R.M. Kaczynski, R.D. Acher, T.J. Anderson, O.D. Crisalle, S.S. Li, V. Craciun, Reaction kinetics of α-$CuInSe_2$ formation from an In_2Se_3/CuSe bilayer precursor film, Journal of Physics and Chemistry of Solids, 66 (2005) 1915-1919.

[143] W.K. Kim, E.A. Payzant, S. Yoon, T.J. Anderson, In situ investigation on selenization kinetics of Cu-In precursor using time-resolved, high temperature X-ray diffraction, Journal of Crystal Growth, 294 (2006) 231-235.

[144] R. Mainz, A. Weber, H. Rodriguez-Alvarez, S. Levcenko, M. Klaus, P. Pistor, R. Klenk, H.-W. Schock, Time-resolved investigation of Cu(In,Ga)Se2 growth and Ga gradient formation during fast selenisation of metallic precursors, Progress in Photovoltaics: Research and Applications, (2014) 10.1002/pip.2531.

[145] C.V. Thompson, Grain growth in thin films, Annual Review of Materials Science, 20 (1990) 245-268.

[146] H.A. Atwater, C.V. Thompson, H.I. Smith, Ion-bombardment-enhanced grain growth in germanium, silicon, and gold thin films, J. Appl. Phys., 64 (1988) 2337-2353.